

## ABSTRACT

### The Design and Validation of an Impinging Jet Test Facility

Peter R. Robertson

Mentor: Kenneth Van Treuren, Ph.D.

An experimental jet impingement facility was constructed with the capability of conducting a detailed analysis of the local heat transfer coefficients beneath an array of large impinging jets. The facility was validated with initial heat transfer studies that determined an appropriate jet discharge coefficient of 0.802 and created a correlation relating local jet Reynolds number and stagnation point heat transfer. The correlation matched closely with previous studies. The thermal effects of impinging jets were visualized by liquid crystal thermography. The resulting thermal footprints of downstream jets revealed the first known documented case of the heat transfer effects of hairpin vortices on the target surface. This phenomenon was identified and discussed.

The Design And Validation Of An Impinging Jet Test Facility

by

Peter R. Robertson, B.S.

A Thesis

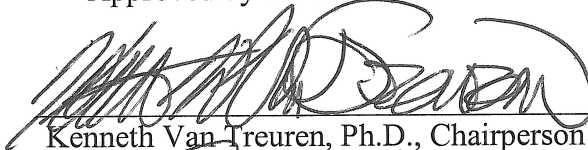
Approved by the Department of Mechanical Engineering



William M. Jordan, Ph.D., Chairperson

Submitted to the Graduate Faculty of  
Baylor University in Partial Fulfillment of the  
Requirements for the Degree  
of  
Master of Science

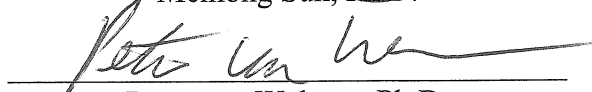
Approved by the Thesis Committee



Kenneth Van Treuren, Ph.D., Chairperson

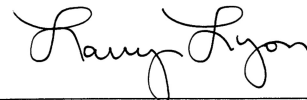


Meihong Sun, Ph.D.



Peter van Walsum, Ph.D.

Accepted by the Graduate School  
December 2005



J. Larry Lyon, Ph.D., Dean

Copyright © 2005 by Peter R. Robertson

All rights reserved

## TABLE OF CONTENTS

LIST OF FIGURES .....	vi
LIST OF TABLES .....	viii
LIST OF ABBREVIATIONS .....	ix
ACKNOWLEDGMENTS .....	xiii
DEDICATION .....	xv
CHAPTER ONE .....	1
Introduction .....	1
<i>Jet Impingement Background and Applications</i> .....	1
<i>Performance in Gas Turbine Engines</i> .....	1
<i>Challenges of a Gas Turbine Engine Designer</i> .....	4
<i>Jet Impingement in the Gas Turbine Engine</i> .....	5
<i>Statement of Problem</i> .....	7
<i>Aims and Objectives</i> .....	8
CHAPTER TWO .....	9
Literature Review .....	9
<i>Introduction to the Literature</i> .....	9
<i>Review of Experimental Facilities</i> .....	9
<i>Impinging Jet</i> .....	12
<i>Single Jet</i> .....	14
<i>Multiple Jets</i> .....	17
<i>Unconfined Jets</i> .....	17
<i>Confined Jets</i> .....	17

<i>Array Configurations</i> .....	22
<i>Heat Transfer Enhancement Elements</i> .....	25
CHAPTER THREE .....	26
Theory .....	26
<i>Heat Transfer Model</i> .....	26
<i>Liquid Crystal Theory</i> .....	28
<i>Thermochromatic Liquid Crystals</i> .....	28
<i>Transient Liquid Crystal Technique</i> .....	30
<i>Double Crystal Technique Using Liquid Crystal Intensity</i> .....	34
CHAPTER FOUR.....	36
Design of the Experimental Jet Impingement Facility .....	36
<i>Introduction to the Experimental Design</i> .....	36
<i>Experimental Apparatus Overview</i> .....	36
<i>Experimental Design and Component Sizing</i> .....	39
<i>Prediction of Flow Losses in the Facility</i> .....	39
<i>Fan Selection</i> .....	41
<i>Piping and Orifice Plate</i> .....	43
<i>Diffuser Plenum</i> .....	45
<i>Flow Straighteners</i> .....	49
<i>Heater Mesh</i> .....	52
<i>Test Section</i> .....	55
<i>Image and Data Acquisition</i> .....	61
CHAPTER FIVE .....	66
Experimental Investigation .....	66
<i>Instrumentation</i> .....	66

<i>Experimental Procedure</i> .....	67
<i>Liquid Crystal Calibration Method</i> .....	71
<i>Jet Hole Discharge Coefficient</i> .....	72
<i>Local Heat Transfer Coefficient</i> .....	75
<i>Flow Field Interpretation</i> .....	77
CHAPTER SIX .....	87
Conclusions and Recommendations .....	87
<i>Summary of the Current Work</i> .....	87
<i>Recommendations to Improve the Current Facility</i> .....	88
<i>Recommendations for Future Work</i> .....	90
APPENDICES .....	92
REFERENCES .....	124

## LIST OF FIGURES

Figure 1 – Effects of RIT on engine power output .....	2
Figure 2 – Introduction of cooling technology and its effect on RIT .....	3
Figure 3 – Thermodynamic tradeoffs in an engine cycle .....	4
Figure 4 – Engine components of a GE CF6 turbofan.....	6
Figure 5 – Cooling schematic within a typical turbine blade .....	7
Figure 6 - The characteristic regions of an impinging jet.....	14
Figure 7 – Local Nu maxima for various nozzle geometries.....	16
Figure 8 – Impinging jet in crossflow.....	18
Figure 9 – Test section nomenclature .....	19
Figure 10 – Pre-impingement jet interference .....	20
Figure 11 – Jet fountain .....	20
Figure 12 – Influence of crossflow on impinging jet structure.....	21
Figure 13 - Impingement plate with varying jet hole diameter and spacing .....	23
Figure 14 – Reorientation of TLC lattice structure.....	29
Figure 15 – Aqueous mixture of encapsulated crystals and binder solution .....	30
Figure 16 – Schematic of semi-infinite solid assumption.....	32
Figure 17 – Baylor University impinging jet test facility .....	37
Figure 18 – Experimental Facility .....	37
Figure 19 – Prediction curve for maximum fluid flowrate.....	41
Figure 20 – Blower fan and nozzle for the current facility.....	42
Figure 21 – Side view of the orifice and piping for the current facility .....	45
Figure 22 – Inlet diverter plates to the diffuser plenum.....	46

Figure 23 – Flow diverter plates in the plenum chamber .....	46
Figure 24 – Flow characteristics in a 90 degree bend.....	47
Figure 25 – Plenum sections side view of the current facility .....	52
Figure 26 – Heater mesh component schematic .....	54
Figure 27 – Impingement array geometry .....	56
Figure 28 – Sample turbine blade impingement hole geometry from a formerly operational Rolls Royce engine.....	57
Figure 29 – Surface thermocouple locations .....	60
Figure 30 – Liquid crystal layers on the target surface.....	62
Figure 31 – Fan control panel .....	69
Figure 32 – Fluid ejection through a jet hole.....	73
Figure 33 – Discharge coefficient distribution across the impingement plate.....	74
Figure 34 – Stagnation point Nusselt numbers at streamwise jet row one .....	76
Figure 35 – Time sequence for average $Re_j = 14,050$ .....	78
Figure 36 - Thermal contour of a first row jet .....	79
Figure 37 – Progressive elongation of impinging jets due to crossflow.....	80
Figure 38 – Enhanced heat transfer effects in the jet channel region .....	81
Figure 39 – Enhanced heat transfer in the jet channel at the back of the array ...	82
Figure 40 – Generation of a hairpin vortex.....	82
Figure 41 – Thermal footprint of a hairpin vortex .....	83
Figure 42 – Time sequence for average $Re_j = 28,800$ .....	84
Figure 43 – Peak in heat transfer at $0.5d$ from stagnation point.....	85
Figure 44 – Secondary peak in heat transfer at $1.5d$ to $2.0d$ from stagnation point .....	86



## LIST OF TABLES

Table 1 – Comparison of experimental facilities.....	13
Table 2 – Comparison of impingement plate geometries and flow conditions ...	24
Table 3 – A comparison of discharge coefficients.....	75

## LIST OF ABBREVIATIONS

$A$	area
$A_j$	jet hole area
$A_{o,i}$	orifice inner diameter
$A_v$	area of jet vena contracta
$CCD$	charged-coupled device (camera)
$CFD$	computational fluid dynamics
$CMC$	ceramic matrix composite
$C$	Centigrade
$C_D$	coefficient of discharge
$C_p$	specific heat
$G_c$	crossflow mass velocity
$G_c/G_j$	ratio of crossflow to jet mass velocity
$GE$	General Electric
$G_j$	jet mass velocity
$d$	diameter
$h$	heat transfer coefficient
$f$	friction factor
$F$	Fahrenheit
$F_o$	orifice flow coefficient
$g$	gravity constant

$h$	local total heat transfer coefficient
$h_c$	crossflow heat transfer coefficient
$h_j$	jet heat transfer coefficient
$h_L$	head loss
$I$	current
<i>IHP</i> <i>TET</i>	Integrated High Performance Turbine Engine Technology
$k$	thermal conductivity
$K_L$	loss coefficient
$\ell$	length
$\ell/d$	length-to-diameter ratio
$m$	experimental constant [Kercher and Tabakoff (1970)]
$\dot{m}$	mass flowrate
$Nu$	Nusselt number
$PC$	personal computer
$Pr$	Prandtl number
$q$	local surface heat flux
$Q$	flowrate
$Q_{ideal}$	ideal flowrate
$Re_j$	jet Reynolds number based on jet hole diameter
<i>RGB</i>	red, green, blue (camera)
<i>RIT</i>	turbine rotor inlet temperature
$t$	time
$T$	temperature

$T_{aw}$	adiabatic wall temperature
$T_c$	crossflow temperature
$T_{down}$	downstream temperature
$T_i$	initial temperature
$T_j$	jet temperature
$T_{mesh}$	mesh temperature
$TOC$	thermocouple open circuit
$T_s$	surface temperature
$T_{up}$	upstream temperature
$TSFC$	thrust specific fuel consumption
$TLC$	thermochromatic liquid crystal
$V$	velocity; voltage
$x/d$	streamwise jet spacing
$y/d$	spanwise jet spacing
$z$	distance to target plate
$z/d$	jet-to-target spacing

### Greek Symbols

$\alpha$	thermal diffusivity
$\beta$	orifice diameter ratio, $h\sqrt{\alpha t} / k$ , or $h\sqrt{\alpha(t - \tau_i)} / k$
$\Delta T_{m,I}$	temperature difference between each temperature step and $T_i$
$\phi_I$	experimental constant [Kercher and Tabakoff (1970)]

$\phi_2$	experimental constant [Kercher and Tabakoff (1970)]
$\eta$	efficiency
$\rho$	density
$\tau$	time constant
$\nu$	dynamic viscosity

## ACKNOWLEDGMENTS

Having “lived” the past year and a half of my life in Room 102 of the Engineering Building at Baylor University, I am both excited and relieved to see my research arrive at an end. However, this day could not have been achieved without the assistance and encouragement of several people who have helped me along this journey.

First, I must extend my most sincere gratitude and admiration to my advisor and mentor, Dr. Ken Van Treuren, who took the challenge of fostering me as the first mechanical engineering graduate student at Baylor University. His passion for teaching and genuine excitement for research has left a lasting impression on me that I pray will only continue to develop as I now venture out into the world to put to good use the practices I have learned. And to Dr. Carolyn Skurla, who first gave me the opportunity to explore research opportunities in her lab, and instilled in me the desire and drive to reach my full potential as a student here at Baylor. Thank you both for your constant support and encouragement that kept me motivated and inspired to continue forth in my studies.

I would also like to thank Mr. Ashley Orr for his machining assistance and guidance which helped make this test facility a reality; and Mr. Dan Hromadka for his computer and software technical assistance in establishing the data and image acquisition systems. Thank you for your tireless efforts in establishing the foundation of this project, upon which, the research could grow. I also wish to thank Dr. Truell Hyde, Vice Provost for Research at Baylor University, whose funding contributions fueled not only this

study, but the establishment of the Baylor University Mechanical Engineering graduate program.

I must also extend earnest thanks to my parents for providing not only the financial resources to my undergraduate education, but for their constant encouragement and guidance in sending me down the right path in my education and in life. Thank you for providing for me this great opportunity and for shaping me into the engineer and the man that I am today.

And lastly, I leave my final appreciation and sentiments to my future wife, Laura, who has endured a great deal over this past year and a half, not the least of which includes many long nights studying with me in “the black hole,” also known as my lab. I cannot even begin to express the love and gratitude I feel for her understanding and patience, which allowed me to concentrate and finish the job. Thank you for always standing by my side and encouraging me to succeed

## DEDICATION

To my family and my fiancé Laura,  
whose constant love and support continue to be my motivation



## CHAPTER ONE

### Introduction

#### *Jet Impingement Background and Applications*

Impingement heat transfer has emerged as a principle source for both controlled cooling and heating of a target surface because of its exceptional ability to augment heat and mass transfer in a variety of industrial processes. Jet impingement can be seen cooling turbine blades and vanes, combustors, electrical and electronic equipment, heating surfaces, and even drying paper, thereby contributing to improving product performance, longevity, efficiency, and quality. The focus of the current study is the application of impinging jets as an effective source of cooling the leading edge and midspan regions of gas turbine blades and vanes by enhancing the convective heat transfer. This thesis reports on the development of an experimental facility and the subsequent facility validation through the investigation of convective heat transfer coefficient,  $h$ , distributions on a flat target surface beneath a standard array of inline impinging jets.

#### *Performance in Gas Turbine Engines*

The Integrated High Performance Turbine Engine Technology (IHPTET) program is a Department of Defense initiative established in 1993 to increase the current 8:1 thrust-to-weight ratio for aircraft gas turbine engines to a more powerful 20:1 level [Han et al. (2000)]. This improvement will be the resultant of several advanced technologies including improvements in material composition. Simple ceramics and composites are too brittle to survive the harsh environment within a gas turbine engine where strength and

durability are essential; therefore, the development of advanced materials such as ceramic matrix composites (CMC) will contribute to increasing the current turbine rotor inlet temperature (RIT) limitations. However, the present demands for engine performance require improvements beyond that of materials only, and must extend to include advancements in component design, high-temperature thermal barrier coatings, and even digital engine control which will allow the custom tailoring of coolant air, amongst other processes, to optimize the needs of each specific stage of flight [Hirschberg (2004)]. These technological improvements will produce significant enhancements in fuel economy and thrust for both military and commercial aircraft engines, but as Figure 1 illustrates, increasing the turbine rotor inlet temperature is critical for improving engine power output.

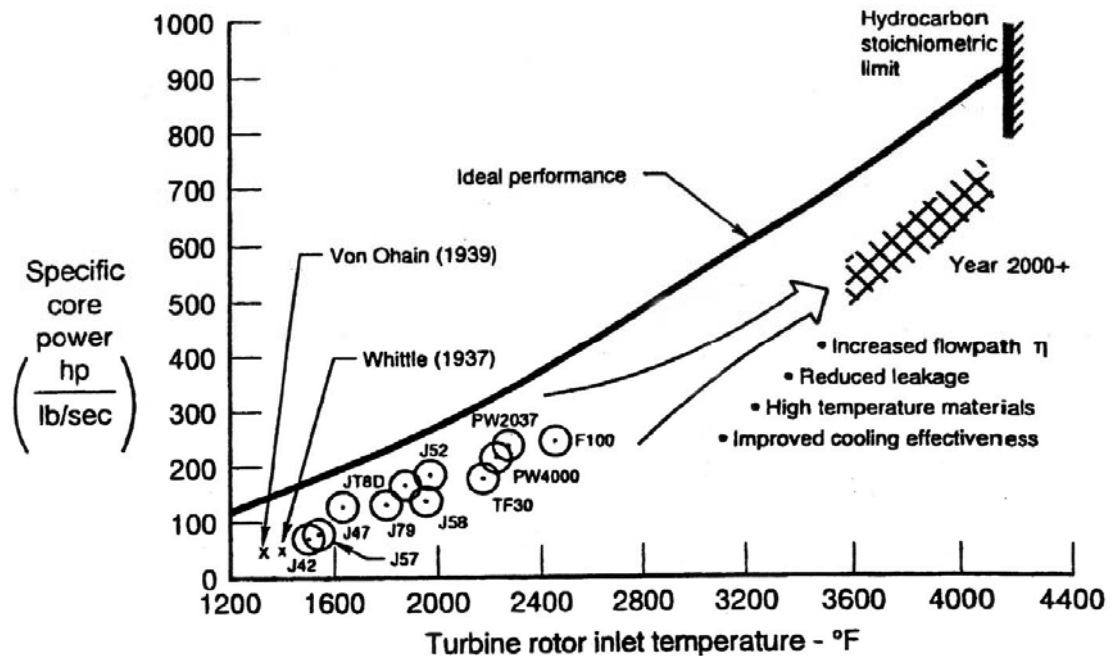


Figure 1 – Effects of RIT on engine power output [Han et al. (2000)]

Figure 1 illustrates several current and past Pratt and Whitney engines, as well as the original Whittle and Van Ohain engines, with their corresponding RIT and specific engine core power output. The ideal performance line denotes a 100% efficient engine (i.e. no leakage or coolant flow). The engines represented tend to advance near this line along the same upward progression of performance. Clearly Figure 1 depicts improved thermal efficiency and power output, and thus, enhanced overall engine performance, with increasing RIT. However, although it remains clear that increasing the RIT improves engine performance, Figure 2 demonstrates that these temperatures exceed the allowable metal temperature, and without proper cooling, the metals within the engine cannot withstand the increased RIT requirement for improved performance.

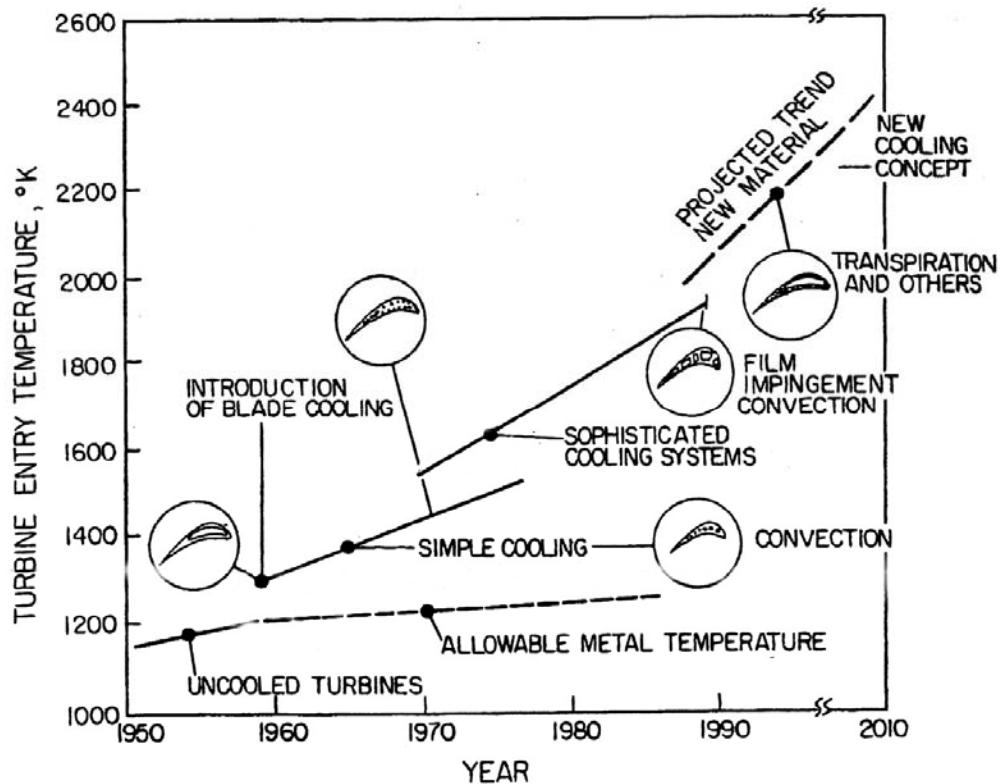


Figure 2 – Introduction of cooling technology and its effect on RIT [Han et al. (2000)]

### *Challenges of a Gas Turbine Engine Designer*

One of the greatest problems facing an engine designer is how to increase the specific thrust of an engine without increasing the aircraft weight or specific fuel consumption. It has already been established, by Figure 1, that an increase in RIT increases engine power output. Increasing engine power, increases specific thrust, which is then coupled with an increase in the thrust-to-weight ratio, which, as Figure 3 depicts, lowers the thrust specific fuel consumption (TSFC). The increase in turbine inlet temperature also allows for options when considering mission application and performance. The increase in thrust can either translate to an increase in payload capacity for commercial aircraft or increased flight speed for fighter aircraft, which allows for quicker combat departure and improved combat abilities, without increasing the diameter of the engine. Conversely, should the thrust demands of a flight remain fixed, the actual engine diameter could be reduced, thereby decreasing material cost, reducing drag, and minimizing aircraft weight which could lead to further improvements in fuel economy.

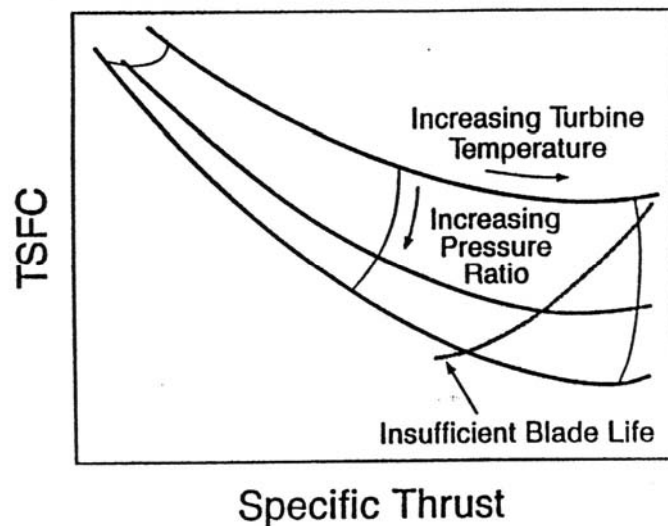


Figure 3 – Thermodynamic tradeoffs in an engine cycle [Borns (1989)]

As Figures 1 and 2 illustrate, current gas turbine engines operate at temperatures exceeding 3000°F (2000 K) in order to maximize their thermal efficiency and power production. As temperatures rise within the turbine to generate this improved performance, the amount of heat transferred to the turbine blade increases, which creates higher fatigue and thermal stress concentrations on the blade itself. An engine designer must therefore use cooling air to minimize these concentrations and create a durable, longer-lasting part. A simple 100°F reduction of turbine blade metal temperature can prolong the blade life by a factor of ten [Van Treuren (1994)]. The use of cooling air does however, decrease the amount of air available for combustion, and subsequently, the capable thrust and cycle efficiency, since the coolant air is extracted from the compressor bleed.

#### *Jet Impingement in the Gas Turbine Engine*

The extraction of air from the compressor for the use of cooling penalizes the thermal efficiency. Therefore, it is important to optimize the amount of coolant air used to cool turbine blades. Too little coolant air will reduce blade life due to the higher temperatures it experiences; however, too much coolant air will negatively impact the engine's Brayton Cycle and thus, diminish engine performance by removing an excess of air from the combustion cycle. An advanced cooling system must therefore create a balance between performance and component longevity within a gas turbine engine.

Figure 4 depicts a cutaway section of the General Electric (GE) CF6 turbofan engine. From this figure, it can be seen that air enters from the fan-side, and travels through the engine to the exit of the compressor. Here, typically twenty percent of the compressor bleed air is removed from the engine cycle and routed to the inside of the

turbine blade to be used for cooling [Han et al. (2000)]. Inside the turbine blade are two chambers. The inner chamber is pressurized by the coolant air. The pressure differential between the two chambers drives the air through the perforated wall and impinges upon the internal wall of the turbine blade, as highlighted in Figure 5. The impingement air then effuses to the outside of the turbine blade creating a film of cooler air to protect the blade. The purpose of these cooling techniques is to create temperature uniformity within the turbine blade below the material limit. The spent impingement air is then often used in conjunction with film cooling, whereby a thin “film” of relatively cooler air (the post-impingement air) blankets the outside of the turbine blade providing a thin barrier from the intense heat within the engine cycle. This “relatively” cooler air is so labeled because the coolant air temperature from the compressor is a mild 1500°F compared with the actual 2500 to 3000°F experienced in the turbine during the engine cycle.

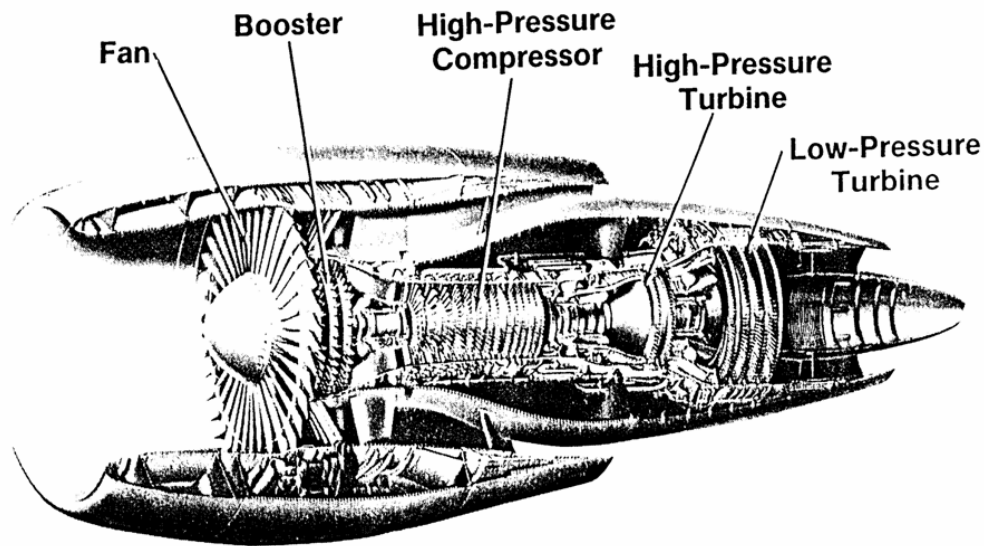


Figure 4 – Engine components of a GE CF6 turbofan [Mattingly (1996)]

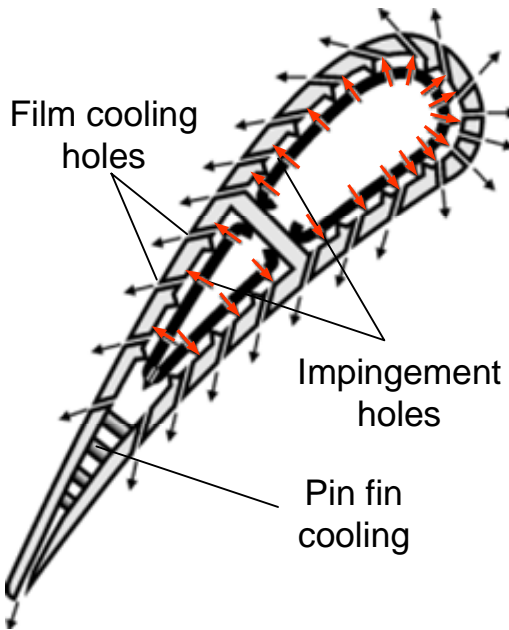


Figure 5 – Cooling schematic within a typical turbine blade [Nomoto et al. (1996)]

### *Statement of Problem*

Jet impingement arrays have been widely accepted as an effective technique of turbine cooling, especially on the leading edge and midspan regions of gas turbine blades and vanes. The turbine industry would most benefit from heat transfer correlations obtained for the complex geometries found within an actual gas turbine environment; however, modeling such configurations to obtain useful data is very complicated and experimentally and computationally expensive. As a result, the turbine industry often includes more jet impingement holes than necessary, uses an excess of coolant air, or simply limits the operating conditions of the engine. Nevertheless, various simple jet configurations and geometries have provided a vast resource to the gas turbine community in regards to jet heat transfer characteristics, which are confined to the empirical correlations resulting from experimental studies of these jet geometries and configurations. By determining the local heat transfer coefficients on the target surface,

the optimum jet configuration can be established to promote the greatest heat transfer for the minimum usage of coolant flow.

The cooling effectiveness of impinging jets generates a significantly high local heat transfer coefficient centered on the target surface directly beneath the jet's core. This aids in the reduction of the intense temperatures experienced in the high pressure turbine so vital to improving engine performance. Since this engine performance is governed by the engine's allowable turbine inlet temperature, a higher inlet temperature translates to higher efficiency and greater power output. The inlet temperature is bounded by the material's melting point, and thus, impinging jets are employed to increase the capable inlet temperature beyond that of the material properties.

### *Aims and Objectives*

These impinging jet heat transfer methods can be investigated through the development and subsequent use of an impinging jet test facility, whereby more detailed correlations can be obtained to help designers better configure jets in a turbine blade. The primary purpose of this study is to

1. Develop an impinging jet test facility with an array of very large impingement holes at Baylor University
2. Validate the facility by performing initial heat transfer studies to determine an appropriate jet discharge coefficient and the heat transfer coefficient at the stagnation point beneath an impinging jet. Compare the results with previous studies. Validation will be considered satisfactory if the percent difference between the current study and the literature is within 10%.



## CHAPTER TWO

### Literature Review

#### *Introduction to the Literature*

The need to improve engine performance and efficiency is the driving force behind experimentation and testing of engine cooling techniques. Experimentation provides designers with correlations whereby they may better design the impingement cooling schemes within gas turbine blades and vanes. The actual gas turbine engine is very complex with many different parameters to control in order to examine the effect of one phenomenon such as impingement cooling. Therefore, a facility must be created specifically for the purpose of testing different impingement systems, so that an impinging jet's characteristic behavior may be properly observed and correlated.

#### *Review of Experimental Facilities*

Jet impingement facilities allow for the modeling of the cooling effects of impinging jets on gas turbine blades and vanes. Van Treuren et al. (1994, 1996) used a suction-type fan to draw air through a heater, and into the 0.5 x 0.5 x 0.2m plenum through well-insulated pipework. Until the heated air had reached a uniform plenum temperature, a set of valves acted as a bypass mechanism to prevent the air from reaching the impingement plate. Upon reaching a steady thermal conduction in the plenum, the fast acting valves were opened, allowing air to flow through the impingement plate. The test plate was an 8 x 5 jet array of 5 mm diameter, sharp-edged impinging jet holes with  $8d$  spacing in both the streamwise and spanwise directions. Since the impingement plate is

linked to the target plate by the recirculation regions created by the shear interaction between the jet and the stagnant air of the test section, it was important for this study that the impingement plate temperature be controlled to determine any heat transfer contributions to the target surface from sources other than the jet itself. Therefore, the temperature of the impingement plate was controlled using a constant water bath throughout the transient experiments. The jet-temperature profile was then attained over time for jet Reynolds ( $Re_j$ ) numbers ranging from 10,000 to 40,000, by the thermographic liquid crystal (TLC) technique using three narrowband crystals with a CCD video camera and frame grabber software.

Wang et al. (1996) performed a comparative study which examined the use of a heater mesh coated in thermochromatic liquid crystals (a temperature indicator discussed in Chapter Three) to measure the heating uniformity of air flow at the exit of the experimental tunnel. This study validates the heater mesh method originally developed and described by Gillespie (1993) and establishes the use of the mesh heater and liquid crystal thermography as an accurate and cost-effective means of uniformly heating airflow and producing an accurate thermal profile. These conclusions effectively eliminate the need for a fast acting valve system by allowing rapid temperature change at low speed flows. Previously, a much more complex technique was required to validate heating uniformity which included the use of traversing probes and temperature rakes [Byerley et al. (1988) and Moss and Oldfield (1991)]. Therefore, the heater mesh method using liquid crystal thermography will be used for the present study.

Lee et al. (1997) examined a single, round jet produced from a centrifugal blower fan, which was networked through a copper pipe to the constant temperature bath and heat

exchanger coil. The pipe then transitioned to a cast acrylic pipe which housed the orifice meter. The exit to the orifice included a smooth transition approximately 150 cm downstream of its exit into the smaller diameter impingement pipe whose length was 58d to ensure a fully developed round jet condition. Thermocouples were inserted in the pipe upstream of the impingement to measure the jet temperature and outside of the pipe to measure the ambient temperature. Images of the liquid crystal-coated target surface were captured by a color video camera system and frame grabber board.

San and Lai (2001) also used a water bath and heat exchanger coil to heat air supplied by a large reciprocating air compressor. Before impingement, the air had to be purified, and therefore, the system included a vapor compressor type dehumidifier and adsorption columns to remove oil in the air supply line. An isobaric surge tank was also used to minimize pressure fluctuations generated from the cyclic nature of the air compressor, and a pressure regulator controlled the exit pressure of the air to the system. The impingement test section was 0.26 x 0.4m with spent air confined to exit in two opposing directions. The air itself was not heated; instead, the target plate was fitted with nine 0.01 mm thick, stainless steel heating foils with silicon filling the irregularities between foils to promote a smooth target area. The impingement heat transfer measurements for this study were taken with 76 traditional T-type thermocouples affixed beneath the heating foil with a highly thermally conductive paste.

Gao et al. (2003) passed air via a compressor through an orifice to measure flowrate and determine the effective jet Reynolds number. Air was channeled through an in-line heater, and diverted away with a valve system until a steady heated temperature was reached. The heated air was then forced through a 90 degree bend into a diffuser

which emptied into a 38.1 x 38.1 cm plenum chamber. The target plate was coated with liquid crystals to indicate the heat transfer rate and the effects recorded by an RGB camera and color frame grabber PC board. This experimental system was capable of achieving jet Reynolds numbers ranging from 2,000 to 10,000 and image capture was obtained via an RGB camera and frame grabber system.

A complete comparison of the experimental facilities is seen in Table 1. All these facilities were designed for the purpose of investigating the cooling effectiveness of impinging jets, so that engine designers might better understand the characteristic nature and flow patterns associated with an impinging jet or jet array.

### *Impinging Jet*

An impinging jet is a locally concentrated stream of coolant air expelled from a hole or slot, which impinges upon a target surface (Fig. 6). The jet itself can be subdivided into three characteristic zones: the free jet, stagnation region, and wall jet region. The free jet exists directly beneath the hole exit. Jet flow does not reach a fully developed state until approximately six hole diameters from the exit plane [Van Treuren (1994)]; therefore, in the case of the gas turbine application, the plate-to-target ( $z/d$ ) distance is too small for a fully developed jet to be realized.

When the coolant air is ejected from the hole, the jet forms a shear layer with the surrounding, relatively stagnant air. This shear layer is unstable and therefore generates turbulence in the form of a recirculation region directly adjacent to the jet's core. The eddies that result from the shear interaction are then propagated downstream along with the spent coolant, helping to enhance heat transfer in the regions between jets.

Table 1 – Comparison of experimental facilities

Article	Air Supply	Heater	Bypass	Plenum Size	Hole Diameter	Image Capture	Temperature Indicator	Test Technique	Re Range
Van Treuren et al. (1994 and 1996)	suction fan	water-cooled impingement plate	3-way diverter valve	0.5 x 0.5 x 0.2m	5mm	CCD video camera w/ frame grabber	TLC (narrowband)	Transient	10,000-40,000
Wang et al. (1996)	blower fan	heater mesh	none	not specified	none specified	RGB camera w/ frame grabber	TLC	Transient	15000-55000
Lee et al. (1997)	blower fan	constant temperature bath and heat exchanger coil	none	none	0.013 to 0.034	RGB camera w/ frame grabber	TLC (narrowband)	Steady	11,000-50,000
San and Lai (2001)	air compressor	target surface heated by thin-foil heater	none	0.26 x 0.40m	not specified	none	T-type thermocouples	Steady	10000-30000
Gao et al. (2003)	air compressor	in-line air heater with heater controller	3-way diverter valve	0.0381 x 0.0381m	3.175 to 6.35mm	RGB camera w/ frame grabber	TLC (narrowband)	Transient	2000-10000
Kanokjaruvijit and Martinez-Botas (2003)	blower	in-line air heater	diverter valve	0.32 x 0.32m	10mm	3CCD camera w/ firewire transfer	TLC (wideband)	Transient	5000-11500

The core of the jet impinges upon the target surface, and the region directly beneath the jet is known as the stagnation region. Here, essentially only the effects of that single jet are realized, and it is therefore the highest area of heat transfer. Upon impingement, the jet must flow radially outwards, and thus, forms a wall jet along the target surface. The wall jet creates a thin boundary layer, which is due to the column of jet air “pressing down” on the boundary layer as it moves outward. This causes some local acceleration with higher heat transfer coefficients. The wall jet region, outside the impinging jet region, is characterized by a deceleration and disbursement of coolant as it interacts with the recirculation region, which may cause turbulent transition of the laminar boundary layer; however, locally, the influence of the wall jet enlarges and progressively decreases the heat transfer effectiveness.

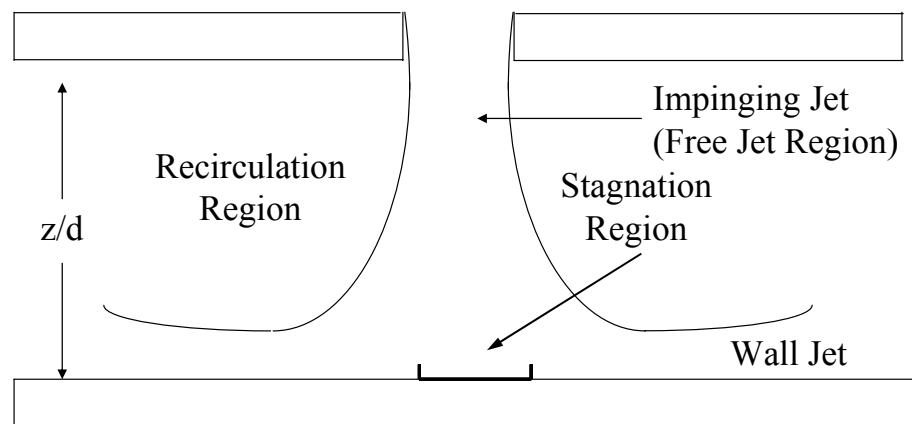


Figure 6 - The characteristic regions of an impinging jet

### *Single Jet*

The study of a single jet is of importance to the present work because it models the initial rows of jets in an impingement array. Since the beginning rows of jets do not generally experience a crossflow effect, their effects closely resemble that of a single

impinging jet. Therefore, a detailed study of a single jet can aid in the understanding of jet behavior in an impingement array.

Jambunathan et al. (1992) provides a detailed literature review of singular circular jet impingement heat transfer studies. Their review emphasizes the critical regions, parameters, and variables of interest in a single impinging jet study, and provides a comparative examination of experimental differences which can lead to a significant influence on the ensuing heat transfer rate. The simplest correlation for the local heat transfer coefficient was reported to be of the form

$$Nu = f(Re_j, z/d, x/d, Pr)$$

where  $Nu$  is the average Nusselt number,  $Re_j$  is the jet Reynolds number,  $z/d$  is the jet-to-target spacing,  $x/d$  is the jet hole spacing, and  $Pr$  is the Prandtl number. This correlation does not, however, account for the effects of nozzle geometry, jet confinement, and turbulence generation upstream of the jet nozzle. Several others [Goldstein et al. (1986) and Metzger et al. (1989)] have also provided correlations relating the above parameters, and Florschuetz et al. (1981) even extended the correlation to include the effects of crossflow.

Obot et al. (1979) determined that nozzle geometry is pivotal in determining the jet turbulence levels which Jambunathan et al. (1992) referred to as points of experimental variation in their literature survey. Their study examined contoured and sharp-edged jet holes as well as varying jet hole length-to-diameter ratios ( $\ell/d$ ). Jets with a short  $\ell/d$  ( $\ell/d = 1$ ) produced a significant variation in heat transfer effectiveness for the two inlet geometries, with sharp-edged holes producing approximately 25 percent greater heat transfer than the contoured geometry (see Figure 7). This is due in part to the large

variation in jet exit velocities. Jets with a contoured geometry or a sharp-edged hole with a large  $\ell/d$  ( $10d$ ) tend to reattach inside the jet hole. With a large enough  $\ell/d$ , fully developed pipe flow can result, which can reduce the exit velocity by up to 30 percent and thus, diminish the heat transfer rate.

A local heat transfer maximum has been frequently reported in the literature at a radial distance of  $0.5d$  from the stagnation point for low  $\ell/d$  jet holes and low  $z/d$  values (less than  $6-8d$ ) (see Figure 7) [Gardon and Akfirat (1965), Obot et al. (1979), and Lee et al. (1997)]. The strength of the maximum is a function of the jet Reynolds number and  $z/d$ . These studies have attributed this phenomenon to a local acceleration of flow caused by a minimum in the boundary layer thickness of the wall jet. Heat transfer was found to monotonically decrease radially outwards from this point until a second peak in heat transfer was found to occur at a radial distance of approximately  $1.5d$  to  $2d$  from the stagnation point. This additional maximum is attributed to the transition of the wall jet region from laminar to turbulent flow resulting in an abrupt increase in the heat transfer rate (see discussion on page 15).

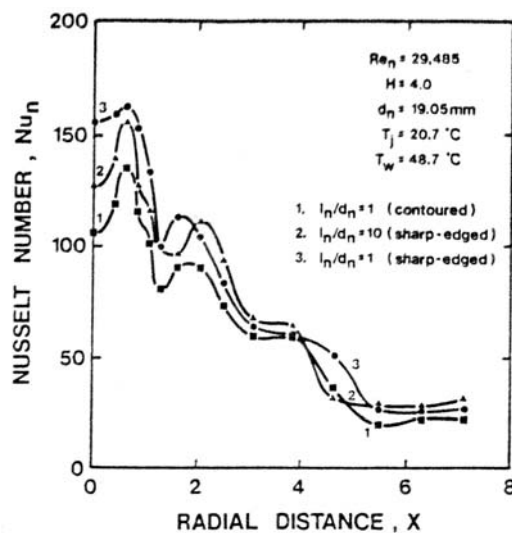


Figure 7 – Local  $Nu$  maxima for various nozzle geometries [Obot et al. (1979)]



## *Multiple Jets*

### *Unconfined Jets*

An impinging jet may be unconfined or confined. An unconfined jet allows the spent coolant air to diffuse openly with the atmosphere, thereby concentrating its primary use in only one centralized location. Rhee et al. (2002) and Hebert et al. (2004) examined this effect by developing effusion holes between the jet holes in which the spent air could exit from the test chamber without interfering with neighboring jets. The results show that the minimization of crossflow generated relatively uniform distributions of heat transfer coefficients. Overall, this study showed that jet strength was maintained under each hole, and little degradation in heat transfer occurred downstream as is present with crossflow in a confined design. However, although these results are promising for maximizing the results of the impinged coolant air, the idea is not indicative of current gas turbine engines where crossflow is the inherent result of spent air exiting the engine naturally.

### *Confined Jets*

A confined jet impinges on the target surface and is constrained within the bounds of the impingement plate and the target plate (and usually on three sides), causing the spent air to be ejected in only one direction. This confinement generates a “crossflow” perpendicular to the core jet flow direction, as illustrated in Figure 8. When several impinging jets are arranged in an array and confined to one flow exit direction, the effects of the upstream jets can be felt by the downstream jets.

Kercher and Tabakoff (1970) provided the foundation for examining the effects of crossflow in impingement cooling. They tested a variety of Reynolds numbers for the

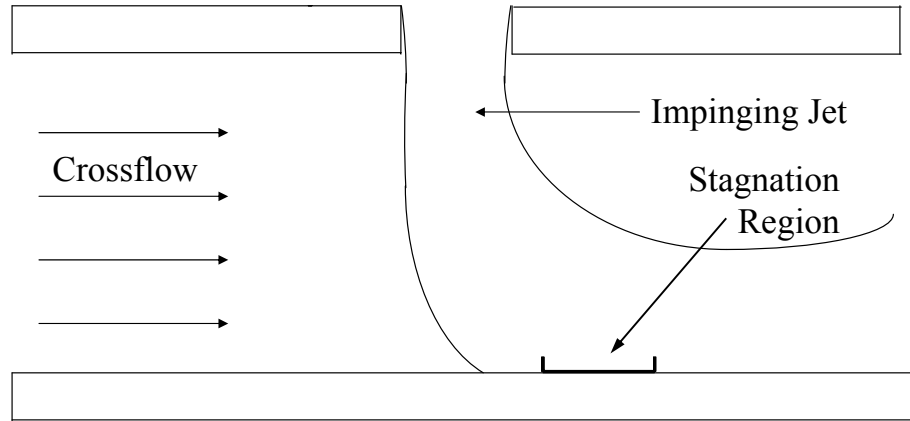


Figure 8 – Impinging jet in crossflow

effects of jet diameter, jet spacing, and jet-to-target distance and arrived at the following empirical steady state correlation for the average Nusselt number,  $Nu$ :

$$Nu = \phi_1 \phi_2 \text{Re}_j^m \text{Pr}^{\frac{1}{3}} \left( \frac{z}{d} \right)^{0.091} \quad (1)$$

where  $\phi_1$ ,  $\phi_2$ , and  $m$  are constants evaluated from graphs derived from the presented data.

The variable,  $\phi_2$ , is a function of  $G_c/G_j$ , the ratio of crossflow to jet mass velocity.

Increasing this ratio decreases the value of  $\phi_2$  and consequently the average  $Nu$ , or heat transfer. They also noted that crossflow produces the opposite effect on performance in regards to  $z/d$  spacing. That is, increasing  $z/d$  in crossflow diminishes the heat transfer rate at the start of the array. With no crossflow, the heat transfer rate was enhanced with increasing  $z/d$  due to formation of turbulence in the expelled jet. Bailey and Bunker (2002) however, showed that the contribution of crossflow to a small  $z/d$ , can actually increase the row resolved average  $Nu$  downstream, near the flow exit. This is due to the channel-like flow of the spent impingement air gaining strength and velocity from each successive spanwise row of jets as the spent air moves closer to the exit.

Perry (1954) first showed that any bending of a jet which alters its impingement angle results in a reduction in heat transfer coefficient. Since a strong crossflow may displace the jet core from directly beneath the center of the impingement hole, as Figure 8 illustrates, so must the largest area of heat transfer be shifted in the direction of the crossflow, and its ensuing heat transfer effects diminished. In addition to the jet Reynolds number and the spacing of the impingement channel ( $z/d$ ), the spacing between the jets (see Figure 9) themselves has been shown to be a vital factor in heat transfer effectiveness in the presence of crossflow [Florschuetz et al. (1981), San and Lai (2001), and Bailey and Bunker (2002)].

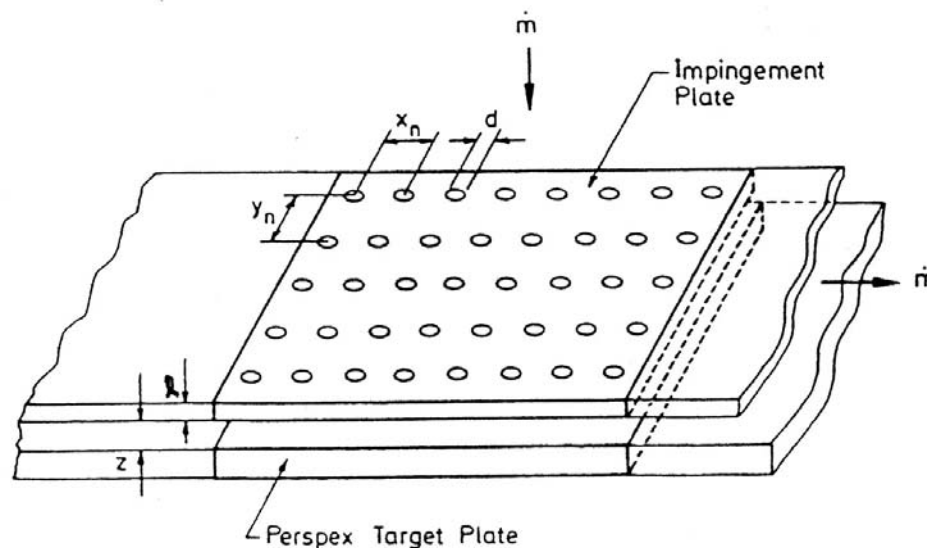


Figure 9 – Test section nomenclature [Van Treuren (1994)]

San and Lai (2001) attempted to optimize jet spacing and noted two plausible causes for diminished heat transfer: pre-impingement jet interference and/or jet fountain. For small jet spacing, because of shear layer expansion, adjacent jets may interfere prior to target impingement (see Figure 10). This interference diminishes the overall jet strength and weakens the heat transfer effect. Conversely, if both jets impinge, a strong

head-on collision between wall jets may produce a jet fountain, as shown in Figure 11.

The entrainment effect will then force both the left and right side flows to recirculate with the jet core causing heated air to mix with the cooling air, diminishing its heat transfer capability. Florschuetz et al. (1981) showed that for small spanwise ( $x_n \leq 10d$ ) and streamwise ( $y_n \leq 6d$ ) jet spacings and/or a jet-to-target ( $z/d$ ) spacing greater than one jet diameter, the resulting crossflow created a significant diffusion of the jet core, and a notable reduction in heat transfer effectiveness.

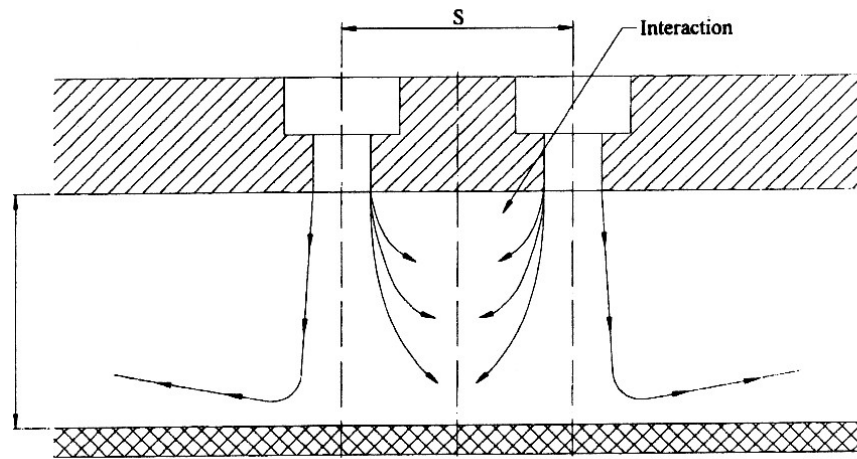


Figure 10 – Pre-impingement jet interference [San and Lai (2001)]

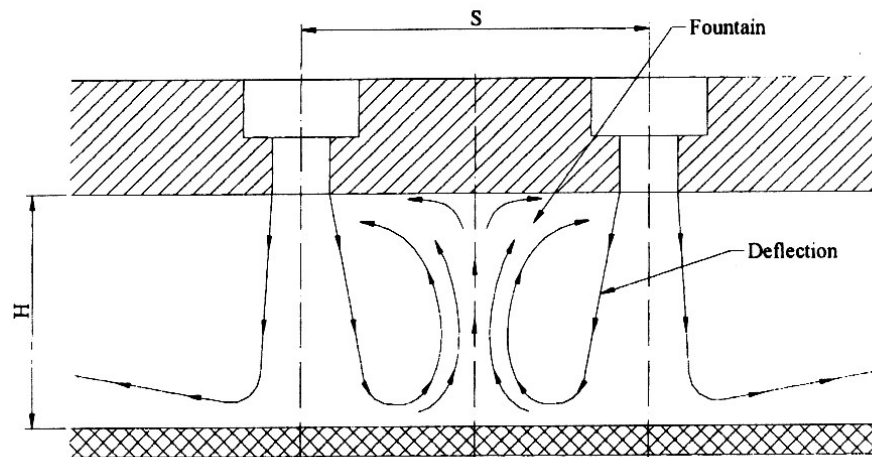


Figure 11 – Jet fountain [San and Lai (2001)]

For larger jet hole spacings and a  $z/d = 1$ , Florschuetz et al. (1981) documented a slight increase in heat transfer as crossflow was found to directly increase the heat transfer rate without significantly reducing the contribution of the impinging jet itself. This is in part explained by the further enhancement of heat transfer at locations between the jets because crossflow promotes greater jet interaction, thereby increasing the turbulent influence of the recirculation region, but, in this case, without generating a strong jet fountain effect which interferes with the bulk flow.

Crossflow also tends to elongate and distort the circular heat transfer footprint that would normally be seen under a single jet. This elongation of the core impingement area corresponds with a resulting diminished heat transfer rate, since the same amount of coolant must be applied to the greater (elongated) effective area. This effect is better demonstrated in Figure 12, which illustrates the elongated jet influence effects generated by crossflow.

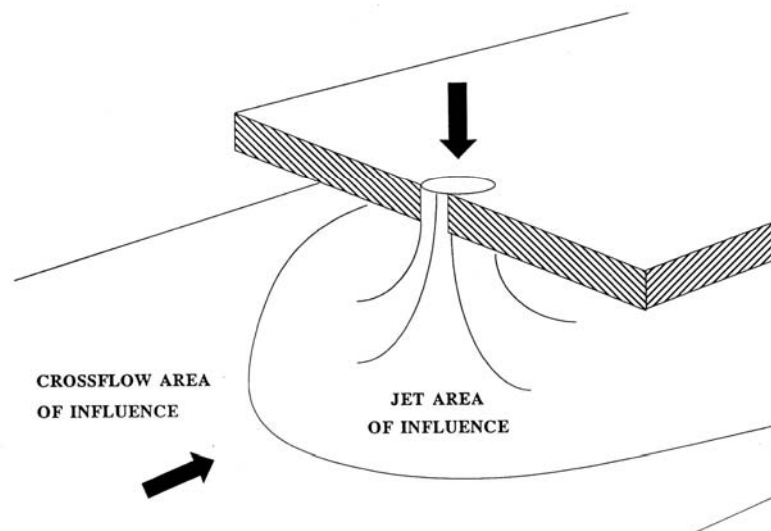


Figure 12 – Influence of crossflow on impinging jet structure  
[Van Treuren (1994)]

### *Array Configurations*

The array configuration is also a critical factor in the influence of crossflow and the resulting heat transfer effectiveness. An array of multiple impinging jets is often modeled in a variety of configurations, the most common of which is a uniform, inline array [Kercher and Tabakoff (1970), Florschuetz et al. (1981), Van Treuren et al. (1994 and 1996), and Bailey and Bunker (2002)]. The uniform, inline array consists of jet holes of identical size and spacing, placed directly streamwise and spanwise of each other. This array was illustrated earlier in Figure 9, given that  $x_n = y_n$ , and will be the array used for the present experimental validation.

The uniform hole case can also be coupled with a staggered geometry, whereby the odd numbered rows exhibit the same geometry as the inline case, but the holes of the even numbered rows are shifted to be midway between the holes in the preceding row [Florschuetz et al. (1981), San and Lai (2001), and Hebert et al. (2004)]. This configuration is more specifically aimed to allow crossflow to penetrate the areas between jets.

The hole size and spacing may also be varied [Gao et al. (2003)]. A plate with varying hole diameter and spacing is shown in Figure 13. Here, the hole size progressively enlarges downstream of the first row of holes. The spacing between holes also increases, that with each successive row, the spacing increases by a jet diameter (i.e. if row one begins at a  $2d$  spacing, then row two has  $3d$  spacing, and row three has  $4d$ , and so on) This geometry is meant to create a larger bulk flow in the latter rows of jets, thereby trying to minimize the adverse effects of crossflow on the downstream holes by limiting the amount of coolant mass which is ejected from the initial row jets. This is

effective in maintaining the core of the latter row jets, but heat transfer upstream is usually lessened directly beneath the jet because of its limited flow.

A summary of some of the literature for single and multiple arrays of impinging jets is presented in Table 2. The table provides a synopsis of the types of arrays studied as well as a comparison of the jet diameter, Reynolds number, and spacing parameters investigated. This review was used to finalize the present design parameters to ensure that the present work is well representative of past and current impinging jet studies. It is

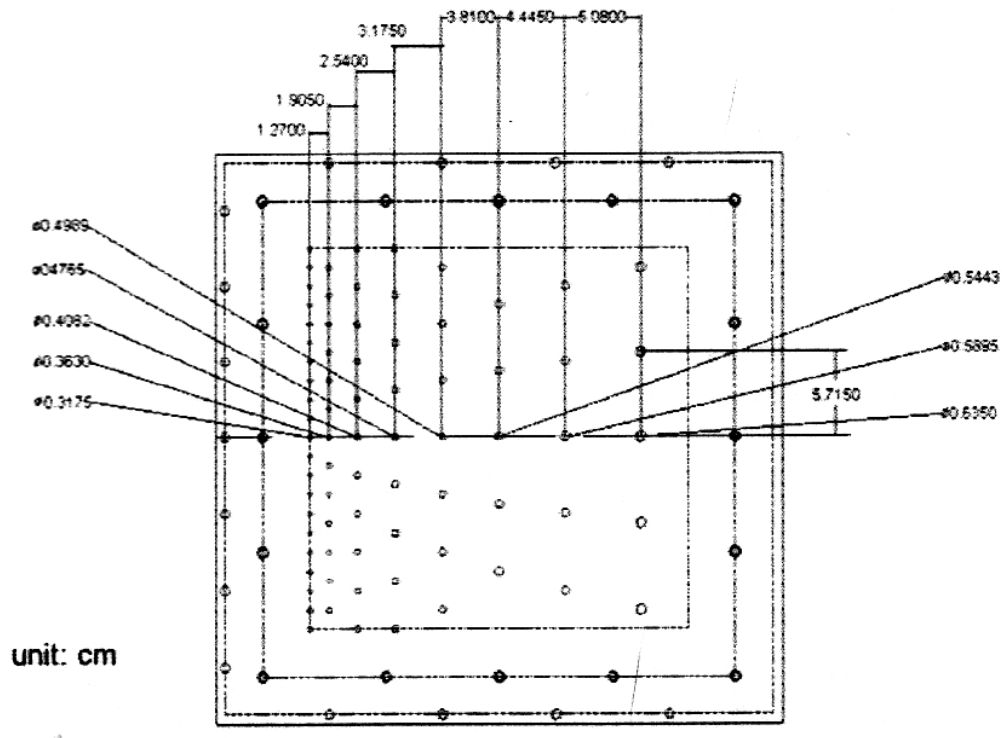


Figure 13 - Impingement plate with varying jet hole diameter and spacing (Gao, et al. 2003)

hoped that this facility will provide a better understanding of the heat transfer behavior of arrays of impinging jets, so that their use might be optimized to produce the best possible performance enhancements for today's gas turbine engines.

Table 2 – Comparison of impingement plate geometries and flow conditions

Author	Year	Nozzle	Jet Diameter (mm)	Re <sub>j</sub> Range	x/d, y/d	z/d	ℓ/d	Geometry	Array Size	Extras
Kercher and Tabakoff	1970	sharp	0.254-2.032	332-3710	3.17-12.5	1.4-8	0.263-1.18	inline	4x4-16x16	none
Obot et al.	1979	contoured sharp	19.05	15000-60000	n/a	2-12	1-40	single jet	1x1	none
Florschuetz et al.	1981	sharp	0.635-7.62	5000-50000	5-15, 4-8	1-6	1	inline, staggered	10x4-10x32	none
Van Treuren et al.	1994	sharp	5	10000-40000	8, 8	1	1.2	inline	8x5	none
Van Treuren et al.	1996	sharp	4.7	10000-18000	8, 8	1, 4	1	inline	8x4	none
Lee et al.	1997	sharp	1.3 to 3.4	11000-50000	n/a	2-10	58	single jet	1x1	none
San and Lai	2001	sharp	3	10000-30000	4-24	2-5	1	staggered	2x3	none
Bailey and Bunker	2002	sharp	5.08, 10.16	14900-64900	3-9	1.25-5.5	1	inline	3x4, 20x26	none
Rhee et al.	2002	sharp	10	10000	6, 6	0.5-10	2	inline	5x5	none
Gao et al.	2003	sharp	6.35 3.175 to 6.35	2000-10000	varying	1, 3, 5	2 varying	stretched	varying	none
Kanokjaruvijit and Martinez-Botas	2003	sharp	10, 20	5000-11500	8, 8	2-12	1.3-2.5	inline	8x8	dimples
Hebert et al.	2004	sharp	2.54	10000-30000	5, 5	not specified	5	inline, staggered	2x11	effusion holes



*Heat Transfer Enhancement Elements*

Several other experimental techniques have also been investigated to enhance the heat transfer of the jet without altering the amount of flow from the jet itself. These include the use of effusion holes [Rhee et al. (2002) and Hebert et al. (2004)], target surface dimples [Kanokjaruvijit and Martinez-Botas (2003)], and rib turbulators (pin fins, pimples, etc.) [Son et al. (2005) and Hong et al. (2005)]. Effusion holes were described earlier as a means of eliminating the adverse effects of crossflow and promoting greater direct jet impingement. Dimples and rib turbulators promote heat transfer by not only adding surface area, but by also tripping the boundary layer to advance the onset of transition and turbulence which enhances the heat transfer rate. All of these are a means of advancing the technology of the gas turbine engine to enable better performance of today's aircraft so they can fly higher, faster, farther, and more efficiently.

## CHAPTER THREE

### Theory

This chapter presents the transient heat transfer theory, beginning with a simplified heat transfer model. Next, a discussion of liquid crystal theory and the principle concepts behind their thermochromatic capabilities is given. Lastly, the transient liquid crystal technique using the double crystal method of analyzing color intensity to determine the local heat transfer coefficients across the target surface is discussed.

#### *Heat Transfer Model*

The impingement of heated air onto the target surface is a convective heat transfer problem with the local surface heat flux,  $q$ , expressed as:

$$q = h(T_{aw} - T_s) \quad (2)$$

where  $h$  is the local total heat transfer coefficient,  $T_{aw}$  is the adiabatic wall temperature, and  $T_s$  is the surface temperature. The total heat transfer coefficient is a combination of the heat transfer effects caused by the jet and crossflow as seen by the following:

$$h = h_j + h_c \quad (3)$$

where  $h_j$  is the jet heat transfer coefficient and  $h_c$  is the crossflow heat transfer coefficient. On some occasions, the effects of the impingement plate are taken into consideration by controlling the temperature of the impingement plate (by means such as a water bath [Van Treuren (1994)]), but for most studies, these effects are not considered and will not be considered in the present investigation.

The adiabatic wall temperature found in Equation (2) is often referred to as the driving gas temperature because it considers the effective mixing of the jet and crossflow together as:

$$T_{aw} = \frac{h_j T_j + h_c T_c}{h_j + h_c} \quad (4)$$

where  $T_j$  is the jet temperature and  $T_c$  is the crossflow temperature. Equations (3) and (4) can therefore be combined and simplified to give the surface heat flux as:

$$q = (h_j + h_c) \left( \frac{h_j T_j + h_c T_c}{h_j + h_c} - T_s \right) = h_j (T_j - T_s) + h_c (T_c - T_s) \quad (5)$$

or even more simply:

$$q = h(T_{aw} - T_s) \quad (6)$$

where both the total heat transfer coefficient and adiabatic wall temperature can be found for the current study with a transient test using the double crystal method of measuring heat transfer (discussed later in this chapter). Therefore, Equation (6) provides the local surface heat flux for the convective heat transfer problem by simplifying all temperatures and corresponding heat transfer coefficients into the adiabatic wall temperature, or fluid temperature, and the effective local total heat transfer coefficient.

For literature comparison purposes, the results can then be presented in terms of the dimensionless Nusselt number,  $Nu$ :

$$Nu = \frac{hd}{k} \quad (7)$$

where  $d$  is the jet hole diameter and  $k$  is the thermal conductivity. Based upon these equations, the present study will develop a facility that will provide the local heat transfer coefficient and adiabatic wall temperature for an array of impinging jets.

## *Liquid Crystal Theory*

### *Thermochromatic Liquid Crystals*

Thermochromatic liquid crystals have been utilized in heat transfer experiments for several decades as a method of temperature measurement [den Ouden and Hoggendoorn (1974), Hippensteele et al. (1983), Van Treuren (1994), and Son et al. (2005)]. Essentially, liquid crystals are a temperature indicator that reflects incident white light to display color relative to wavelength which is proportional to temperature. The temperature response is determined by the pitch, or the measure of molecule rotation of the helicoidal arrangement of liquid crystal molecules [Van Treuren (1994)]. A byproduct of the helical structure of the cholesteric mesophase is its ability to selectively reflect light of wavelengths equal to the pitch length. This means that a color will be reflected when the pitch is equal to the corresponding wavelength of light in the visible spectrum. Since temperature directly affects the molecule orientation between successive layers (see Figure 14), the pitch length changes with temperature, resulting in the alteration of the wavelength of reflected light, producing temperature-dependent color ranging from red (longest wavelength) to dark blue (shortest wavelength). An increase in temperature increases the angle between successive molecule layers, consequently tightening the pitch and shortening the wavelength. Similarly, a decrease in temperature increases the pitch length and the corresponding wavelength of light. The resulting color exhibited by the liquid crystals can then be calibrated to temperature using a thin foil thermocouple adhered to the test surface. This visible color play interval is both reversible and repeatable making thermochromatic liquid crystals ideal for temperature measurement across large surface areas of the experimental apparatus.

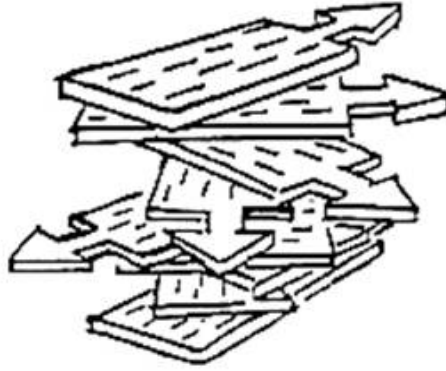


Figure 14 – Reorientation of TLC lattice structure [Jones (1992)]

Liquid crystals exist in a microencapsulated liquid solution, capable of chromatically indicating large ranges of temperatures ( $-30^{\circ}\text{C}$  to  $120^{\circ}\text{C}$ ) and bandwidths as small as  $0.5^{\circ}\text{C}$ , or as large as  $20^{\circ}\text{C}$  [Stasiek and Kowaleski (2002)]. For most transient experimental studies, a one degree-wide, narrowband crystal is used [Van Treuren et al. (1994), Lee et al. (1997), and Gao et al. (2003)] because of its sharp color transition and strong intensity definition; however, a single wideband crystal has also been used for color hue analysis [Bailey and Bunker (2002), Gao and Sunden (2002), and Saxena et al. (2003)]. The present study uses three one-degree wide crystals. Across this bandwidth, the crystal exhibits the entire color spectrum, from red at the lowest temperature to blue-violet at the highest temperature. When the temperature is outside of a crystal's bandwidth, the resulting color display is transparent. For heat transfer experimentation, the yellow-green color is the preferred indicator for temperature measurement because it corresponds with a peak in color intensity; however, exposure to ultra-violet light, oils, and chemical vapors can contaminate the experimental surface and severely diminish the TLC color intensity.

Liquid crystals exist in the mesophase, exhibiting a conjunction of both orderly arrangement (solid-like) and mobility (liquid-like). The tiny crystals are encapsulated by a very thin polymer membrane which helps to protect it from the effects of shear and pressure fluctuations generated in a heat transfer experiment; however, TLC remains very sensitive to touch and extreme heat. The encapsulated shell, with an approximate diameter of only 10  $\mu\text{m}$ , allows for a very thin layer of TLC, 20 to 30  $\mu\text{m}$  thick, to be applied to the target surface as in Figure 15. This thickness is considered thermally thin, allowing the crystal to respond to temperature change almost instantaneously ( $\approx 3$  ms) yielding accurate time-temperature thermography [Ireland and Jones (1987) and Stasiek and Kowaleski (2002)]. This response time is negligible in comparison with the total experiment time.

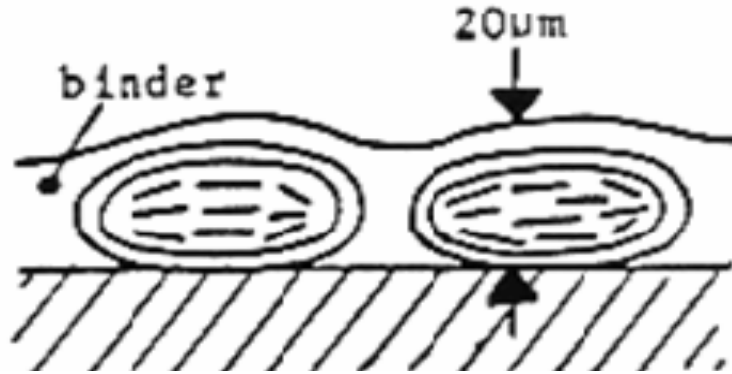


Figure 15 – Aqueous mixture of encapsulated crystals and binder solution [Jones (1991)]

### *Transient Liquid Crystal Technique*

The impingement of the heated air onto the target surface is a convective heat transfer problem with the local surface heat flux expressed as in Equation (6) previously:

$$q = h (T_{aw} - T_s) \quad (8)$$

where  $q$  is the local heat flux,  $h$  is the convection coefficient,  $T_{aw}$  is the adiabatic wall temperature (fluid temperature) that yields  $h$  independent of temperature, and  $T_s$  is the local surface temperature. The convection coefficient can be reduced to a function of only the flow field with an appropriate choice of the adiabatic wall temperature. For impingement experiments, where one-dimensional heat conduction behavior is assumed into the Plexiglas target surface, gas temperature differences are sufficiently small (around 20°C) that fluid properties can be assumed to remain constant and independent of the transient temperature.

The convection problem of impinging jets is considered a three-temperature situation involving the temperature of the fluid,  $T_{aw}$ , the temperature of the surface, and the initial jet temperature. Therefore,  $T_{aw}$  is the driving gas temperature in the heat flux equation. The temperature of the surface is determined by the transient response of the liquid crystal color play on the target surface. Initially, the target surface is at uniform temperature,  $T_i$ , and is suddenly exposed to the heated impingement air. The liquid crystal response for each surface pixel to reach a given temperature is dependent upon the adiabatic wall temperature and the local heat transfer coefficient at each pixel location.

The thermal conditions of a heat transfer experiment allow the lateral conduction of the target plate to be neglected compared to the convected heat from the bulk airflow because the principal form of heat transfer in the experiment is convection rather than conduction. The local heat transfer coefficients across a liquid crystal coated target surface can then be obtained using a semi-infinite solid assumption (see Figure 16) and solved using the one-dimensional Fourier equation:

$$k \frac{\partial^2 T}{\partial z^2} = \rho C_p \frac{\partial T}{\partial t} \quad (9)$$

with boundary and initial conditions:

$$-k \frac{\partial T}{\partial z} \Big|_{z=0} = h (T_{aw} - T_s)$$

$$T \Big|_{z=\infty} = T_i$$

$$T \Big|_{t=0} = T_i$$

where  $k$  is the coefficient of thermal conductivity of the substrate,  $z$  is the length in the heat flux direction,  $\rho$  is the density,  $C_p$  is the specific heat,  $t$  is time, and  $T_i$  is initial temperature. The equation applies the conservation of energy to the transient conduction problem by equating the net accumulation of heat per unit volume due to conduction (left-hand side) to the rate of change of thermal energy per unit volume within the substrate (right-hand side).

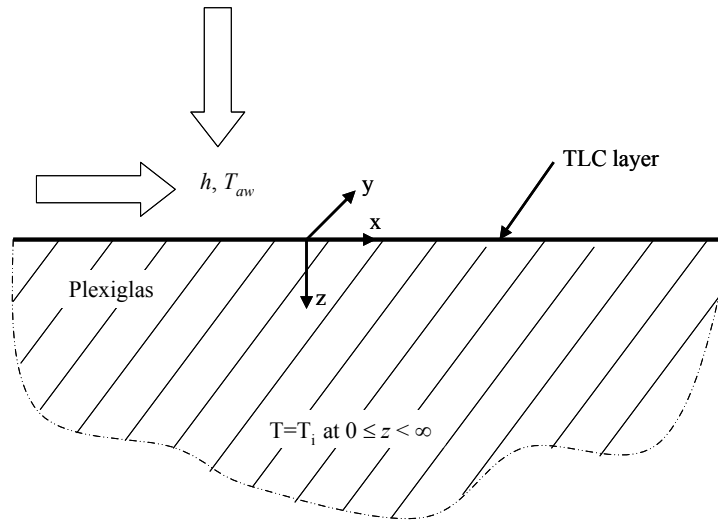


Figure 16 – Schematic of semi-infinite solid assumption

The constants of Equation (9) can be related by the thermal diffusivity,  $\alpha$ , which is a measure of the ratio of thermal conductivity to the material's thermal capacity, and is defined as:



$$\alpha = \frac{k}{\rho C_p} \quad (10)$$

The solution for the surface temperature response with time is:

$$\frac{T_s - T_i}{T_{aw} - T_i} = 1 - e^{\beta^2} \operatorname{erfc}(\beta) \quad (11)$$

where

$$\beta = \frac{h\sqrt{\alpha t}}{k}$$

and  $h$  and  $T_{aw}$  are unknown. Therefore, two events are required to solve for the unknowns. Using the double liquid crystal technique described in the subsequent section, the surface temperature at a particular time permits the simultaneous evaluation of the convective heat transfer coefficient and adiabatic wall temperature provided that all other parameters in Equation (11) are known.

Although the initial temperature of the Plexiglas is uniform at ambient temperature, the impinging fluid temperature is higher and not a true step increase. This is accounted for through the modification of Equation (11) by Duhamel's superposition theorem [Ireland et al. (1993)], which represents the temperature change as a series of steps described by:

$$T - T_i = \sum_{i=1}^N \left[ 1 - e^{\beta^2} \operatorname{erfc}(\beta) \right] \Delta T_{m,i} \quad (12)$$

where

$$\beta = \frac{h}{k} \sqrt{\alpha(t - \tau_i)}$$

and  $\tau_i$  is the time step for each temperature step,  $\Delta T_{m,i}$  is the temperature difference between each temperature step and the initial temperature, and  $T_i$ ,  $\alpha$ , and  $k$  are characteristic of the Plexiglas plate.

For this process to be employed, several assumptions must be satisfied. The present experiment involves a target plate of finite thickness. In order to satisfy the semi-infinite assumption, the transient temperature must not penetrate through the thickness of the plate during the test duration. This is achieved by a sufficiently thick plate of low thermal conductivity and diffusivity (0.187 W/m·K and  $0.1073 \times 10^{-6}$  m<sup>2</sup>/s for Plexiglas respectively). The semi-infinite assumption is governed by:

$$z > 4\sqrt{\alpha t} \quad (13)$$

which was developed by Schultz and Jones (1973) as a guideline for determining an acceptable target plate thickness,  $z$ . For the one-dimensional heat transfer assumption to be satisfied, conduction can only occur normal to the plate surface with all lateral conduction effects neglected. Although the plate may actually experience some small-scale lateral conduction, the dominant temperature gradient is in the direction perpendicular to the surface, and thus lateral effects are considered negligible.

#### *Double Crystal Technique Using Liquid Crystal Intensity*

For the double crystal technique to be used, the target surface must first be coated in at least two different liquid crystals. Bonnett (1989) showed that the brightness of a color response under fixed lighting conditions is not significantly affected by this thicker layer of liquid crystal, while Ireland and Jones (1987) determined that the crystal response time is also insignificantly affected. The double crystal method utilizes the peak value in intensity (or color brightness) emanated from the liquid crystal coated target surface, in

conjunction with the corresponding previously calibrated temperature value and measured test time. Using two different peak intensity values (i.e. two different  $t$  and  $T_s$  values) given by two different liquid crystal responses in a single transient test, two equations of the form in Equation (11) can be solved simultaneously for the unknown values of  $T_{aw}$  and  $h$ , thereby allowing a complete local heat transfer coefficient profile to be created across the entire experimental test surface. These intensity values are determined by a color image processing system used by Baughn and Shimizu (1989). The present study uses three narrowband crystals, of which, the two with the most definitive peak intensity values will be analyzed as described by the double crystal method by a color processing system which will be discussed in detail in Chapter 4.

## CHAPTER FOUR

### Design of the Experimental Jet Impingement Facility

#### *Introduction to the Experimental Design*

This chapter details the design and initial development of the Baylor University impinging jet test facility. The design was modeled after other impingement facilities and experimental flow systems, infusing the basic design concepts of the wind tunnel with advanced heating concepts and typical jet impingement array and flow configurations. The design will accurately model conventional engine representative conditions of impinging jets on a larger scale than has been previously documented. The facility establishes the premise of the current study and creates a cornerstone toward the development of future jet impingement studies.

#### *Experimental Apparatus Overview*

The experimental apparatus (Figure 17) was designed to be compatible with a variety of jet impingement array configurations. The facility consists of a blower fan, diffuser plenum, flow straighteners, heater mesh, impingement and target plates, three-chip CCD camera, and image processing system. An overhead model of the experimental apparatus is presented in Figure 18. Air is supplied to the experimental facility by a variable speed blower fan and the flowrate measured with an Oripac orifice meter. The desired mass flow rate is established by measuring the differential pressure across the orifice and matching the reading with the manufacturer-supplied calibration curve. This is used to set

the desired jet Reynolds number based on the 0.7344 in (18.65 mm) impingement hole diameter [Robertson and Van Treuren (2005)].

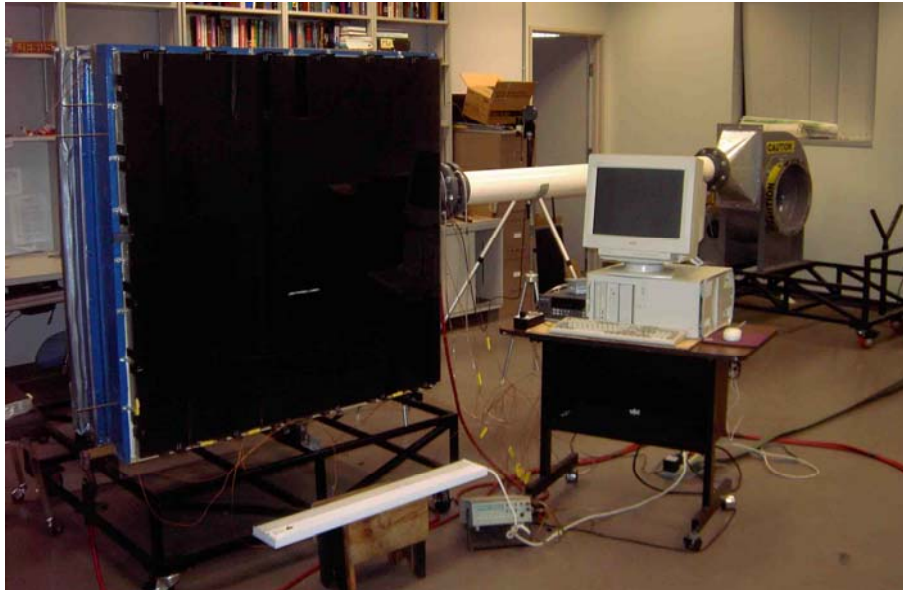


Figure 17 – Baylor University impinging jet test facility

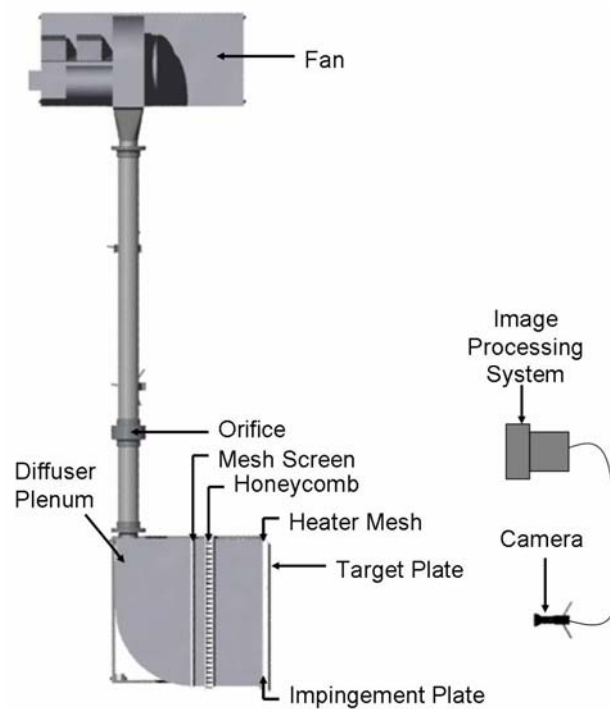


Figure 18 – Experimental Facility [Robertson and Van Treuren (2005)]

Airflow reaches the impingement plate after first entering the diffuser plenum. The plenum accepts air from downstream of the orifice plate and serves to both reduce the bulk air velocity and diffuse the concentrated air jet across the entire span of the chamber. The flow then enters a series of flow straighteners which assist in minimizing flow turbulence by providing a pressure drop that promotes uniform flow.

The heater mesh method developed by Gillespie (1993) is used to heat the air just prior to impingement. The mesh consists of a 40  $\mu\text{m}$  316-stainless steel fine wire mesh with a 0.38 open area ratio soldered between two brass bus bars. A Miller Syncrowave 250 arc welder is connected to the brass bars to provide heating to the mesh [Robertson and Van Treuren (2005)].

The heated air impinges on a target plate coated with thermochromatic liquid crystals. A coating that combines three different encapsulated liquid crystals (R25C1W, R30C1W, and R35C1W) is used to measure the surface temperature created by the impinging jets. The system is designed with fluorescent lights mounted on the frame to ensure uniform, non-heated lighting and a three-chip CCD camera is used to capture the transient process. The video feed is transferred into a standard IEEE-1394 (FireWire) PC card and successive images are captured by a LabVIEW program. The image capture rate is 30 frames per second [Robertson and Van Treuren (2005)]. The local heat transfer coefficients and adiabatic wall temperature were determined using a visual technique employed by Li et al. (1988) and Jones (1992).

### *Experimental Design and Component Sizing*

#### *Prediction of Flow Losses in the Facility*

The design of the impinging jet testing facility was developed through an iterative theoretical analysis involving a Loss Calculator that predicted the pressure loss through each component and then fit a theoretical curve predicting head loss as a function of air flowrate against the manufacturer's data. The main purpose of the theoretical study was to determine the largest possible impingement hole capable of producing engine representative Reynolds numbers of nearly 15,000 to 45,000 in a large 8 x 8 array.

The calculator was therefore used as the determination factor for component sizing. It was created with the idea that given several "desired" inputs, the resulting sizes of the dependent components could be sized. The input cells are highlighted in yellow in the calculation program (Appendix A). These include the desired number of holes in the streamwise and spanwise direction as well as the hole spacing. These were the first factors considered in the calculator's computation as it was most important to be sure that the array geometry would be representative of other typical array configurations. Other input factors are determined by the surroundings, such as room temperature, which generates the air density and viscosity by interpolating values from an air properties table taken from Munson et al. (2002). The jet temperature does a similar calculation based upon the desired input and produces an estimate of the jet Reynolds number. Several more parameters are used to help determine the overall system length, although their inputs are based upon some standard sizes and are therefore fixed. These include the mesh and heater mesh wire diameter, the fan's cart depth, and the required camera distance from the test plate. The remaining inputs; pipe diameter, orifice inner (bore)

diameter, hole diameter, and input flowrate; provide the means of the iterative theoretical analysis.

Through an iterative approach, the effects of altering these parameters can be seen on the jet Reynolds number, predicted system head loss, and overall facility length. A compromise must therefore be made between these parameters to maximize the facility's capabilities within the confines of the room dimensions. With these component sizings in place, an estimate of the facility's capabilities can be predicted as governed by Figure 19.

The Loss Calculator prediction begins with the input flowrate entered at the fan local control panel. The calculator then computes local velocities through each component based upon the sizing criteria. Using the component loss coefficients and overall pressure loss equations determined in the following sections, the actual loss in the system can be calculated by the sum of each component's contribution to the overall system pressure loss:

$$h_{L,overall} = \sum h_{L,components} \quad (14)$$

where the component losses are found from the forms of Equations (15) through (17), which will be discussed in detail. All required parameters used in these equations, such as friction factor, air properties, and water properties are automatically interpolated from tables extracted from Munson et al. (2002) based upon the input criteria. After all the inputs have been entered into the calculator, the calculator produces the predicted overall system pressure loss, jet Reynolds number, and minimum overall facility length. By this means, the facility was predicted to produce a maximum fluid flowrate of 1350 m<sup>3</sup>/s (47,674 ft<sup>3</sup>/s), which yields an impingement hole of 0.7344 in (18.65 mm) for jet



Reynolds numbers of nearly 15,000 to 45,000 and an overall facility length of 20.5 feet (6.25 m).

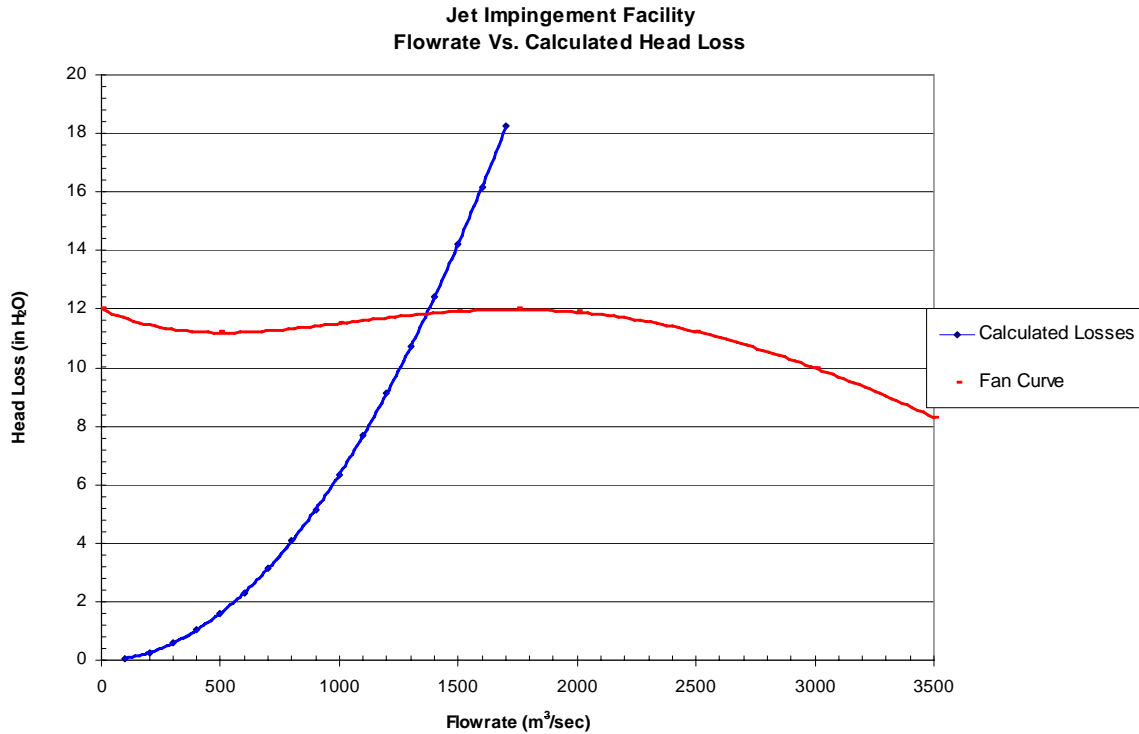


Figure 19 – Prediction curve for maximum fluid flowrate

### *Fan Selection*

From the literature, several choices were available to supply the airflow to the system. The air compressor used by San and Lai (2001) and Bailey and Bunker (2002) is capable of supplying high Reynolds number values (up to 65000 [Bailey and Bunker (2002)]), but without the use of pressure regulators and valves to meter the air supply, the cyclic nature of a compressor would produce large fluctuations in flow velocity and uniformity. These instabilities would then require either a greater upstream pipe length, or more screens (both of which produce more flow losses) to help promote flow uniformity. Suction-type fans offer the advantage of greater flow uniformity, but are limited in their

ability to produce high Reynolds numbers, which forces smaller jet diameters. Van Treuren et al. (1996) achieved Reynolds numbers in the range of 10,000 to 34,000 using a vacuum pump to draw the air through the experimental facility and impinge with a small array of 5 mm (0.197 in) jet diameter holes. The suction fan also requires a large contoured inlet which demands additional room space for the air to enter. The centrifugal blower fan alleviates the space restriction by instilling a side-inlet design and offers the necessary power to achieve typical engine representative Reynolds numbers with the much desired large-scale jet hole design which is large enough to allow future hot-wire studies. The blower fan does however produce some small-scale pulsations; however, these are sufficiently low, even at off-design operation. The centrifugal blower fan therefore runs with reasonable steadiness and efficiency across a large range of flow conditions, making it ideal for the current wind tunnel design [Mehta and Bradshaw (1979)]. For the present study, air will be supplied to the system by a Cincinnati Centrifugal Blower Fan model HDBI-160 (Figure 20). The fan drives the open circuit facility upstream of the test section and will be capable of driving jet Reynolds numbers in the range of 10,000 to 50,000 with a much larger jet diameter of 0.7344 inches.



Figure 20 – Blower fan and nozzle for the current facility

The fan delivers the airflow to the system through a nozzle which serves to transition the flow from the large 10 inch by 18 inch rectangular fan exit into the 6 inch diameter PVC pipe. The nozzle contour helps to minimize system flow losses and reduce percentage fluctuations by increasing the velocity without altering the total pressure [Mehta and Bradshaw (1979)]. This creates a loss coefficient,  $K_L$ , of only 0.07 for the 30 degree nozzle as opposed to a 0.43 loss coefficient for a sudden contraction design based upon the pre- and post-contraction areas [Munson et al. (2002)]. This produces an overall system loss,  $h_L$ , of:

$$h_L = K_L \frac{V^2}{2g} \quad (15)$$

where  $V$  is the velocity through the exit of the nozzle and  $g$  is the gravitational constant. The contraction also serves to reduce both the mean and fluctuating velocity variations to a smaller fraction of the average velocity exiting the blower [Mehta and Bradshaw (1979)].

#### *Piping and Orifice Plate*

The piping network consists of an orifice between two lengths of pipe: the 90 inch upstream (of the orifice) pipe and the 30 inch downstream (of the orifice) pipe. The orifice was chosen with a large diameter ratio,  $\beta$ , of 0.80 to again minimize the flow losses by creating a greater orifice flow coefficient,  $F_o = 0.83$  [Holman (2001)]. This translates to a total system loss of:

$$h_L = \left( \frac{Q}{F_o A_{o,i}} \right)^2 \left( \frac{1 - \beta^4}{2g} \right) \quad (16)$$

through the orifice, where  $Q$  is the flowrate through the orifice and  $A_{o,i}$  is the orifice inner bore diameter. The  $\beta$  value is also used to determine the two pipe section lengths from the British Standards for Fluid Flow in Closed Conduits (1989). A minimum distance of  $15d$  is required upstream of the orifice to ensure that flow has reached a fully developed state. Similarly, a  $5d$  distance is used in the downstream pipe section to allow the effects of the orifice contraction to settle [British Standards (1989)]. A large pipe diameter (6 inch PVC) was chosen to help reduce the flowrate through the pipe. This also reduces flow loss which is directly proportional to the square of the velocity of the fluid within the pipe, and is given by the following:

$$h_L = f \frac{\ell}{d} \frac{V^2}{2g} \quad (17)$$

where  $h_L$  is the head loss,  $f$  is the friction factor determined from the Moody Chart [Munson et al. (2002)],  $\ell$  is the length of the pipe,  $d$  is the pipe diameter,  $V$  is the fluid velocity in the pipe, and  $g$  is gravity. A simple calculation with the losses calculator of Appendix A reveals that the use of a 6 inch pipe produces 80 percent savings in flow loss versus a 4 inch pipe, which translates into the ability for the facility to push higher Reynolds numbers though the impingement plate. However, an 8 inch pipe requires 40 inches in length more than the 6 inch pipe. Therefore, the diameter of the pipe was limited by the standard length requirements mentioned earlier, and a tradeoff between loss and length must be considered. Ultimately, the 6 inch PVC pipe was selected because it produced the least flow loss for the dimension requirements of the room.

Between the two pipe sections, an Oripac orifice meter (Model 4150) measures the system flowrate by a pressure differential. The meter is tapped for pressure readings both upstream and downstream of the contraction. The pressure differential is then fit to a

manufacturer's supplied data curve (see Appendix B) which allows for the determination of the fluid flowrate. This fluid flowrate is then used to calculate the average ideal jet Reynolds number for the flow setting.

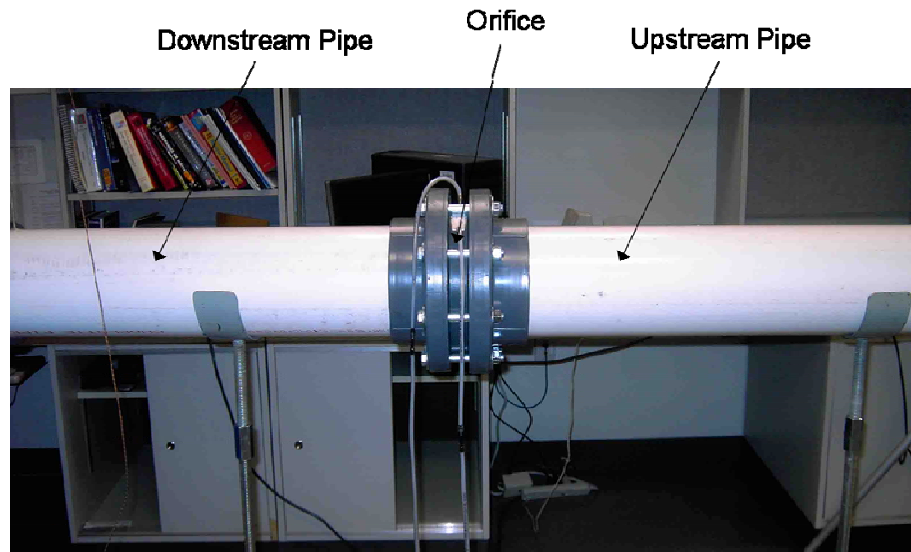


Figure 21 – Side view of the orifice and piping for the current facility

### *Diffuser Plenum*

Airflow from the downstream pipe empties into the diffuser plenum. The incoming air is immediately met by two radiused diverter plates (Figure 22) which divide the incoming air into three sections, thereby facilitating the diffusion of the concentrated air jet across the entire height of the chamber. As the air spreads across the plenum, it is again met by two more radiused diverter plates (Figure 23) spanning the height of the plenum. Each plate is set 2 inches inward from the front and back of the plenum inlet hole in order to evenly divide the air and promote even diffusion across the width of the chamber, as well as turn the flow towards the plenum exit. The back wall of the diffuser plenum is also radiused to facilitate the 90 degree turn.

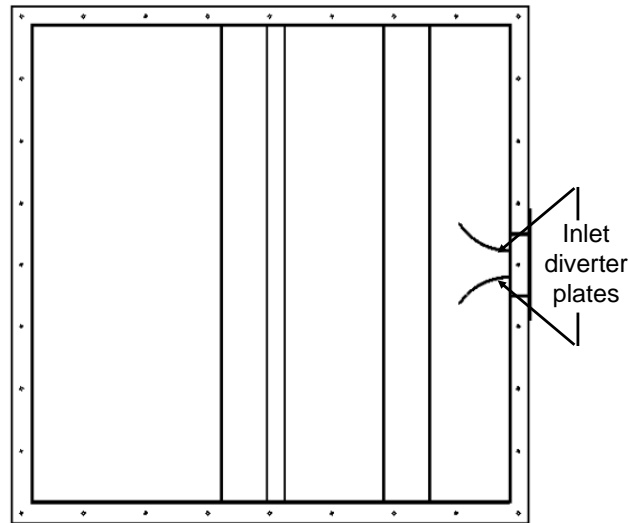


Figure 22 – Inlet diverter plates to the diffuser plenum  
[Robertson and Van Treuren (2005)]

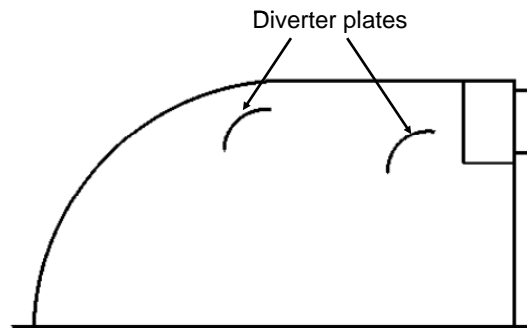


Figure 23 – Flow diverter plates in the plenum chamber  
[Robertson and Van Treuren (2005)]

The plenum and guide vanes are radiused for several reasons. The first is to minimize the flow losses to the system. Instituting guide vanes across a 90 degree mitered bend produces a loss coefficient of 0.2 compared to that of 1.1 without the diverter plates [Munson et al. (2002)]. This reduces the total losses seen by the system, which serves to permit a greater flow velocity, and thus, greater jet Reynolds numbers or greater jet hole diameters. The second reason is to minimize separated flow regions. Guide vanes help to turn more of the flow quicker, as shown in Figure 24(b). Without the flow diverters, the

fluid would turn with a larger radius proportional to its flow velocity (i.e. the greater the velocity, the less inclination of the flow to turn). This means that the bulk flow would be forced to the far side wall of the turned plenum, creating a region of flow separation at the near wall of the bend as seen in Figure 24(a).

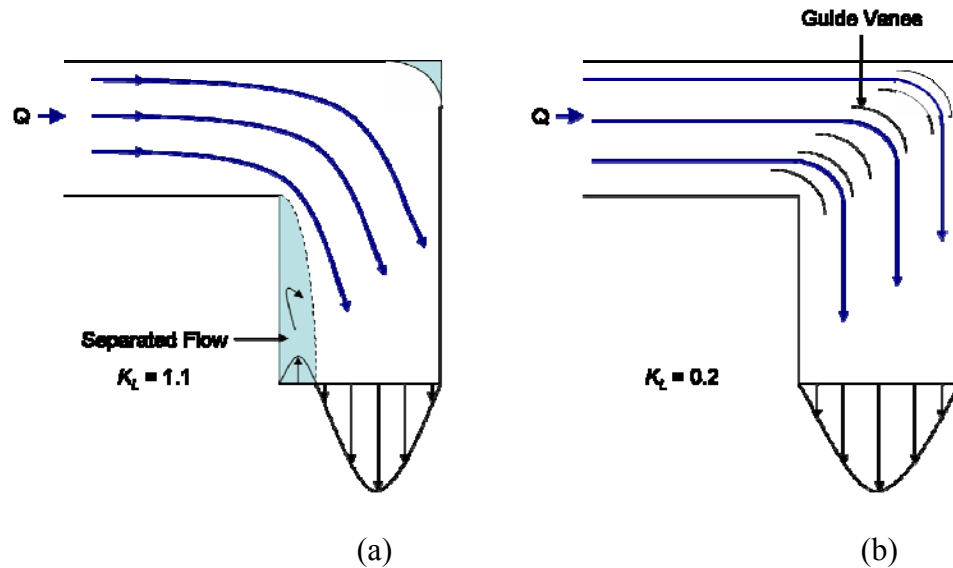


Figure 24 – Flow characteristics in a 90 degree bend: (a) without guide vanes, (b) with guide vanes

The third, and probably most important reason, is simply for space purposes. Room 102 at Baylor University, where the facility is located, is 23 ft in its longest direction. Therefore, the total length of the testing facility and required system analysis tools could not exceed this dimension. With the already established dimensions of the fan, lengths of the piping, and including a sufficient distance for camera placement, a typical wide-angle conical diffuser would not fit within the room dimensions. For a conical diffuser to see a benefit in its loss coefficient compared to that of the current 90 degree design, it would require no greater than a 35 degree diffusion angle [Munson et al. (2002)]. This would produce a diffuser length more than 3 feet longer than the 90 degree

design, and would exceed the dimensions of the room. Although a greater diffusion angle would shorten this plenum length, the increased expansion would essentially generate no difference in diffusion capability or corresponding flow losses as compared to the current design since it would simply be seen as a common sudden expansion. Consequently, the 90 degree bend was implemented to create greater experimental versatility and ensure that the facility would be able to remain in the same laboratory room even if the test section were elongated to support greater  $z/d$  spacings.

As the name implies, the plenum serves to “diffuse” the concentrated stream of air from the downstream pipe. Therefore, the fluid must flow from a lesser area to a greater area. The basic dimensions of the diffuser plenum include a 47 in x 47 in (1.19 m x 1.19 m) exit area that is 24 in (0.61 m) deep. The diffusion of the pipe airflow into the diffuser plenum can be seen as a sudden expansion. Although the inlet diverter plates of Figure 22 would help to diminish the losses of such a case, a conservative estimate of the flow losses was considered which neglects their loss reduction effects. This was done to ensure that the calculated facility component dimensions determined by the losses calculator would be capable of producing the desired jet Reynolds numbers. Therefore, considering the conservation of mass, momentum, and energy equations, the loss coefficient associated with this sudden expansion can be expressed as:

$$K_L = \left(1 - \frac{A_1}{A_2}\right)^2 \quad (18)$$

where  $A_1$  is the upstream area (area of the pipe) and  $A_2$  is the downstream area (cross-sectional area of the diffuser plenum). A calculation reveals that the associated loss coefficient is 0.95. The diffuser plenum as a whole sees both the losses due to the 90 degree bend as well as those due to the sudden expansion. Therefore, the total loss



coefficient created in the diffuser plenum is simply a sum of the component losses, or  $K_L = 1.15$ , and the total system loss is given by Equation (15).

### *Flow Straighteners*

According to the conservation of mass, the mass flowrate in the pipe must equal that in the plenum. Therefore, the larger plenum area also serves to slow the airflow velocity as governed by the following:

$$\rho A_1 V_1 = \rho A_2 V_2 \quad (19)$$

where  $V_1$  is the velocity in the pipe and  $V_2$  is that in the plenum. The flow immediately following the bend in the diffuser is non-uniform, and therefore, a series of flow screens serve to promote uniformity and reduce turbulence and pressure fluctuations. The flow conditioners consist of a sequence of one honeycomb section followed by two stainless steel mesh screens. The honeycomb panel produces a relatively low pressure drop, rendering it rather ineffective against streamwise non-uniformities and fluctuations [Lindgren and Johansson (2002)]. However, honeycomb is very effective in reducing the lateral components of the mean velocity and of the larger turbulent eddies, thereby minimizing flow swirl, and straightening the flow path from the 90 degree turn to be normal to the flow exit plane [Mehta and Bradshaw (1979)]. Generally, the panel will break up eddies larger than the cell size and reduce the overall free-stream turbulence level [Lindgren and Johansson (2002)]. The effectiveness of a honeycomb panel in reducing these cross-stream fluctuations is attributed to the nature of the cell grid which is elongated in the flow direction, but a sufficient length of six to eight cell diameters is necessary for its effects to be realized [Mehta and Bradshaw (1979)]. The honeycomb panel used in the present study is 2 inches (5.08 cm) thick with a 0.25 inch (0.635 cm) cell

diameter, thereby meeting the requirements for an adequate honeycomb section size. The honeycomb itself will actually produce some turbulence of its own on the same order as the cell diameter. This turbulence diminishes much slower than that from a screen, and therefore, two successive screens follow the honeycomb section to reduce this turbulence effect.

The idea of a mesh screen to enhance flow uniformity was first proposed by Prandtl (1932) and has been frequently implemented in impinging jet facility designs such as those used in the experimental work of Van Treuren (1994), Gao et al, (2003), and Saxena et al. (2003), just to name a few. Screens, much like contractions, serve to reduce the longitudinal components of turbulence and promote more uniform flow profiles by imposing a static pressure drop proportional to the square of the approaching velocity and the loss coefficient. The loss coefficient was quantified by Wieghardt (1953) as:

$$K_L = 6.5 \frac{(1-\beta)}{\beta^2} \left( \frac{Vd}{\beta\nu} \right)^{-1/3} \quad (20)$$

where  $\beta$  is the open area ratio,  $V$  is the approaching velocity,  $d$  is the wire diameter, and  $\nu$  is the dynamic viscosity. The equation shows that the loss coefficient is inversely proportional to the approaching velocity; therefore, the reduction in plenum velocity as determined from Equation (19) will produce a larger pressure drop across the screen. At first this may seem like an adverse effect as the previous components were sized to minimize flow losses; however, according to Mehta and Bradshaw (1979), a large  $K_L$  is necessary to promote a sufficient pressure drop that will effectively remove the mean velocity fluctuations. It was found that a  $K_L$  value of approximately 2.8 will eliminate the majority of flow unsteadiness. Therefore, the higher loss coefficient created by the

reduced flowrate is actually desirable, and in turn, the small velocity produces an insignificant contribution to the overall system pressure loss which is determined by Equation (15). For the current blower fan capabilities, a loss coefficient in the range of 4.4 to 6.2 is produced in the screens.

The screen is essentially a hydrodynamic resistance to the flow that, when confined within a constant area flow path such as the plenum box, experiences a drag force. This drag force reduces the total pressure of the air flowing through the screen without affecting the local average velocities; however, where the local velocity is higher than the average, the drag force will also be higher, thus, tending to equalize the total pressure across the plenum cross section effectively reducing velocity variations [Mehta and Bradshaw (1979)]. The combination of several screens in series will significantly reduce these mean velocity fluctuations and turbulence to an acceptable level,

For the current facility design, two standard 0.011 inch (0.2794 mm) wire diameter mill-grade mesh screens with an open-area ratio of 0.51 were used in conjunction with the honeycomb panel to promote a uniform flow field. The first screen was placed directly at the exit of the honeycomb panel to encourage the reduction of both longitudinal and lateral fluctuations. A 5.5 inch (13.97 cm) settling chamber was installed before the next successive mesh because, as with the exit of the honeycomb, the exit of the screens also produces a small amount of turbulence, although much less than would be at the exit of a honeycomb alone. A  $500d$  distance is thus required post-mesh to allow the small amount of wire-induced turbulence to decay [Cheong (2002)]. A second mesh of the same proportions as the first then serves to further eliminate the velocity fluctuations, and a

second 5.5 inch settling chamber is again affixed to the facility to allow the slight flow unsteadiness to settle.

Screens successfully reduce the streamwise components of turbulence; however, they are not as successful in reducing the lateral components. Therefore, the honeycomb-screen combination, which effectively reduces both lateral and longitudinal non-uniformities and fluctuations, is ideal for basic wind tunnel design and the present facility development. Figure 25 shows a side view of the plenum chamber and the sections following its exit.

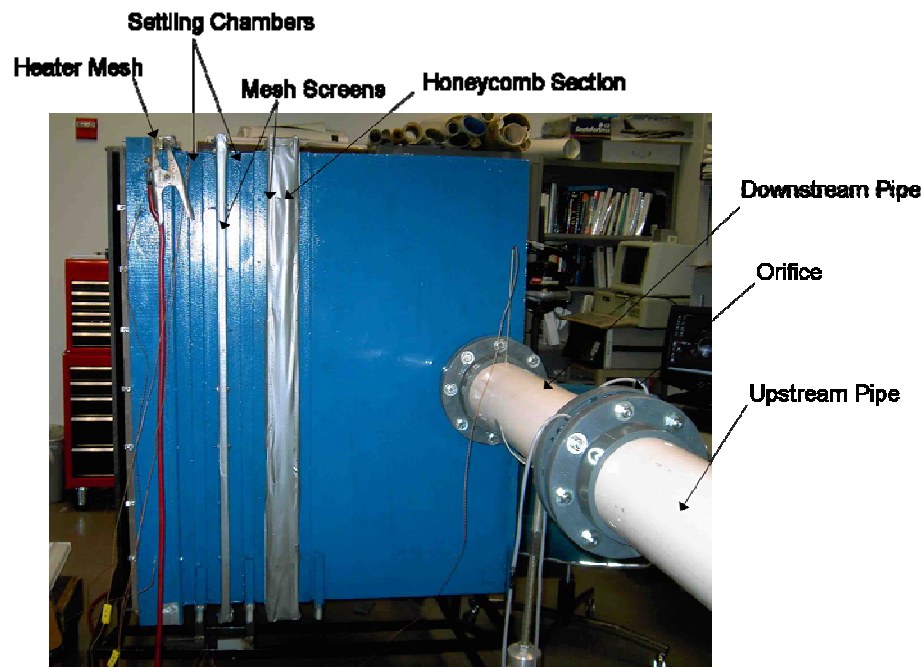


Figure 25 – Plenum sections side view of the current facility

#### *Heater Mesh*

Following the two 0.51 open-area ratio screens, is a third screen of 0.38 open-area ratio. This screen serves two purposes. The first is to provide one final mesh screen to reduce any remaining flow uniformities. Groth (1991) determined that a cascade of

successive wire mesh screens of progressively finer mesh serves to reduce flow variation substantially. This is again accomplished with a nearly non-existent effect to the overall system pressure loss due to the same low-velocity flow condition found with the previous screen sections. The second reason is to provide heating to the facility through a heater mesh component first developed by Gillespie (1993). However, several other methods of heating the airflow have also been used in experimental heat transfer facilities. One method involves pre-heating the flow and using valves to divert it away from the test section until a steady state flow temperature has been reached. When the flow reaches thermal equilibrium, the valves are quickly switched and airflow is allowed to pass through the test section providing a near step increase in temperature [see Van Treuren et al. (1994), Gao et al. (2003), and Kanokjaruvijit and Martinez-Botas (2003)]. Other methods involve heating the target surface rather than the airflow to examine the convective heat transfer effects [San and Lai (2001)]. However, for the current design, the heater mesh concept was implemented.

The heater mesh provides several advantages. First, the need for a fast acting valve system is avoided. This allows for multiple experiments to be run in a short time frame since there is a shorter waiting period for the test section to return to ambient temperature. The nature of the heater mesh itself, thus, simplifies the heating process and allows for rapid temperature switching in low-speed flows. Although the change in temperature is not considered a true step-change ( $< 0.1$  sec), the time constant can easily be accounted for by Duhamel's Superposition Principle (Equation (12)) presented in Chapter Three.

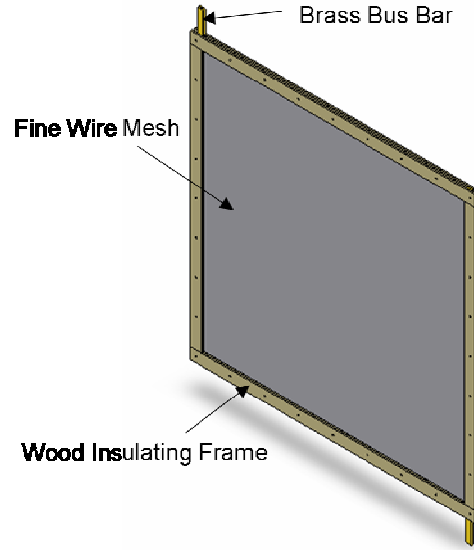


Figure 26 – Heater mesh component schematic

The heater mesh (Figure 26) is created by soldering a 316-stainless steel fine-wire ( $40\text{ }\mu\text{m} / 1.575 \times 10^{-3}$  in diameter) mesh between two sets of brass bus bars using silver solder (see Appendix C for mesh production instructions). The mesh is housed within a wooden frame which helps to insulate the heat and ensure greater heater efficiency. This efficiency can be found by:

$$\eta = \frac{T_{down} - T_{up}}{T_{mesh} - T_{up}} \quad (21)$$

where  $T_{down}$  is the temperature downstream of the mesh,  $T_{up}$  is the temperature upstream of the mesh, and  $T_{mesh}$  is the actual temperature of the heated mesh. A typical heater mesh efficiency is approximately 0.55, which means that the mesh temperature is roughly twice the temperature difference from the inlet air as the exit temperature is from the inlet [Cheong (2002) and Ireland (2005)]. A simple current-producing device, such as an arc welder or car battery, is connected to the brass bus bars to provide energy to the mesh, and

thus, the airflow. A downstream temperature produced by such a device is determined with the known power output by:

$$T_{down} = \frac{IV}{\dot{m}c_p} + T_{up} \quad (22)$$

where  $I$  and  $V$  are the supplied current and voltage respectively,  $\dot{m}$  is the mass flowrate, and  $c_p$  is the coefficient of heat. For the arc welder, the amperage is simply a dial adjustment, and the associated voltage can be measured by a Phillips PM2525 Multimeter with leads connected to the welder electrodes. For a car battery, the battery voltage and the natural resistance of the mesh (approximately  $0.074 \, \Omega$  – see Appendix D) draw enough current necessary to satisfy Ohm's Law ( $V = IR$ ). The current can then be used with the voltage measure and Equation (22) to determine the downstream temperature. For the present design, a Miller Syncrowave 250 arc welder provides sufficient power to produce almost  $47^\circ\text{C}$  ( $116.6^\circ\text{F}$ ) downstream of the mesh by providing 18.5 volts DC and 250 amps for a mass flowrate of  $0.2 \, \text{kg/s}$  ( $0.441 \, \text{lb}_m/\text{s}$ ).

### *Test Section*

Once the air is heated, it travels a 3.5 inch settling chamber before encountering the test section. The test section consists of an impingement plate, target plate, and spacers as seen in Figure 27. The entire test section is constructed out of Plexiglas whose material properties make it an ideal candidate for experimentation. The low thermal conductivity and diffusivity of Plexiglas permit the use of the one-dimensional semi-infinite solid assumption and also serves to naturally insulate the test section thereby ensuring that the only heat effect is the convective heat transfer of the jets acting on the target surface. The transparency of Plexiglas is also beneficial because it allows for the

liquid crystal thermal profile to be visible through the Plexiglas. A camera system can therefore be set up behind the test plate and still collect the transient experiment images for post-processing analysis.

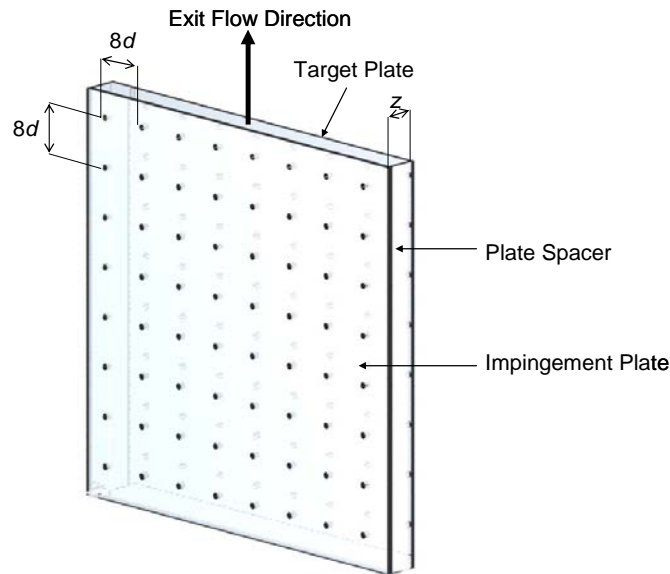
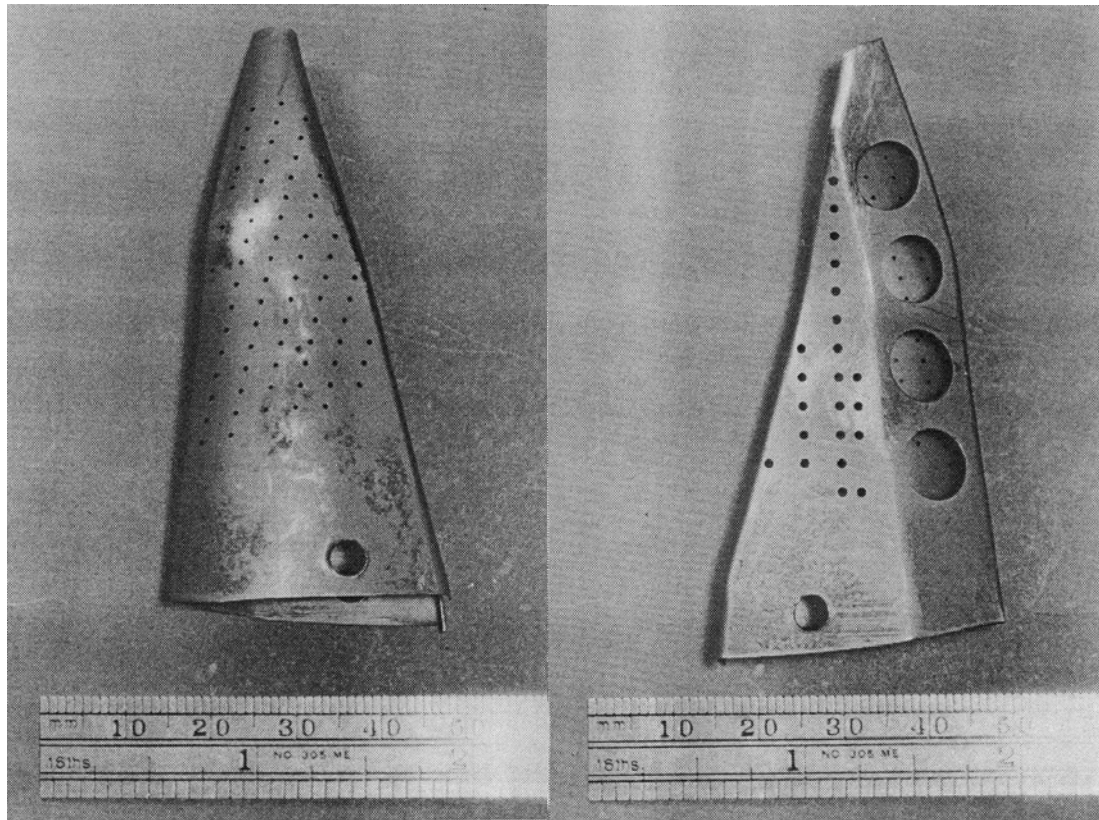


Figure 27 – Impingement array geometry [Robertson and Van Treuren (2005)]

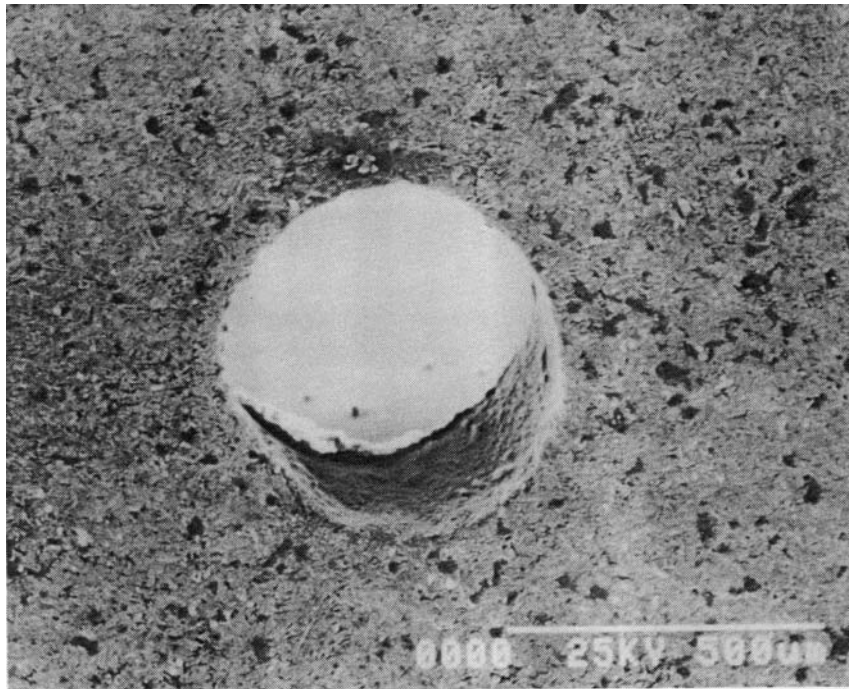
The array geometry is modeled after the works of Kercher and Tabakoff (1970), Van Treuren et al. (1994), and Kanokjaruvijit and Martinez-Botas (2003), among others. The impingement plate is an 8 x 8 jet array of 0.7344 in (18.65 mm) diameter holes, uniformly spaced  $8d$  in both the streamwise and spanwise directions as shown in Figure 27. The impingement holes in the array are sharp-edged to be indicative of current turbine blade design which utilizes rows of laser-drilled holes. Van Treuren (1994) presented detailed turbine blade images in which the jet hole was examined under a scanning electron microscope to enhance the visual geometry of the hole. Figures 28(a)-(c) show an actual turbine blade insert from this study.





(a) Suction surface

(b) Pressure surface



(c) Jet hole

Figure 28 – Sample turbine blade impingement hole geometry from a formerly operational Rolls Royce engine [Van Treuren (1994)]

Figure 28(a) shows an inline array on the blade suction surface with jet hole diameters of 0.48 mm (0.189 in) and an  $\ell/d$  of 0.75. The hole spacing is  $7d$  in the streamwise and  $5d$  spanwise with the number of spanwise holes ranging from two to six for a given streamwise row, with the larger occurring in the midspan region. The pressure side (Figure 28(b)) jet hole diameter is almost twice as large at 0.95 mm (0.374 in), while spacing is about half. These figures and data, courtesy of Van Treuren (1994), help provide a visual basis for the chosen impingement array model developed in the current study. The inline array is not only representative of current impingement models (examined in Chapter 2), but it is also very characteristic of the actual turbine blade. Also, the current model contains impinging jet hole diameters approximately 20 to 39 times that in an actual gas turbine engine and nearly three to four times larger than any facility of comparable array size and jet Reynolds numbers, thereby satisfying the first objective outlined at the close of Chapter 1.

The 8 x 8 geometry was chosen to be very representative of the literature. This will allow for accurate comparison between the results of the current facility and that of previous designs. Although the array seems much larger than that of the actual turbine blade as seen in Figure 25, the enlarged design allows for the examination of the middle jet section, away from the upper and lower walls and their associated boundary layers, so that simply the effects of the impinging jets themselves may be analyzed accurately. The enlarged hole size was also chosen for several reasons. The first is so that a more detailed assessment of the heat transfer effects of an array of impinging jets could be analyzed than ever before. To the author's knowledge, no other experimental facility contains an array of jet holes as large as the present design while still capable of delivering jet Reynolds

numbers of 45,000. This enlarged jet area will allow for the heat transfer features of the impinging jet to also be enlarged, and thus, analyzed in greater detail to better determine the characteristic nature of their heat transfer effects. The larger jet diameter will also provide enough area for a hotwire or computational fluid dynamics (CFD) study on the same impingement array.

Figure 27 also shows a plate spacer between the impingement and target plates. This serves to confine the test section on three sides, allowing spent air to exit in only one direction which represents the post-impingement flow across the surface of a turbine blade within a gas turbine engine. This spacer is placed at one diameter distance from the exit of the jet hole to allow for accurate comparison with the literature, such as Florschuetz et al. (1981), Van Treuren (1994), and Gao et al. (2003).

The heated air impinges upon a liquid crystal coated target surface. The surface provides a chromatic temperature profile of the jet-induced heat transfer which, when used in conjunction with its corresponding time required to reach the indicated temperature, allows for the determination of the local heat transfer coefficient and adiabatic wall temperature. Liquid crystals were used because of their significant advantage over thermocouples. Firstly, liquid crystals are much quicker to implement than adhering thermocouples to the test plate at all desirable locations. Liquid crystals are applied to the test surface by an air brush. With this technique, a thermally thin layer of approximately 20  $\mu\text{m}$  can easily be applied to the test surface. Secondly, liquid crystals create a continuous surface model flow field that thermocouples cannot. Thermocouples are unable to give an exact temperature at every point on the test surface due to the nature of their construction. They require wire leads either to run through or across the test plate.

For either situation, extreme care must be taken to ensure that the target surface is smooth to prevent tripping the boundary layer which can introduce conditions that will affect the jet heat transfer investigation. Liquid crystals remove this situation as the entire surface is uniformly coated in the crystal itself to provide a smooth test surface. However, the use of liquid crystals does require some form of temperature measurement whereby the liquid crystal color intensity at a particular location can be compared to a known value of temperature so that a calibration curve can be created. Therefore, four surface thermocouples are applied to the target surface by means of a thin layer of adhesive glue. Two thermocouples are applied between jets, and two are applied at the center of the jets as shown in Figure 29. The calibration technique is discussed in Chapter Five.

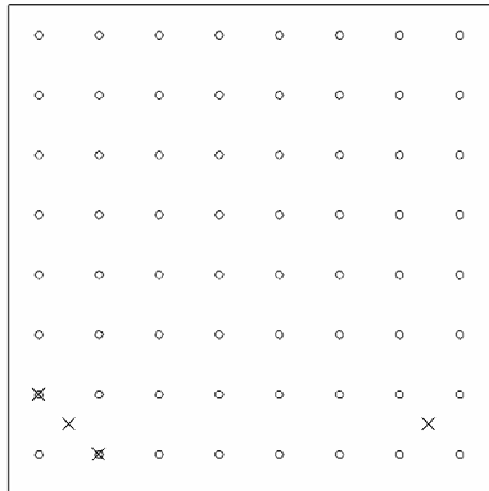


Figure 29 – Surface thermocouple locations (indicated by an “x”)

The main form of temperature measurement for the current study however, uses three crystals applied to the target surface. Although the double crystal technique described in Chapter Three outlines the need for only two crystals, the third is used mainly to provide longer test times in the regions of high heat transfer. With a large enough

temperature difference created by the heater mesh, so that the third crystal can provide a sharp enough peak in intensity, it can also provide an extra check in the heat transfer coefficient calculation as well.

The present study uses one-degree wide liquid crystals. This creates a sharp color contrast that provides the clear peak in intensity necessary to accurately determine the associated specific time to calculate the heat transfer coefficient in Equation (11). However, care must be taken in choosing the operating temperature of the crystal to minimize the experimental uncertainty. The crystal temperatures must demonstrate sufficient separation so as not to exhibit interfering color play intervals, and the difference between the driving gas temperature and these crystal temperatures must be large enough to minimize errors by ensuring a definitive intensity peak [Van Treuren (1994)]. For this reason, a 25°C, 30°C, and 35°C crystal combination was used (Hallcrest R25C1W, R30C1W, and R35C1W).

### *Image and Data Acquisition*

In order to better visualize the liquid crystal, a thin layer of aqueous black backing paint (Hallcrest BB-G1) is applied to the target surface after the three liquid crystal layers have already been sprayed. The coating on the target surface is illustrated by Figure 30. The black paint simply provides a dark contrast to the bright display of the liquid crystal so that the visual heat transfer is more vibrant. To ensure that the camera system will only capture the color intensity emanated from the crystals, the test is performed, with the test plate illuminated only by a controlled light source. For this purpose, a fluorescent light is mounted both above and below the test section to provide uniform lighting. A typical incandescent light source would not suffice for experimentation because of the nature in

which it produces light. The incandescent light bulb glows because electricity flows through a filament, which offers resistance, which transforms the electrical energy into heat, much like how the resistance in the heater mesh creates heat when supplied with power from a car battery. This heat makes the filament white hot, thereby producing light. On the other hand, fluorescent lights use electric current to stimulate mercury atoms, causing them to release ultraviolet photons, which in turn stimulate phosphors. These phosphors emit visible light photons creating a four to six times more efficient, non-heating, “cool” light. Therefore, fluorescent lights provide the illumination necessary to view the crystal’s color play without contributing additional heat to the test plate.

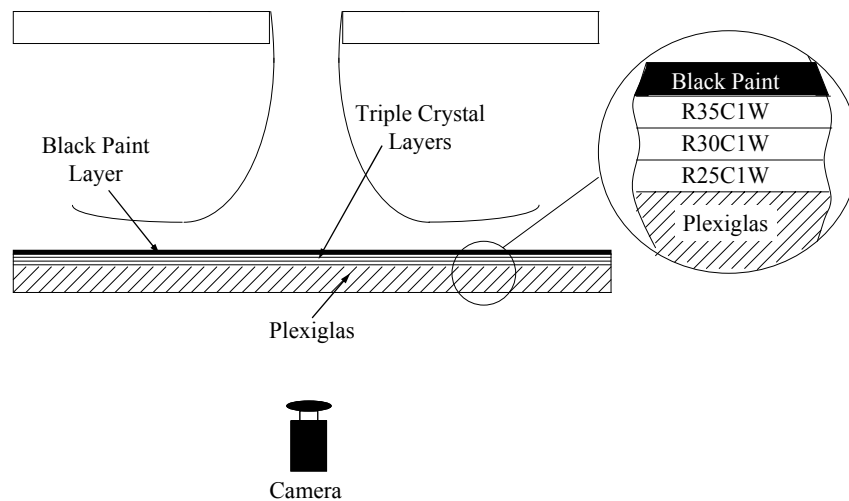


Figure 30 – Liquid crystal layers on the target surface

In order to capture the images from the liquid crystal color play, an adequate camera system is required. Heat transfer experimentation has utilized several different types of camera systems including RGB [Wang et al. (1996), Lee et al. (1997), and Gao et al. (2003)], CCD [Van Treuren (1994), Van Treuren et al. (1996), and Gao and Sunden (2002)], 3CCD [Kanokjaruvijit and Martinez-Botas (2003)], and infrared [(Hollworth and

Bowley (1975)]. For the present study, a three-chip CCD camera system was selected. The 3CCD camera produces the greatest color resolution of the systems available. Compared to a the single-chip CCD camera, the 3CCD system provides three times the color resolution as there are three different chips, each capable of storing one component of color. Since the entire chip is dedicated to one facet of color; either red, green, or blue; a greater resolution of the color intensity can be captured. Similarly, RGB cameras (or the common consumer camera) are incapable of matching the color resolution of the 3CCD. However, they have often been used in heat transfer experimentation because they are significantly less expensive, and can still provide a good heat transfer image, but its limitations are confined to smaller impingement arrays and geometries than the current design [see Wang et al. (1996), Lee et al. (1997), and Gao et al. (2003)]. Infrared camera systems, by design, offer the greatest potential contribution to heat transfer studies as they provide a thermal image that can give a direct temperature reading without the thermochromatic liquid crystals and image analysis required from the other three systems. However, this convenience comes at a very significant cost increase, and it is therefore not used for the current test.

The primary goal in the selection of the camera system was to establish a state-of-the-art image acquisition system. Therefore, the 3CCD camera chosen was a Sony DXC-C33. The camera is IEEE-1394 (FireWire) compliant allowing for faster transfer rates of 30 images per second. This is a significant improvement over the previous Baylor University image acquisition system which acquired an image every six seconds. Clearly, this means that more images will be taken per transient test, which provides greater detail into the jet activity and interaction that will allow for a more detailed view of the

formation of each individual aspect of the impinging jet's contribution to heat transfer. This can possibly lead to image acquisition of developing features too quick for the previous system and the naked eye that will provide greater depth into the characteristic nature of jet impingement. The Sony camera system is also digital, which provides greater resolution over the previous analog signal which required simultaneous capture and digitization during data acquisition. This aids in the image acquisition speed by simplifying the image acquisition process. A Fujinon VCL-616WEA C-mount camera lens was also added to the camera to provide the capability of expanding to view the entire impingement array without distortion, as well as zoom in on a single jet to provide excellent resolution and detail.

The image acquisition is run via a LabVIEW program which successively captures the images from the camera and stores them in the computer memory for post-processing. This program is shown in Appendix E. Simultaneous data is also collected by a Fluke Hydralogger data acquisition system. The system allows for the concurrent logging of the orifice pressure, upstream temperature, plenum temperature (four locations), jet temperature, surface temperatures (four locations), and room temperature. Overall, the system provides for the capability of measuring 20 input devices.

A different data acquisition system was also investigated, the National Instruments SCXI-1600 USB data acquisition system. The system allows for the same measurements as the previous system, but at a much faster rate with more channels. The system provides for the capability of measuring 32 thermocouple inputs and 8 input/output devices. The SCXI-1102 Thermocouple Input Module provides 32 thermocouple input channels that each include an instrumentation amplifier and a 2 Hz lowpass filter designed for high-



accuracy temperature measurement that provides cold junction compensation to an accuracy of  $0.1^{\circ}\text{C}$ . The data acquisition device itself connects to the computer by a USB connection which was selected to allow for the greatest mobility and modularity so that the system could be transported for use with other laboratory experimental data collection as well as the current facility. The system also provides the means for an all-in-one trigger start, whereby the push of a single button, the entire experiment can be started and data acquired through an easy LabVIEW interface. This however, was not implemented into the present design, but the system was investigated and chosen with its future implementation in mind.

## CHAPTER FIVE

### Experimental Investigation

This chapter explains the instrumentation employed as well as the experimental procedures and the techniques used in the validation of the impinging jet test facility. The calibration methods and data reduction techniques for the liquid crystal thermography are also discussed.

#### *Instrumentation*

In order to validate the experimental facility, the apparatus must be instrumented. The mass flowrate input into the system by the fan was measured using a Mamac PR-274-R4 Pressure Transducer. The transducer was connected to the orifice via 0.25 inch (0.635 cm) flexible plastic tubing, and the transducer was connected to the data acquisition system by a pair of wire leads. The transducer jumper was set to read a range of 0-15 inH<sub>2</sub>O pressure differential across a voltage range of 0-10 volts, but the jumper could be reconfigured to read a variety of smaller pressure differential ranges across the same full scale voltage range or a smaller voltage range depending upon the data acquisition device's capabilities (see Mamac PR-274-R4 User's Manual for other jumper configurations). The present range however, allows for the full capable fan flowrate to be measured.

The target plate is instrumented with four surface thermocouples as described previously and shown in Figure 29. The thermocouples are Omega "Cement On" Thin Foil Type K Thermocouples (Catalog #CO2-K). These thermocouples are constructed of a very thin foil (thickness = 0.005 in (0.0127 cm)) that was easily run along the surface of

the plate to a female thermocouple connector adhered to the edge of the target plate. A 10 ft (3.05 m) K-type thermocouple wire extender then connected each of the surface thermocouples to the data acquisition device. Similarly, six other thermocouples were inserted into the facility: five in the heated settling chamber section, and one in the pipe downstream of the orifice. Each of these thermocouples was made of the same K-type thermocouple wire as the extenders, and the tip was soldered together using an Omega Thermocouple and Fine Wire Welder (Model TL-WELD). The wire was then inserted into a 0.125 inch (0.3175 cm) outer diameter brass rod, with the tip extruding from the opposite end, which provided the wire with rigidity. Four of the thermocouples were placed  $8d$  inward in both the streamwise and spanwise directions from all four corners of the settling chamber, halfway between the heater mesh and the impingement plate. This allowed for thermal monitoring of the approaching air temperature. The fifth thermocouple placed in the settling chamber was positioned directly in front of the hole  $12d$  from the top of the test plate and  $4d$  inward from the left-hand side in order to provide a measure of the air temperature just prior to entering the test section. The final thermocouple was inserted into the downstream pipe, five pipe diameters from the orifice plate. All of these thermocouples were provided with a ten foot length and were directly connected to the female connectors of the data acquisition device.

### *Experimental Procedure*

This is the procedure for the current study, which does not utilize the data acquisition device and the camera system specified in the previous chapter. However, the procedure for using those devices is presented in Appendix F. The current process, which instead uses a stop watch and the visual identification of the color intensity peaks, also

uses a Fluke Hydralogger to acquire the instrumented data. The experimental procedure is as follows:

1. Ensure that the test plate is properly secured to the spacers and impingement plate via the attachment clips. In the event that any part of the test section has been replaced (i.e. impingement plate, spacers, or target plate), ensure that all joints are sealed with silicone to prevent leakage in the test section.
2. Measure and mark the center of each impingement hole desired to be tested on the target plate (since the black backing was applied to better view the crystal, the jet hole can no longer be seen through the Plexiglas). A measure of 3.44 in (8.73 cm) downward and inward from the top right corner of the impingement plate was used as the experimental jet. This will allow for better accuracy in determining the heat transfer coefficient at the stagnation point.
3. Check the pressure transducer connections and ensure that the tubing is connected to the proper “high” or “low” side of the orifice and transducer. Ensure that the jumper is properly placed within the Mamac PR-274-R4 Pressure Transducer according to its User’s Manual so that a 0 to 15 inH<sub>2</sub>O pressure differential can be measured. This pressure differential range will be adequate for the entire span of the fan’s capabilities. (For more precise measurements, the jumper placement can be modified per its User’s Manual)
4. Turn on the Fluke Hydralogger and computer. Load file *<httest1.ini>*. This will load the configuration of the thermocouples and pressure transducer. This file configuration sets up the 11 thermocouple inputs as channels 1-11 and the pressure transducer input as channel 12. This can be verified by selecting *<Show Setup>*.

Check the thermocouple connections to ensure that they are secure and are input into the proper channels. Ensure that the pressure transducer is wired into the proper channel.

5. Initiate the program so that temperature measurements can be made. Make certain that there are no open circuits by viewing the output and making sure that every thermocouple has a temperature output and does not read *TOC*, or thermocouple open circuit.
6. Inspect the fan to be sure that there is no loose debris in or around the inlet area. Remove all paper and other lightweight objects nearby that could easily be sucked into the inlet of the fan.
7. Turn on the blower fan by (1) pulling out the red knob on the back of the fan near the fan control panel, and then (2) pressing the green button (see Figure 31).

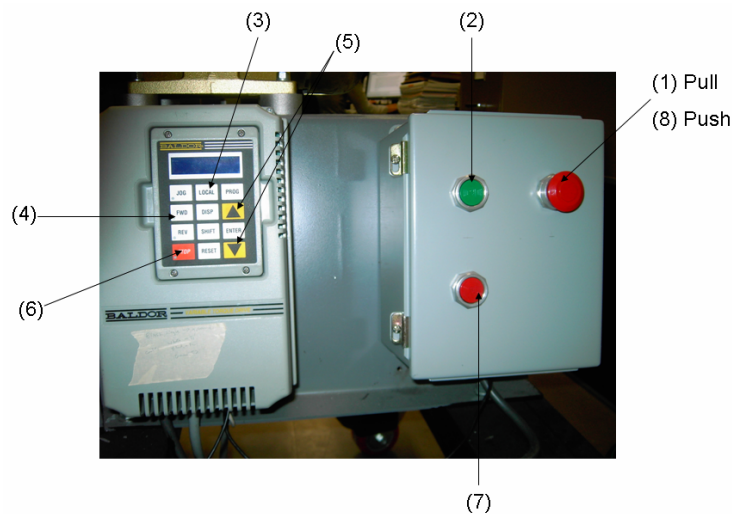


Figure 31 – Fan control panel

Allow the control panel approximately ten to fifteen seconds to initiate itself and warm up (a “click” will be heard when it is ready). (3) Press the *LOCAL* button,

followed by (4) the *FWD* button. This will start the fan. (5) Adjust the fan to the desired flowrate by increasing/decreasing the flowrate in whole number increments from 20Hz to 60Hz using the ▲ or ▼ keys. A pre-calibrated flowrate curve has been created to match the fan setting with its corresponding mass flowrate. This data curve is presented in Appendix G.

8. Allow the system to run until the thermocouples all reach a uniform reading.
9. Set the dial on the arc welder to the desired current output based on the calculation of Equation (22). After the temperatures have steadied in the test section, the experiment is ready to begin.
10. The method of data collection for the present study involves two people, one to operate the arc welder, and other to run the three stopwatches. The timer must position himself to get a good view of the jet hole he wishes to examine by using the marked hole as a guide. On his count, the welder switch is turned on and the timers started simultaneously. When the yellow-green color of the first crystal reaches the grid point, timer one is stopped, but timers two and three continue to run. When the second crystal reaches the yellow-green color over the grid point, the second timer is stopped as well. Similarly, when the third crystal reaches yellow-green, the third timer is stopped. Record the three times.
11. The experiment is now finished. Turn off the arc welder but do **NOT** turn off the blower fan. It is extremely critical that the fan is left on to continue cooling the heater mesh to prevent it from burning up. Once the test plate returns to its original black color (i.e. crystal color play has ceased and the temperatures shown

on the Hydrallogger are at approximately room temperature), the Hydrallogger data acquisition may be ceased by clicking <QUIT>.

12. The fan may then be turned off by first (7) pressing the red button, and then by (8) depressing the red knob (see Figure 31).

With the known time values and the corresponding temperature values obtained from a calibration using the surface thermocouples (calibration described in the following section), the double crystal technique creates two forms of Equation (11) that can now be solved for the local heat transfer coefficient and adiabatic wall temperature.

#### *Liquid Crystal Calibration Method*

The current experiment uses a method used by Li et al. (1988) and Jones (1992) which does not use a camera system with an image processor. Li et al. (1988) determined that visual perception of the yellow-green isotherm was sufficient for determining the heat transfer coefficient for a location on the target surface. For experimentation, three Hallcrest narrowband liquid crystals, R25C1W, R30C1W, and R35C1W, were used to cover the desired experimental temperatures. The intensity method involved calibrating all three liquid crystals for the peak intensity temperatures. With the prepared test plate in place, the calibration was performed under the controlled lighting conditions of the heat transfer experiment produced by the fluorescent lamps. A surface mounted thermocouple, located beneath an impinging jet, was used for calibration. The surface was slowly heated by incrementally increasing the supplied amperage from the arc welder. When the thin yellow-green band appeared to be directly on top of the thermocouple tip, the temperature was recorded by a handheld Fluke 52 K/J Thermometer directly connected to the surface thermocouple leads. This was performed until each of the three crystals had reached the

yellow-green peak intensity state over the thermocouple tip. The initial calibrations for the narrowband crystals were 26.6°C, 32.5°C, and 37.8°C.

The procedure for calibrating the liquid crystal color intensity using the three-chip CCD camera and NCXI data acquisition systems is also presented in Appendix H.

### *Jet Hole Discharge Coefficient*

Flow uniformity through the jet holes was verified by examining the discharge coefficient of each impinging jet. The discharge coefficient is a ratio of the average flowrate of each jet to the flowrate obtained from the Bernoulli Equation. The average flowrate was obtained by measuring the total mass flowrate through the orifice and then dividing it evenly between the 64 holes to obtain an average jet flowrate per hole. The flowrate at each jet hole was then calculated from pressure measurements made at the centerline of each jet hole. This flowrate,  $Q_{ideal}$ , can be described by:

$$Q_{ideal} = A_j \sqrt{\frac{2 \Delta p}{\rho}} \quad (23)$$

where  $A_j$  is the jet cross-sectional area and  $\Delta p$  is the pressure differential measured at the jet hole centerline. A pitot-static tube was used to measure the pressure differential exiting each jet hole. A Mamac PR-274-R4 Pressure Transducer was used to convert the pressure to a voltage signal which was read by a Phillips PM2525 Digital Multimeter. The jumper was set for a range of 0-15 inH<sub>2</sub>O across a full scale output of 0-10 volts. With the target plate removed from the facility, five pressure measurements were taken at each jet hole centerline, and the results were averaged for use with Equation (23).

Non-ideal effects can occur for two reasons. The first is that the flow through the jet hole actually forms a vena contracta as seen in Figure 32(b).



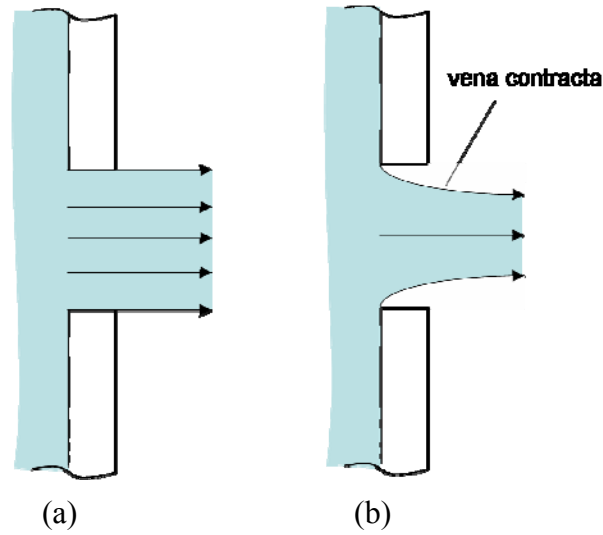


Figure 32 – Fluid ejection through a jet hole (a) ideal, (b) actual

In this case, it is clear that the diameter, and therefore, the resulting cross-sectional area of the vena contracta,  $A_v$ , is less than the area of the jet hole,  $A_j$  by some unknown amount.

Therefore,

$$A_v = C_D A_j \quad (24)$$

where  $C_D$  is the contraction coefficient, or the coefficient of discharge. The second reason for non-ideal effects is created by the swirling flow and turbulent motion of the fluid near the orifice plate, which introduces a head loss that must be empirically derived [Munson et al. (2002)]. Therefore, the discharge coefficient accounts for these effects by:

$$Q = C_D Q_{ideal} = C_D A_j \sqrt{\frac{2 \Delta p}{\rho}} \quad (25)$$

The average discharge coefficients measured for the current study were distributed as follows for a Reynolds number of approximately 20,000:

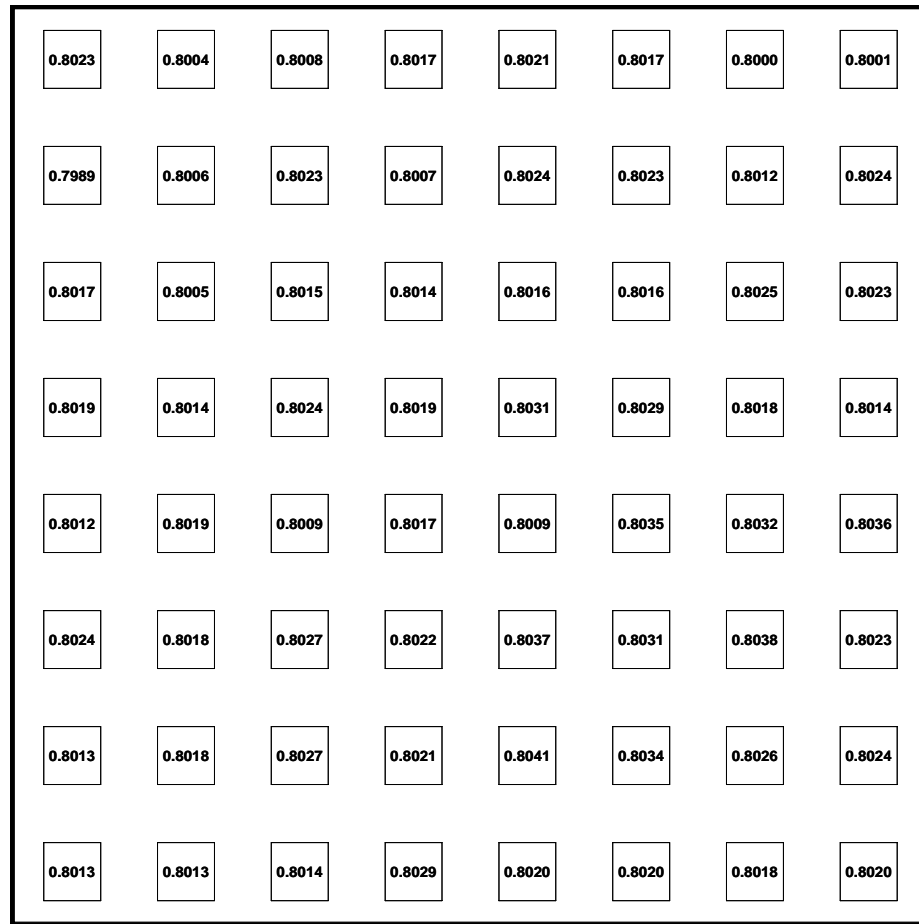


Figure 33 – Discharge coefficient distribution across the impingement plate

The average jet discharge coefficient was found to be 0.802 with a maximum percent difference of 0.375%. This is very similar to the 0.80 value for  $C_D$  obtained by Florschuetz et al. (1981) for the same jet Reynolds number and an  $\ell/d = 1$ . The value also falls directly in line with the results obtained from McGrehan and Schotsch (1988) and Bailey and Bunker (2002) who also obtained discharge coefficients equal to 0.80. The experimental value also finds very close agreement (within 2.2% difference) with James (1961), Van Treuren (1994), and Hay et al. (1987). A comparison between these results and the current study is presented in Table 3.

Table 3 – A comparison of discharge coefficients

Author	Year	Discharge Coefficient	% Difference
Florschuetz et al.	1981	0.8	0.25%
James	1961	0.791	1.39%
Van Treuren	1994	0.82	2.20%
McGrehan and Schotsch	1988	0.8	0.25%
Hay et al.	1987	0.81-0.82	0.99%-2.20%
Current Study	2005	0.802	n/a

This validates the facility for jet flow uniformity, which allows for further comparison of the test rig and the resulting heat transfer coefficients.

#### *Local Heat Transfer Coefficient*

The local heat transfer coefficient was examined at the stagnation point of the upper right hand corner jet. By the procedure described at the beginning of this chapter, test times of the crystal were measured and recorded. Five test times were obtained and averaged for the second and third crystal (R30C1W and R35C1W) for a range of average jet Reynolds numbers spanning 14,000 to 44,000. However, the heater mesh is unable to make a proper step change in time (<0.1 sec) and therefore, a time constant,  $\tau$ , must be accounted for [Gillespie (1993)]. Using the correlation equation developed by Gillespie (1993), the time constant is given by

$$\tau = 0.0840u^{-1.014} \quad (26)$$

where  $u$  is the mesh velocity. A calculator was then developed to iteratively calculate two simultaneous equations of the form Equation (12). This calculator is shown in Appendix I. The initial inputs are highlighted in yellow. With an initial guess of the beta ( $\beta$ ) value from Equation (12), the adiabatic wall temperature and local heat transfer coefficient can

be calculated. The resulting stagnation point  $Nu$  are shown in Figure 34. These values were compared with the correlation obtained by Van Treuren (1994), which was given by the following:

$$Nu = 0.567 Re_{jet}^{0.511} \quad (26)$$

where  $Re_{jet}$  is the local jet Reynolds number obtained by using the calculation program developed by Florschuetz et al. (1982) which predicts the crossflow distribution resulting in the local jet Reynolds number for each row of jets.

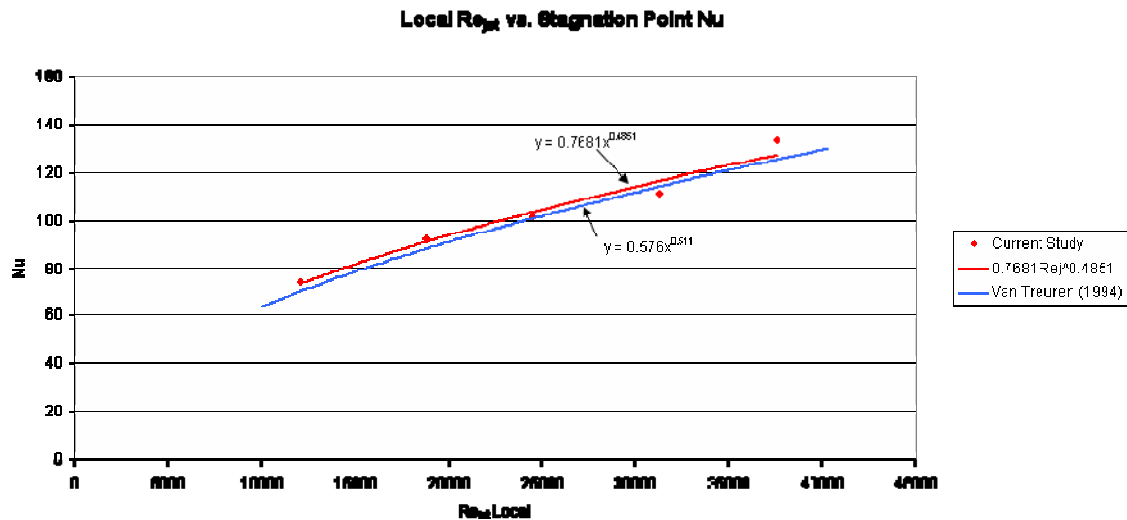


Figure 34 – Stagnation point Nusselt numbers at streamwise jet row one

Figure 34 plots the measured stagnation point  $Nu$  for a first row jet. From the data, a least squares fit was obtained to correlate  $Nu$  for a given local  $Re_j$ . This correlation is given by the following equation:

$$Nu = 0.7681 Re_j^{0.4851} \quad (27)$$

This equation is a general correlation for stagnation point  $Nu$  in the absence of crossflow for the conditions tested. This correlation gives a maximum percent difference of only 5%

for  $Re_j$  in a range of 10000 to 50000 when compared to the results obtained by Van Treuren (1994) in Equation (26). For all actual measured values, the largest percent difference with the predicted  $Nu$  correlated by Van Treuren (1994) was approximately 8% at the maximum blower fan setting of roughly  $Re_{j, local} = 37,500$  ( $Re_{j, avg} = 44,000$ ). This is within the criteria of 10% required for satisfactory facility validation outlined in Chapter One.

For the calculation of the local Nusselt number, the experimental uncertainty was determined by the method of Moffat (1988). The greatest experimental uncertainty was determined at local  $Re_j = 18,850$ . The calculated  $Nu$  for this condition was found to be  $84.813 \pm 5.943$  (20:1 odds). This yields an experimental uncertainty of 7.01%.

### *Flow Field Interpretation*

With the implementation of the camera and data acquisition system, a complete transient map of local heat transfer coefficient and adiabatic wall temperature can be obtained. However, for the current study, only the single stagnation point described in the previous section was used to validate the facility. The camera was however used to analyze the flow field and local heat transfer features beneath the inline array of impinging jets. The thermal map produced by the liquid crystal color play gives an indication of the relative heat transfer levels over the target surface. The color play initially appears in areas of highest heat transfer (which is typically, beneath the jet). Then, as the transient experiment progresses, the areas of lower heat transfer gradually exhibit the color play, as the areas of higher heat transfer begin to transition into the color play of the higher temperature crystal (i.e. from R25C1W to R30C1W or R30C1W to R35C1W). This process can be seen in Figure 35. As shown in the figures, the transition

lines for the narrowband liquid crystal form a sharp, thin color transition. The flow is from right to left (for all subsequent figures).

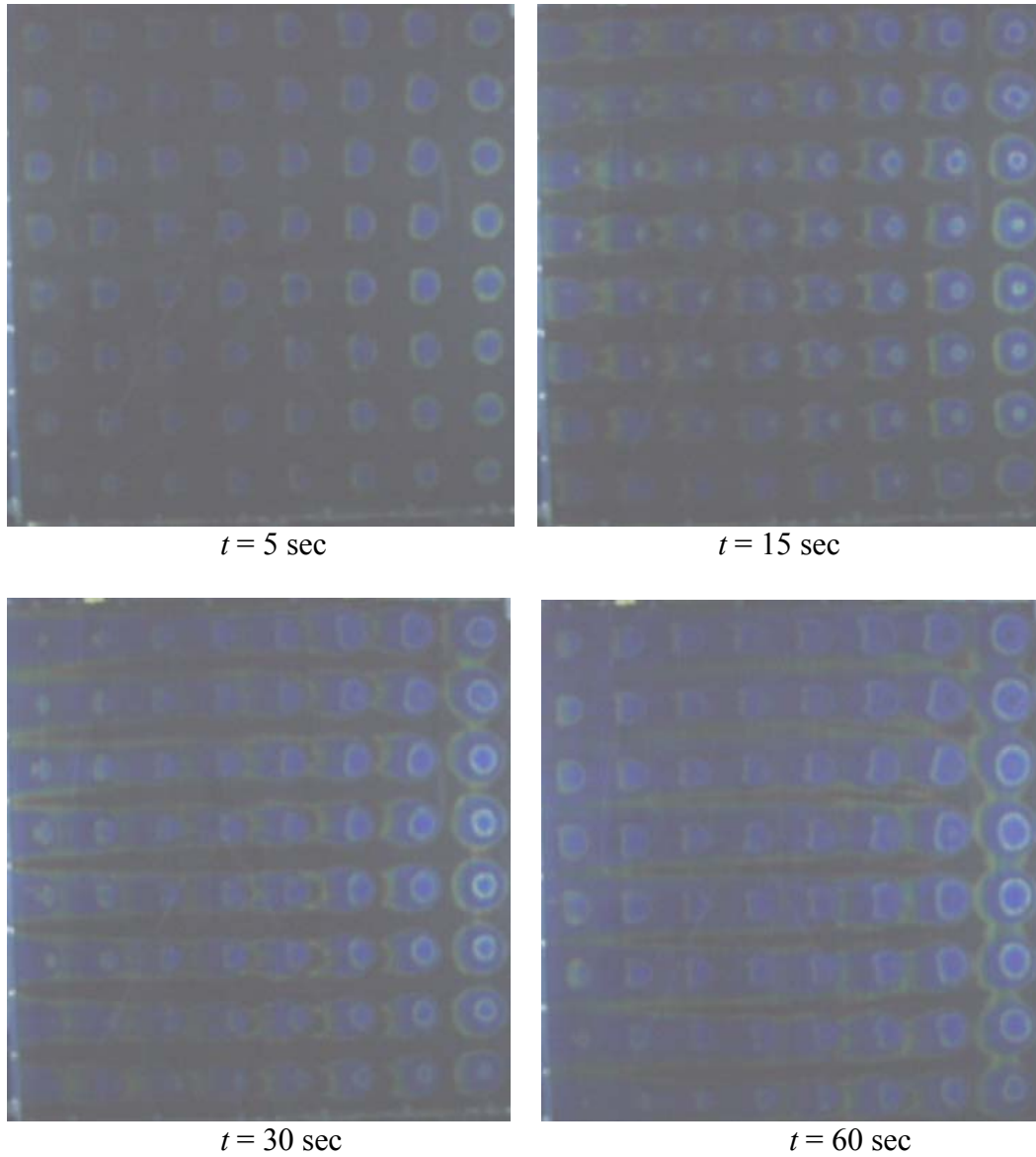


Figure 35 – Time sequence for average  $Re_j = 14,050$

The sequence of images are for average jet Reynolds numbers of 14,050 and a  $z/d = 1$ .

Figure 35 shows the formation of the jet interaction over time. It is important to note the circular nature of the thermal contour in the first row of jets (Figure 36). The contour is

circular because the influence of crossflow is minimal. The only crossflow present is that portion of the spent flow which moves toward the closed end before proceeding downstream between the first row jets. The first row is thus an indication of the effects of each jet without crossflow, and the spent air from the first row of jets then causes crossflow in the second row. The crossflow continues to accumulate for each subsequent row of jets until it exits from the test section.

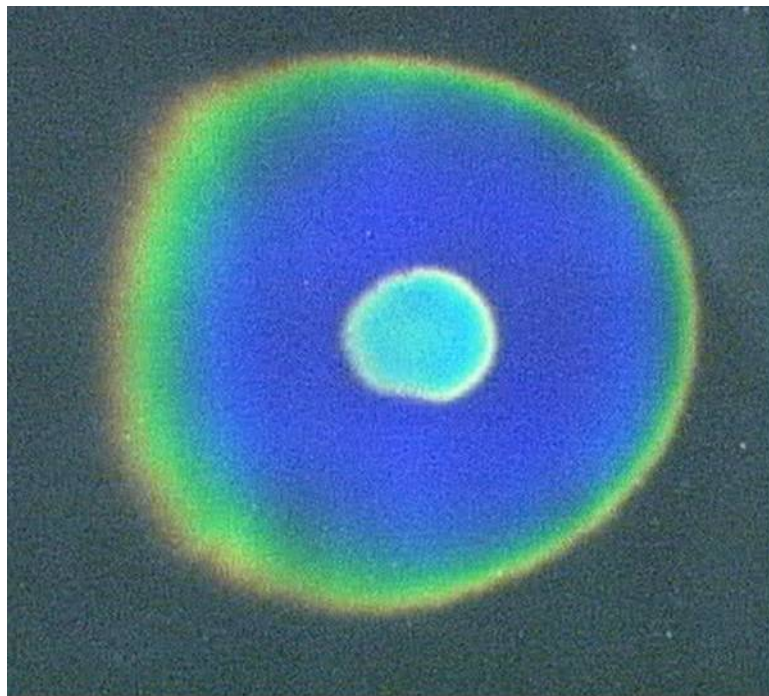


Figure 36 - Thermal contour of a first row jet

The most prominent feature of Figure 35 is the distortion of the jets downstream of the first row. This is attributed to crossflow. Crossflow affects the impinging jet in two ways. First, it attempts to displace the jet downstream of the jet exit; and secondly, it seemingly prevents the impinged jet from spreading in the upstream and spanwise directions. Both of these effects tend to elongate the circular footprint of the jet from that seen in the first row of jets. The spent flow that would typically spread radially outwards

in all directions to form circular contours, can now only spread in the downstream direction because of the upstream crossflow colliding with the jet core. This generates enhanced heat transfer at the back of the jet from the increased flow in that direction, hence, the elongated jet. With each subsequent jet row, the amount of crossflow increases, and its effects strengthened. This causes greater jet elongation with each downstream jet row. The effect of crossflow on an impinging jet is illustrated in Figure 37.

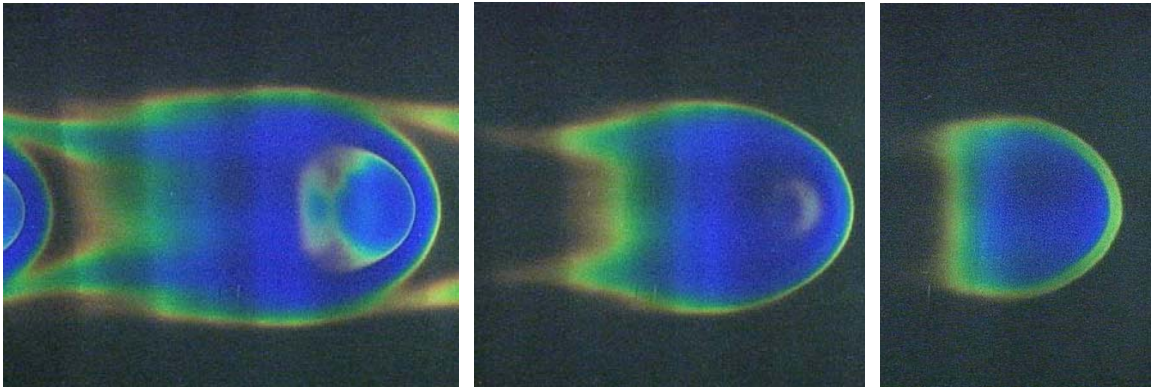


Figure 37 – Progressive elongation of impinging jets due to crossflow (flow from right to left)

An examination of the transient images reveals that the collision between the crossflow and the core flow also deflects the crossflow to the region between the jets. This indicates that the impinging jet acts as an obstruction to the crossflow. Since the jet is a circular contour, its effective footprint creates a reduced area available for crossflow at the midpoint directly in line with the adjacent jet center. Therefore, a local acceleration of the crossflow must occur between the jet centers, also known as the jet channel, which may attribute to the slight increase in heat transfer in this region (Figure 38).



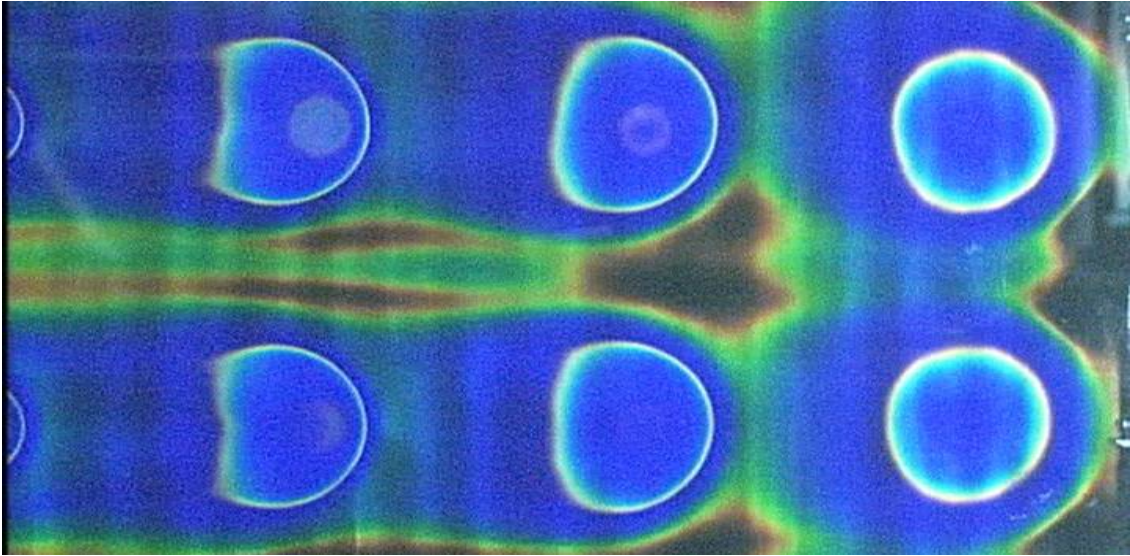


Figure 38 – Enhanced heat transfer effects in the jet channel region

Consequently, just downstream of this region, there is more area available for crossflow, and thus, the local deceleration in crossflow could account for this diminished crystal color play. With each successive downstream row, massflow is added to the crossflow, and thus, the highest channel velocity and channel heat transfer is achieved at the last row of jets. This explains the color play scheme of the impingement channel, which begins at the back of the array and progressively transitions upstream (Figure 39). However, the color play in the downstream jets is first impacted at the stagnation point beneath the jet, and not by the crossflow.

A very significant feature of the impinging jet flow field has also become evident because of the large scale of the impingement plate: the formation of a hairpin vortex in the downstream jet rows. A hairpin vortex is characteristic of turbulent flow, whereby counter-rotating streamwise vortices act as interacting hairpin legs, elongated by the mean

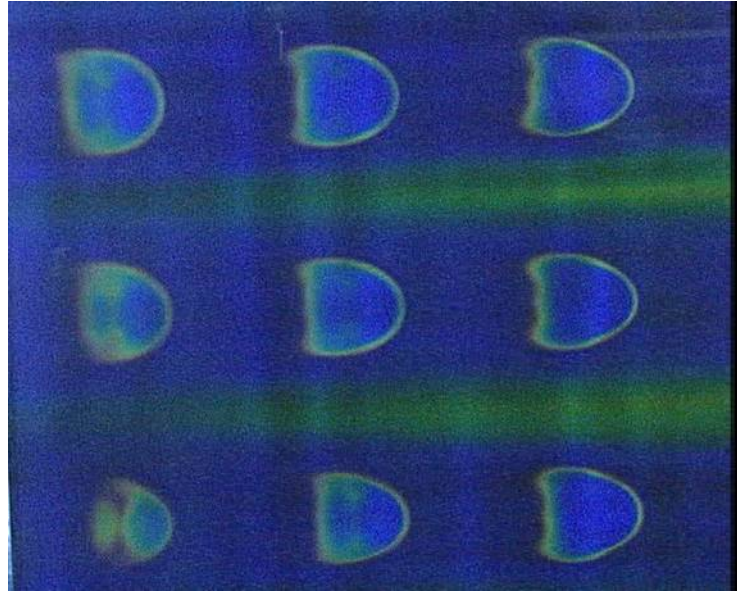


Figure 39 – Enhanced heat transfer in the jet channel at the back of the array

streamwise flow with hairpin heads embodied as traverse vortices inclined to the wall. This means that the legs of the hairpin vortex are comprised of rotational flow, which augments the heat transfer beneath it, before lifting and finally separating from the wall. This flow characteristic is generated by the turbulence of the crossflow exhibited in the region between the jets. Figure 40 shows the generation of the hairpin vortex beginning with the initial oscillation, and ending with the formation of the hairpin vortex.

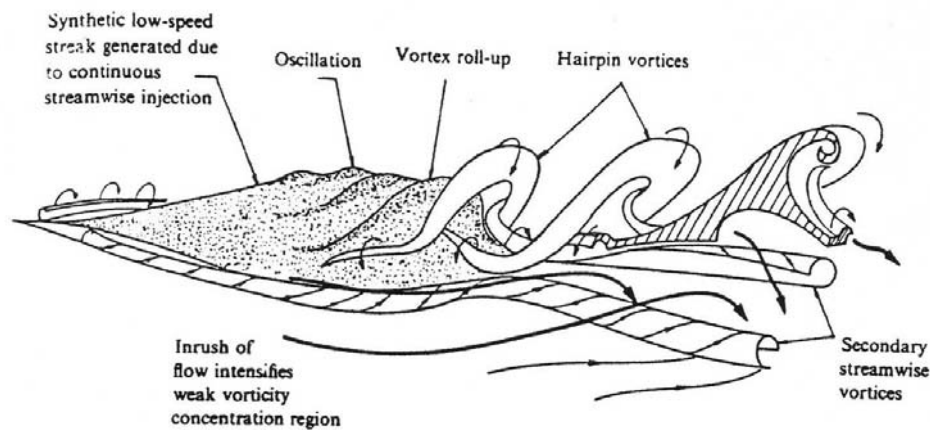


Figure 40 – Generation of a hairpin vortex [Acalar and Smith (1987)]

Figure 41, shows the thermal footprint of this flow characteristic. From the figure, the counter-rotational vortical legs of the hairpin vortex are clearly evident by the three heat transfer streaks running on either side of the core jet. Since the image is only capable of showing the effects of the hairpin on the target surface, the head of the hairpin vortex is not evident, as it is out of plane with the target plate.

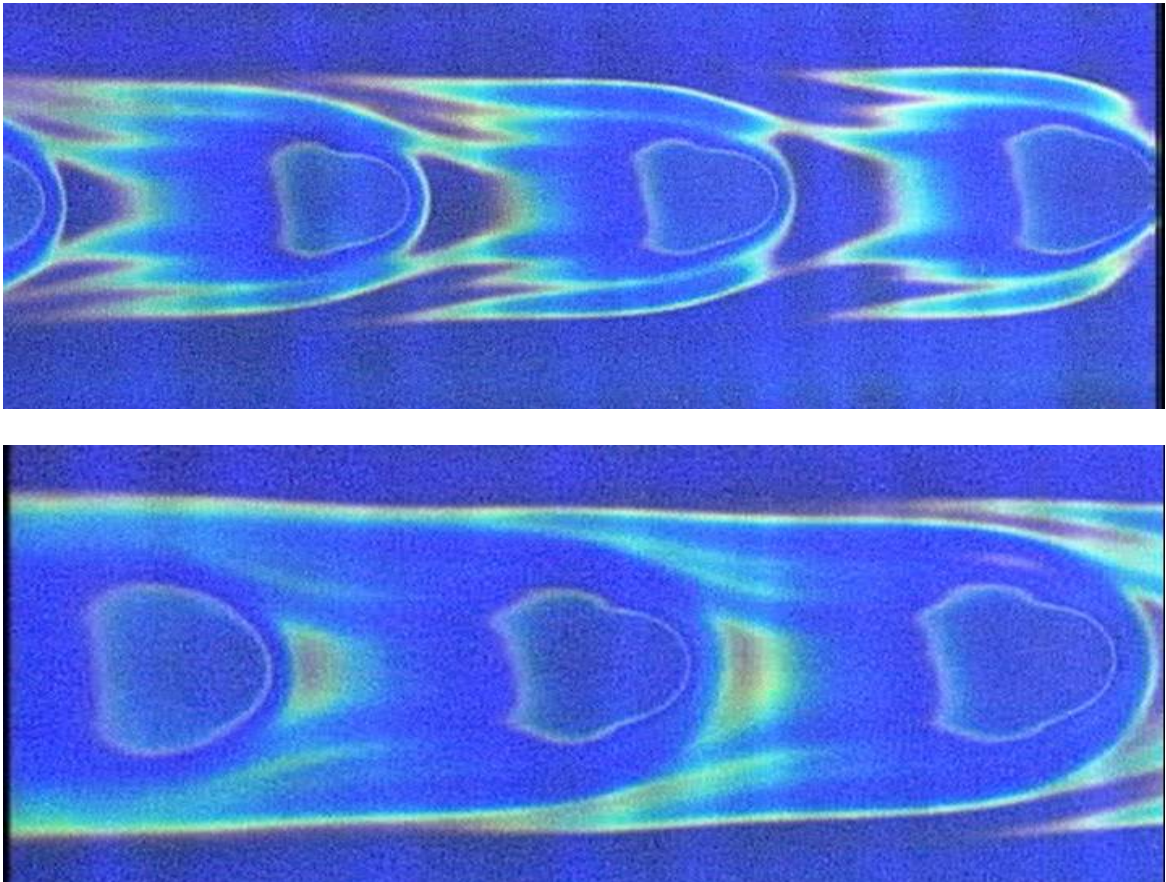


Figure 41 – Thermal footprint of a hairpin vortex  
(top):  $t = 0.35$  sec, (bottom):  $t = 0.50$  sec

For the current study, only the acknowledgement of the existence of the hairpin vortex is investigated. To the author's knowledge, no other experimental study has recorded such a find via thermal mapping, although its existence has been noted through



flow field studies involving smoke visualization and CFD techniques [Acalar and Smith (1987), Jeong et al. (1997), Patel and Roy (2003)]. Further studies should be conducted in order to quantify the contribution of the hairpin vortex to the overall heat transfer effectiveness.

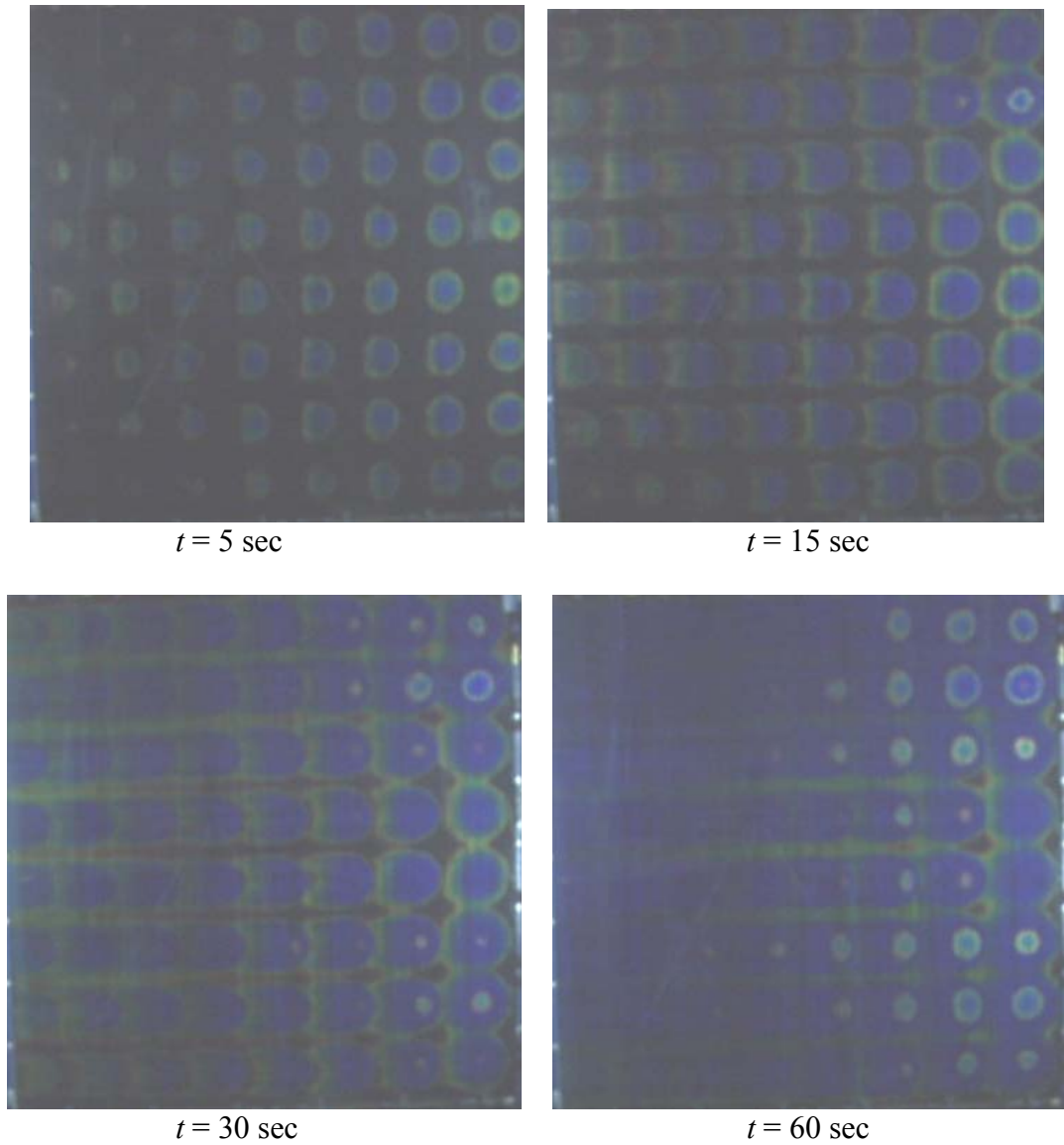


Figure 42 – Time sequence for average  $Re_j = 28,800$

With an increase in the jet Reynolds number, a clear increase in stagnation point and channel heat transfer levels becomes apparent. Figure 43 shows the impingement

array for an average jet  $Re$  of 28,800. From these images, a few key features become apparent. The first is that the area of highest heat transfer has been clearly defined as a small, circular ring just outside of the stagnation region. This contour is evident in the first rows of jets, and is illustrated by Figure 44. Several studies have determined this region to be approximately  $0.5d$  in the radial direction from the jet center [Gardon and Akfirat (1965), Obot et al. (1979), Van Treuren et al. (1996), and Lee et al. (1997)]. This increase in heat transfer has been attributed to jet interaction with the relatively quiescent channel air at the edges of the jet, as well as the local acceleration of flow caused by a minimum in boundary layer thickness of the wall jet as described in Chapter Two [Van Treuren (1994) and Lee et al. (1997)].

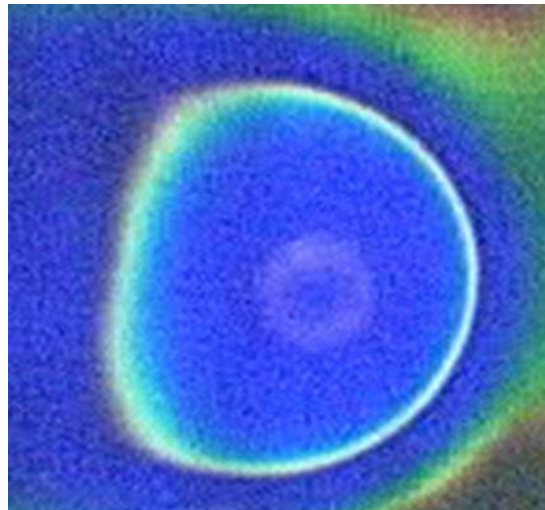


Figure 43 – Peak in heat transfer at  $0.5d$  from stagnation point

This peak in heat transfer is followed by an additional sudden increase in heat transfer away from the axial jet center. This region has been experimentally determined by Obot et al. (1979), Van Treuren (1994), and Lee et al. (1997), among others, to form at a radial distance of approximately  $1.5d$  to  $2d$  from the stagnation point. This feature is

again related to the boundary layer, and is shown in Figure 44. At this point, the boundary layer is thought to transition from laminar to turbulent, thus, the increase in heat transfer. With an increase in average jet Reynolds number to 43,300, the characteristic features of the surface heat transfer remains similar to that of the 28,800 case.

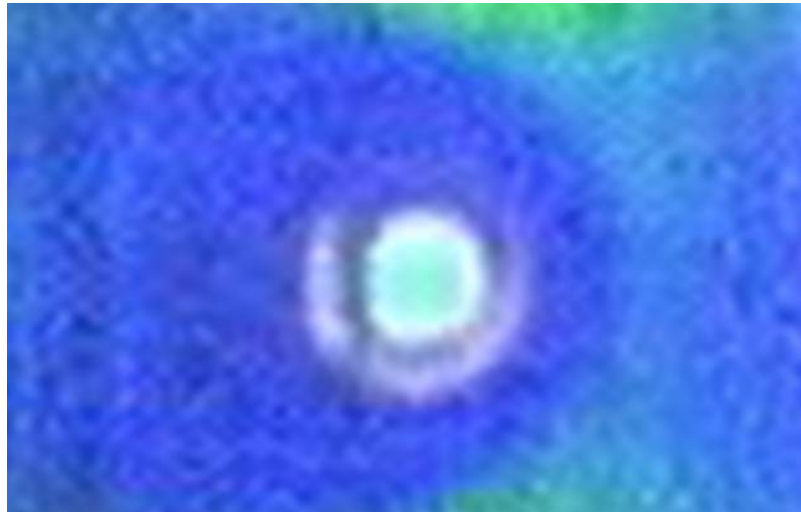


Figure 44 – Secondary peak in heat transfer at  $1.5d$  to  $2.0d$  from stagnation point

## CHAPTER SIX

### Conclusions and Recommendations

In this final chapter, a summary of the current work is presented with reference to the aims and objectives outlined in Chapter One, as well as the study's resulting contributions to the understanding of impinging jet arrays. The practical significance of the facility is then outlined and detailed. Finally, recommendations for facility improvement and future work are discussed.

#### *Summary of the Current Work*

A versatile experimental heated wind tunnel facility has been designed, developed, and validated for jet impingement heat transfer studies. Experiments were conducted for an inline jet array of uniform diameter jet holes in an 8 by 8 array configuration. The hole size was enlarged beyond the examined literature studies for a large range of engine representative Reynolds numbers. A calculation program was developed to determine the local heat transfer coefficient and driving gas temperature given inputs of measured surface temperature with time. For the configuration, the effect of the local jet Reynolds number has been quantified for the local stagnation point heat transfer. A subsequent correlation relating  $Re_{jet}$  and  $Nu$  was formulated.

Comparisons were made between the experimental stagnation point data and the published correlation presented by Van Treuren (1994). The experimental results were found to match the predicted results within the 10% criteria established in the Objectives section of Chapter One.

Comparisons were also made between the experimental jet discharge coefficient and published data from several sources. The measured discharge coefficient was found to correspond closely (within 2.2%) of all literature comparisons with similar experimental conditions. The facility was therefore validated for flow uniformity through the jet holes.

For the first time, a thermal footprint of a hairpin vortex has been identified. The identification of this structure will allow for the determination of the feature's contribution to the local and overall heat transfer. The current study however, did not quantify this contribution.

#### *Recommendations to Improve the Current Facility*

The current impinging jet facility provides an accurate model of engine representative impinging jets with values of local heat transfer closely matching with previous experimental correlations. However, several improvements to the facility could be made to upgrade its components. The honeycomb section initially provided flow leaks. The cause of the leaks was created by the material used in the section's construction. The leaks were caused when the Plexiglas frame buckled and broke when it was bolted to the frame, thereby creating gaps between the honeycomb panel and the frame. These gaps were accordingly sealed; however, the author recommends that the section could be better constructed by replacing the Plexiglas with a different material such as wood. The wood frame would provide the rigidity necessary to withstand the stresses created by bolting it to the frame. It is also recommended that a filler, such as an epoxy resin, should be used to fill the honeycomb cells at the screw attachment locations, so that the action of attaching the honeycomb between the top and bottom frames does not crush the



honeycomb (which can also create gaps). This is the same process used in the aerospace industry when attaching a fitting to the base of an aircraft fuselage.

The present heater mesh also produces a temperature gradient, with the upper right hand corner producing higher temperatures than the lower left, within the plenum. This has been determined to be associated with a bad connection between the mesh and the brass bus bars on the bottom side of the facility. By calculating the expected downstream temperature from Equation (22), and comparing the measured plenum temperatures from the data acquisition system, it can be seen that the upper right corner of the plenum is producing within the expected temperature values, while the other three corners fall short, with the bottom left producing the lowest values. Therefore, the right corner is sufficient for validating the facility's ability to produce accurate local heat transfer coefficients in this region; however, it is necessary to remove the mesh from the facility and resolder the mesh to the brass to produce a better connection, and thus, uniform heating for all regions.

The current facility also uses the Fluke Hydralogger data acquisition system, despite the capacity to use a much more advanced NI-SCXI system. The NCXI system was researched and purchased for the purpose of use with the current facility; however, it was not utilized for the validation of the current design. Implementation of this system would allow for faster data acquisition times as well as integration with the camera system. This would eliminate the stopwatch procedure described in Chapter Five. The system would also allow for the integration of a single trigger start, whereby with one click of the mouse, the welder would begin providing energy to the mesh, the data acquisition sequence would begin, and images would be successively captured via a coded LabVIEW program. This would allow for the use of the MATLAB program for analyzing

liquid crystal color intensity developed by Adavi (2003), as the associated time with each image would be known from the DAQ device.

### *Recommendations for Future Work*

The Baylor University impinging jet test facility was designed and developed with the idea of future experimental work as the foundation. The current work validated the facility for use in jet impingement heat transfer studies; however, the entire heat transfer array distribution was not investigated. Therefore, a complete surface analysis for differing  $Re_{jet}$  is recommended to quantify the current configuration heat transfer. It would then be logical to analyze different  $z/d$  dimensions, as well as varying jet hole spacing and geometries and compare them with the present configuration. This might provide a means for a combined geometry effect which could optimize a jet arrangement or cover a wider span of engine representative configurations. The facility might further be modified to eliminate the array altogether in favor of one very large single jet. The capabilities of the blower fan and the facility would allow for a single very large diameter hole to be investigated so that the features of the impinging jet would be enlarged on a very large scale to enhance the details of the thermal footprint.

The current facility was however, designed with special attention and consideration given to the current jet hole size. The hole diameter was designed to be large enough that a hot-wire flow field study could be performed on the current array of impinging jets. This would allow for an in-depth, detailed look at the jet flow by examining the local velocities at the jet exit. Also of interest would be to include a computational fluid dynamics study with the facility to predict the flow field and heat transfer and compare it with the experimental results.

The current experiment validates the design of the impinging jet testing facility, showing excellent correlation with heat transfer predictions from the literature. Since the current work only provides information for one jet region, other prediction correlations might be developed to compare the heat transfer and determine a local maximum location.

## APPENDICES

## APPENDIX A

## Screenshot of Losses Calculator

*loss\_calculator.xls***Loss Calculator****Temperatures**

Room Temperature	21.5 °C
Jet Temperature	30.0 °C

**Flowrate Specifications**

Input Flowrate	1340.34 ft <sup>3</sup> /min
----------------	------------------------------

0.63257 m<sup>3</sup>/s**Pipe Specifications**

Pipe Diameter	6.05 in
Length Upstream	60.5 in
Length Downstream	30.25 in

0.15367 m

1.5367 m

0.76835 m

**Orifice Specifications**

Orifice Outer Diameter	6.05 in
Orifice Inner Diameter	4.852 in
$\beta$	0.801983

0.15367 m

0.1232408 m

**Impingement Plate Specifications**

Hole Diameter	18.65313 mm
Holes Streamwise	8
Holes Spanwise	8
Hole Spacing (in d's)	8
$z/d$	1
Plate Thickness	18.65313 mm
Jet Reynolds Number	42257.14
Pipe Reynolds Number	343299.2

47/64 drill bit

0.734375 in

**Fan**

Depth	36 in
-------	-------

**Camera**

Distance from Target	84 in
----------------------	-------

**Regular Mesh**

Wire Diameter	0.011 in
Settling Chamber (min)	5.5 in

**Heater Mesh**

Wire Diameter	0.001575 in
Settling Chamber (min)	0.787402 in

**Overall**

Total Length	246.5374 in
	20.54478 ft

calculated delta: 11.37076738

measured 11.3709

%diff of flowrat 2.46%

**Plenum/Diffuser Specifications**

Plenum Width	1193.8 mm
Plenum Height	1193.8 mm
Plenum Area	1.425158 m <sup>2</sup>
Diffuser 90° Turn Radius	0.6096 m
Hydraulic Diameter	1.1938 m
Diffuser Length	0.6096 m

	Through Pipe	Through Orifice	Through Plenum	Through Holes
Velocity	34.10676489 m/s	53.02854 m/s	0.4438594 m/s	36.1689195 m/s

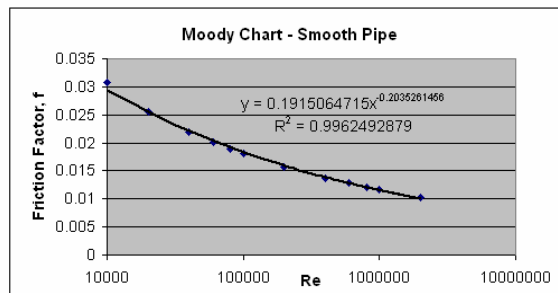
	Head Loss							
	Contraction	Upstream	Orifice	Downstream	Diffuser	Mesh Screens	Heater Mesh	Jet Holes
#	1	1	1	1	1	2	1	64
C <sub>o</sub>	-	-	0.83	-	-	-	-	-
K <sub>L</sub>	0.07	-	-	-	1.1496787	4.869244217	10.0608529	0.5
friction factor	-	0.014306	-	0.014306366	-	-	-	-
loss (m)	4.150305749	8.482256	121.9835	4.241127966	68.164544	0.097787521	0.101024493	33.33819412

<b>Total Loss</b>
240.559 m
11.3708 inH <sub>2</sub> O

**Interpolaters:**

## Friction Factor Interpolator

Re	f
10000	0.0308
20000	0.0256
40000	0.022
60000	0.0201
80000	0.0189
100000	0.0181
200000	0.0156
400000	0.0137
600000	0.0128
800000	0.0121
1000000	0.0116
2000000	0.0103



Air Properties Interpolation

	Temperatures of -40°C-25°C	Temperatures of 25°C-90°C	Temperatures of 90°C-1000°C
Density (room)	1.198 kg/m <sup>3</sup>	out of range kg/m <sup>3</sup>	out of range kg/m <sup>3</sup>
Viscosity (room)	1.83E-05 N·s/m <sup>2</sup>	out of range N·s/m <sup>2</sup>	out of range N·s/m <sup>2</sup>
Density (jet)	out of range kg/m <sup>3</sup>	1.165 kg/m <sup>3</sup>	out of range kg/m <sup>3</sup>
Viscosity (jet)	out of range N·s/m <sup>2</sup>	1.86E-05 N·s/m <sup>2</sup>	out of range N·s/m <sup>2</sup>
Density (mesh)	out of range kg/m <sup>4</sup>	1.113479 kg/m <sup>4</sup>	out of range kg/m <sup>4</sup>
Viscosity (mesh)	out of range N·s/m <sup>3</sup>	1.93E-05 N·s/m <sup>3</sup>	out of range N·s/m <sup>3</sup>

Water Properties Interpolator

	Temps of 0°C-60°C	Temps of 60°C-100°C
Density	997.825 kg/m <sup>3</sup>	out of range kg/m <sup>3</sup>

Properties of Water

Temp °C	Density kg/m <sup>3</sup>
0	999.9
5	1000.0
10	999.7
20	998.2
30	995.7
40	992.2
50	988.1
60	983.2
70	977.8
80	971.8
90	965.3
100	958.4

Properties of Air

Temp °C	Density kg/m <sup>3</sup>	Dynamic Viscosity N·s/m <sup>2</sup>
-40	1.514	1.57E-05
-20	1.395	1.63E-05
0	1.292	1.71E-05
5	1.269	1.73E-05
10	1.247	1.76E-05
15	1.225	1.80E-05
20	1.204	1.82E-05
25	1.184	1.85E-05
30	1.165	1.86E-05
40	1.127	1.87E-05
50	1.109	1.95E-05
60	1.060	1.97E-05
70	1.029	2.03E-05
80	0.9996	2.07E-05
90	0.9721	2.14E-05
100	0.9461	2.17E-05
200	0.7461	2.53E-05
300	0.6159	2.98E-05
400	0.5243	3.32E-05
500	0.4565	3.64E-05
1000	0.2772	5.04E-05

APPENDIX B

Oripac Orifice Meter Manufacturer’s Supplied Data Curve

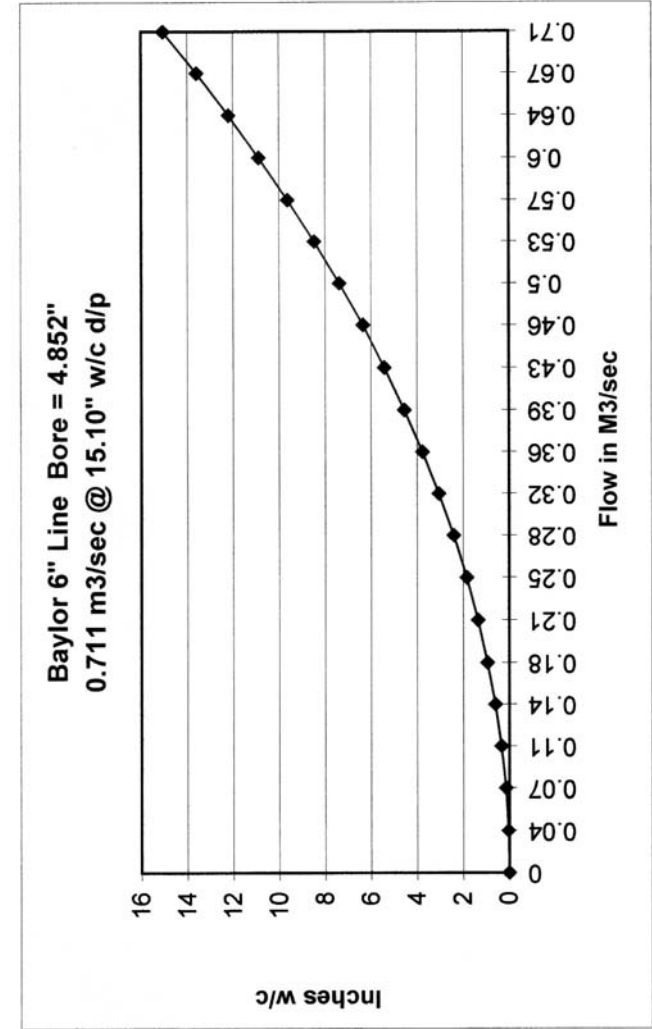
Lambda Square Inc.

Baylor Univ.

1  
15.1

Full Scale Flow  
Full Scale d/p

Size: 6" s/40 Pipe Fluid: Air Flow: 0.711 m3/sec Press: 14.7 psia Temp: 60 deg F



Flow	D/P
0	0
0.0355	0.037644
0.071	0.150576
0.1065	0.338795
0.142	0.602302
0.1775	0.941097
0.213	1.35518
0.2485	1.84455
0.284	2.409209
0.3195	3.049155
0.355	3.764389
0.3905	4.55491
0.426	5.42072
0.4615	6.361817
0.497	7.378202
0.5325	8.469874
0.568	9.636835
0.6035	10.87908
0.639	12.19662
0.6745	13.58944
0.71	15.05755

## APPENDIX C

### Mesh Production Instructions

#### *To Remove an Old Heater Mesh Screen*

1. Evenly heat the brass bus bar with a heating torch
2. After the bar has been partially heated, unscrew the locking screws in the bar
3. Continue heating the two bars which are now only held together by solder
4. When the two bars are able to be separated by hand, do so, being sure that a glove is used to handle the bar, as it will be extremely hot
5. Peel/scrape off the thin sheet of solder that remains on the brass bus bar
6. Use a steel wire brush to scrape the soldered surface of each brass bus bar until the solder has been evenly distributed and the metal feels smooth

#### *Cutting a New Mesh Screen*

1. Unroll the mesh screen in necessary and place on a flat surface.
2. Measure and trace out a square of 47 in x 55 in on a flat portion of the mesh, keeping in mind that folds and crinkles in the mesh will affect uniform heat transfer when heated.
  - a. The 55 in length will provide the 4 in extra length on either side to allow for clamping the mesh on one end and locking the other end in the mesh jig, to help make it taut. Therefore, this length can be adjusted as desired, as long as enough length is kept to provide ease in using the mesh jig.



- b. Be sure to leave room on either side of the 47 in length for one extra inch.

This material will be used to make tabs. (mesh width = 52 in)

3. Trace out 1 in wide by 1 in tall triangular tabs, every six inches, along the 47 in length as seen below. These will provide the tabs which become clamped between the two heater mesh frame halves. (The tabs must so be done because if a large area of mesh is clamped between the frame, the mesh will burn up upon heating)

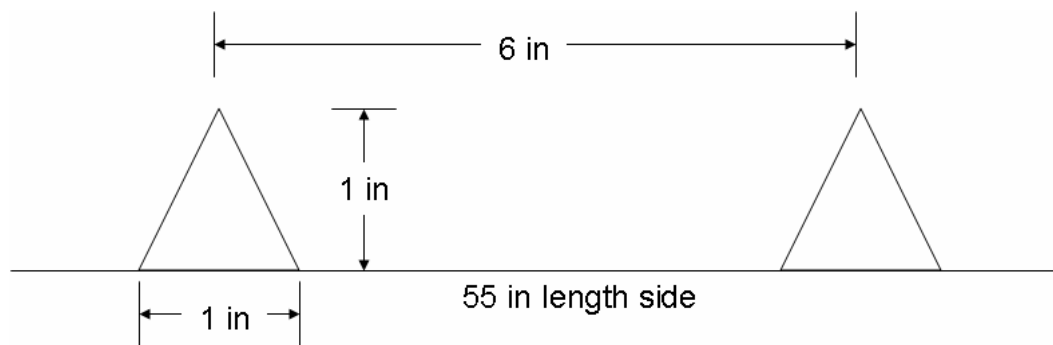


Figure C.1 – Mesh tab measurements

4. Cut the mesh to shape using a standard scissors

#### *Soldering to the Brass Bus Bars*

1. Lay the thin section of frame on the mesh jig with the flat side down. Lay a piece of brass flush against the ridge of the frame bottom, allowing one end to remain flush with the edge and the other to protrude past the frame edge. Do the same on the opposite side with the brass flush with the edge on the opposite side as it was with the other bar.



Brass flush with the edge

Brass protruding past the edge

Figure C.2 – Orienting the brass on the wood frame

2. Lay the mesh over the jig, placing careful attention to aligning the tabbed edge of the mesh with the edges of the frame. Lock one end of the mesh over the ratchet bar of the mesh jig, and clamp the other end to the flat aluminum surface of the mesh jig. Ratchet the mesh taut.
3. Poke holes in the mesh at the screw points in the brass bars on the CLAMPED SIDE (not the ratchet side). This will help the screw into the hole.
4. Cut a piece of silver solder to the length of the mesh. Flatten the solder by hammering it on a clean, solid surface. Try as carefully as possible to keep the solder in a straight line, as the flattening will tend to create a snake-like effect in the solder. This is acceptable as long as the solder stays relatively straight.
5. Place the flattened solder over the mesh and brass bar on the clamped side. Try to keep the solder away from the inner portion of the mesh if possible. Squirt some flux along with the solder in this same area.
6. Place the top brass bar over the solder, etc. and start the screw as much as possible. Note, it will not tighten all the way.

7. Prop up the opposite side of the mesh jig so that the lower end is the working end.

This is done so that when the brass is heated and the solder melts, it does not run into the inner portion of the mesh, but rather, away from it.

8. Place a large piece of aluminum across the length of the top piece of brass so that the mesh immediately touching the brass is covered by the aluminum plate. This will act as a heat sink and prevent the torch from directly coming into contact with the heater mesh to prevent it from burning up. Make sure that no portion of mesh is visible between the edge of the top piece of brass and the edge of the aluminum plate.
9. Use a low temperature torch to heat the top piece of brass, working the torch back and forth over a small section of the bar. As this portion heats, move the torch to the adjacent portion of the bar, and use a screwdriver to tighten the screws of the heated portion (Be careful of the torch!) After the screw has been tightened, be sure to continue heating the area, as another screw is tightened. Continue this process until every screw is satisfactorily tightened across the entire bar and the bars appear to be tightly joined. Note: it may be possible to see some solder squeeze out the bottom end *away* from the inner portion of the mesh. This can be used as a guide as to whether or not the solder has melted yet.
10. When the side has been completed, wait for it to cool before proceeding to the next side. A fan may be used to help convect heat away from the surface.
11. When the bars have cooled sufficiently enough that it would be impossible for the solder to run towards the inner portion of the mesh, it is time to begin soldering the

opposite side. Ratchet the mesh taught using a ratchet and socket attached to the end of the ratcheting rod.

12. Repeat steps 3 through 10.
13. After the mesh has cooled, begin on one side of the mesh and pull the tabs outward so that the mesh tightens. Place a small piece of electrical tape over a portion of the tip of the triangle and adhere it to the frame.
14. Move to the opposite side of the frame, and repeat step 13 with the tab directly across from it.
15. Repeat steps 13 and 14 for the tab next to this tab. Continue repeating this procedure until all of the tabs have been taped to the frame. This will create a taught mesh.
16. Overlay the top frame and screw the two pieces together so that the mesh can be transported to the facility and mounted using the designated screw holes. If the mesh is not to be mounted right away, place the mesh in a safe spot to prevent it from being damaged.

## APPENDIX D

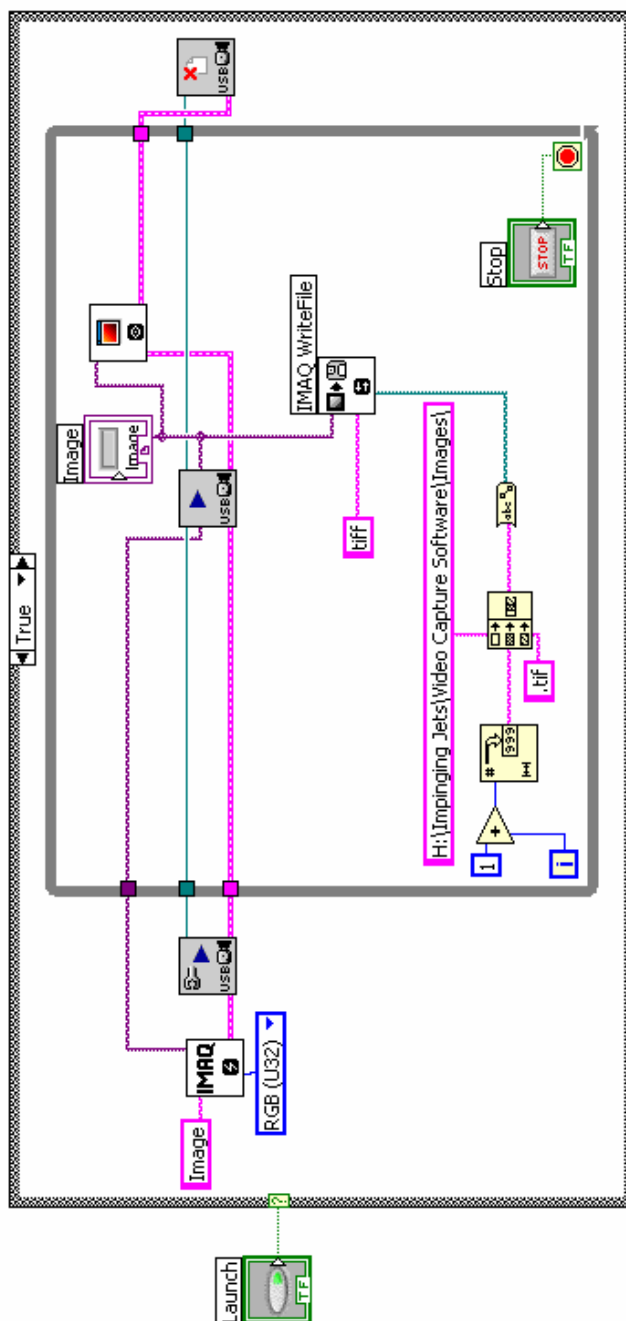
### Heater Mesh Resistance Measurement Technique

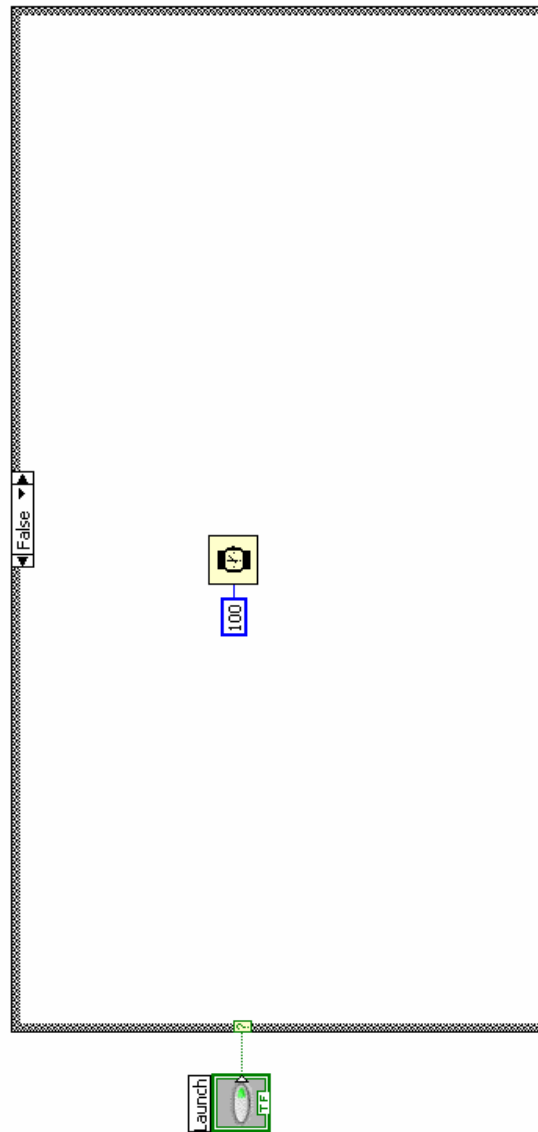
1. To measure the resistance in the heater mesh, simply connect the arc welder to the brass bus bars.
2. Follow the procedure described in Chapter Five to start the facility.
3. Wire a Phillips PM2525 Multimeter with alligator clips and connect them to the welder electrodes at the base of the welder. Turn on the welder.
4. Use the Multimeter to measure the output voltage. Perform this operation for a variety of welder amperage outputs. (Note: a test was performed to validate the amp output of the welder and it was found that the output matches the setting at approximately 125 A)
5. Using Ohm's Law ( $V=IR$ ), calculate the resistance in the mesh.

The resistance found in a 316-Stainless Steel mesh with 40  $\mu\text{m}$  diameter wire, soldered with Stay-Brite (Lead-free, Cadmium-free) Silver Solder, between 1660 Brass bars is 0.074  $\Omega$ .

## APPENDIX E

## LabVIEW Program for Image Acquisition

*firewire\_continuousgrab.vi*



The following programs MUST be installed on the computer IN THIS ORDER for the program to work:

1. LABVIEW 7.1 or greater
2. IMAQ Vision for LabVIEW 7.1
3. IMAQ 3.1.1 driver (available on the National Instruments Website)

NI\_IMAQ\_for\_USB\_Cameras (available on the National Instruments Website)

## APPENDIX F

### Experimental Procedure Using Camera and SCXI Acquisition Systems

1. Ensure that the test plate is properly secured to the spacers and impingement plate via the attachment clips. In the event that any part of the test section has been replaced (i.e. impingement plate, spacers, or target plate), ensure that all joints are sealed with silicone to prevent leakage in the test section.
2. Overlay a grid to pinpoint the center of each impingement hole on the target plate (since the black backing was applied to better view the crystal, the jet hole can no longer be seen through the Plexiglas). This will allow for better accuracy in determining the heat transfer coefficients in the region around the stagnation point.
3. Check the pressure transducer connections and ensure that the tubing is connected to the proper “high” or “low” side of the orifice and transducer. Ensure that the jumper is properly placed within the Mamac PR-274-R4 Pressure Transducer according to its User’s Manual so that a 0 to 15 inH<sub>2</sub>O pressure differential can be measured. This pressure differential range will be adequate for the entire span of the fan’s capabilities. (For more precise measurements, the jumper placement can be modified per its User’s Manual)
4. Turn on the computer, SCXI data acquisition device, and camera. Load file *<htexperiment.vi>*. This will load the configuration of the thermocouples, pressure transducer, and camera system. This file configuration sets up the 11 thermocouple inputs as thermocouple channels 0-10 and the pressure transducer input as channel 11. Check the thermocouple connections to ensure that they are



secure and are input into the proper channels. Ensure that the pressure transducer is wired into the proper channel. Ensure that the camera is plugged into the computer via an USB port.

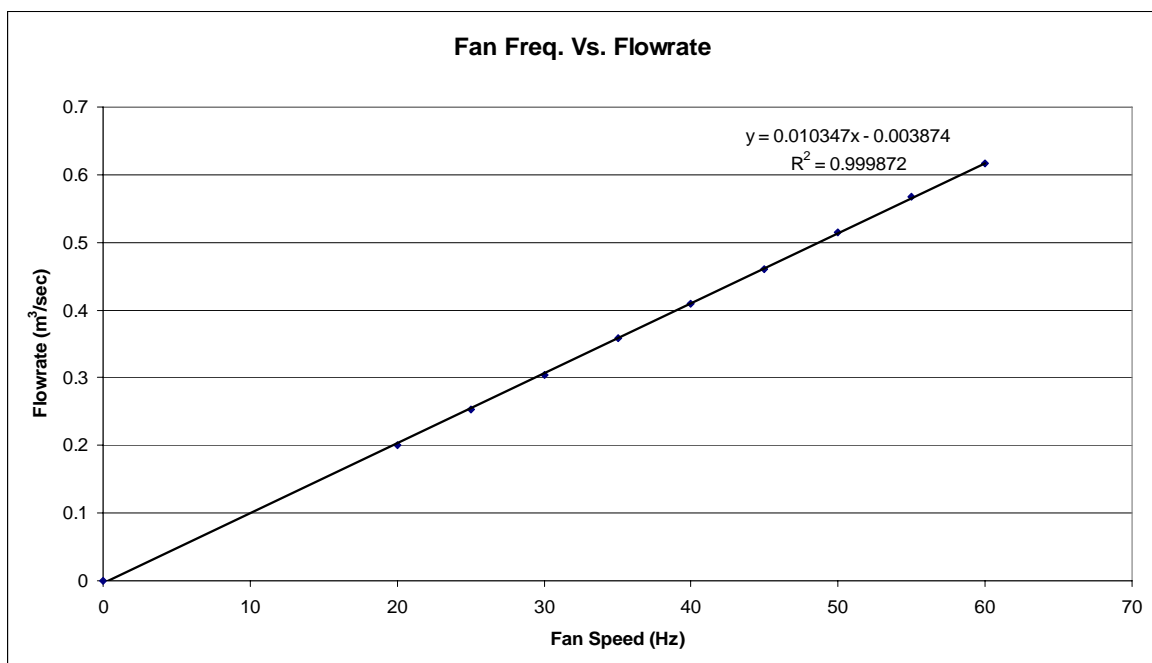
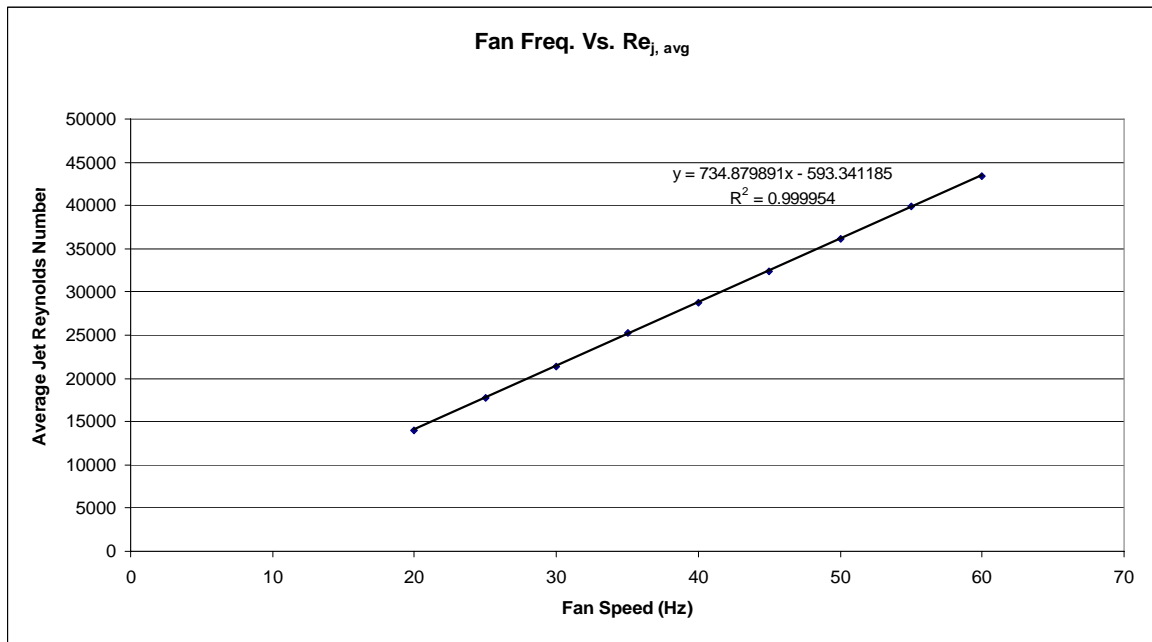
5. Calibrate and verify the thermocouples connected to the SCXI-1102 Thermocouple Module per the step-by-step calibration procedure for the device found in the supplied Users Manual.
6. Set up the camera and remove the lens cap. Ensure that the desired view is captured in the screen by using the real-time display monitor of Microsoft Movie Maker.
7. Inspect the fan to be sure that there is no loose debris in or around the inlet area. Remove all paper and other lightweight objects nearby that could easily be sucked into the inlet of the fan.
8. Turn on the blower fan by pulling out the red knob on the back of the fan near the fan control panel, and then pressing the green button (see Figure 31). Allow the control panel approximately ten to fifteen seconds to initiate itself and warm up. Press the *LOCAL* button, followed by the *FWD* button. This will start the fan. Adjust the fan to the desired flowrate by increasing/decreasing the flowrate in whole number increments from 20Hz to 60Hz using the ▲ or ▼ keys. A pre-calibrated flowrate curve has been created to match the fan setting with its corresponding mass flowrate. This data curve is presented in Appendix G.
9. Allow the system to run for five minutes to allow the thermocouples to steady at ambient temperature.

10. Set the dial on the arc welder to the desired current output based on the calculation of Equation (22). After the five minute waiting period, the temperatures should be steady in the test section. The experiment is now ready to begin.
11. The method of data collection for the present study involves two people. One to man the arc welder, and one to man initiate the data acquisition program. On a set count, simultaneously switch on the welder and trigger the data acquisition by the *START* button.
12. Let the experiment run for a set experiment time of two minutes. After two minutes, click the *STOP* button to cease data acquisition and save the output file. Turn off the arc welder, but do NOT turn off the blower fan. It is extremely critical that the fan is left on to continue cooling the heater mesh to prevent it from burning up. Once the test plate returns to its original black color (i.e. crystal color play has ceased).
13. The fan may then be turned off by first pressing the red button, and then by depressing the red knob.

The saved images may now be implemented into *CalculateTempArray.m* with these results going into *HeatTransferMain2.m* in MATLAB. Follow the directions within *UsageNotes.doc* to process the images for their intensity values [Adavi (2003)].

## APPENDIX G

## Cincinnati Blower Fan Flowrate Curve



## APPENDIX H

### Liquid Crystal Calibration Procedure for Camera and SCXI System

For experimentation, three Hallcrest narrowband liquid crystals, R25C1W, R30C1W, and R35C1W, were used to cover the desired experimental temperatures. The intensity method involved calibrating all three liquid crystals for the peak intensity temperatures. With the prepared test plate in place, the calibration was performed under the controlled lighting conditions of the heat transfer experiment produced by the fluorescent lamps. A surface mounted thermocouple, located beneath an impinging jet, was used for calibration. The surface was heated to the blue-violet color-play temperature of the first crystal (R25C1W), and then allowed to cool until the color disappeared. This procedure was performed for the R30C1W and R35C1W crystals as well. The crystals must be calibrated separately because heating to the point of the crystal turning clear (heating past blue-violet) will introduce a bias [Anderson and Baughn (2004)]. The data acquisition system was used to record the thermocouple temperature as well as capture successive images from the camera. The images were then processed to find the three intensity peaks corresponding to the three different crystals. This process will produce results similar to the below: When the images with the highest liquid crystal intensity were determined, their associated time values were used to look up the thermocouple temperature corresponding to the intensity peak.

## APPENDIX I

## Heat Transfer Coefficient Calculator

*ht\_calculator.xls*

SPREADSHEET TO CALCULATE HEAT TRANSFER COEFFICIENTS  
FOR PLATE AND JET USING THE DOUBLE CRYSTAL  
TECHNIQUE

569  $\sqrt{(\rho ck)}$ 

### Gillespie (1993) Correlation

Amesh	1.42515844	m2
rho	1.127	kg/m3
mdot	0.618200561	kg/s
umesh	0.384895053	m/s
tau	0.221178121	s

	TEST#1
TSUR1 =	32.5 deg C
TSUR2 =	37.8 deg C
TIME1 =	4.17 s
TIME2 =	18.13 s
K =	2.129608327
TINIT=	21.5 deg C
B1GUES=	0.588942096 0.5889421

k	0.02856 W/mK
---	--------------

LHS	0.633055507
RHS	0.633055507
DIFF	0

BETA1	0.588942096
BETA2	1.254215991

H#1	168.6363104 W/m2K
H#2	168.6363104 W/m2K

THETA1	0.427215373
THETA2	0.633055507

Taw1	47.24813713 deg C
Taw2	47.24813713 deg C

Calculated

Htotal	168.6363104 W/m2K
Nu	110.1397045

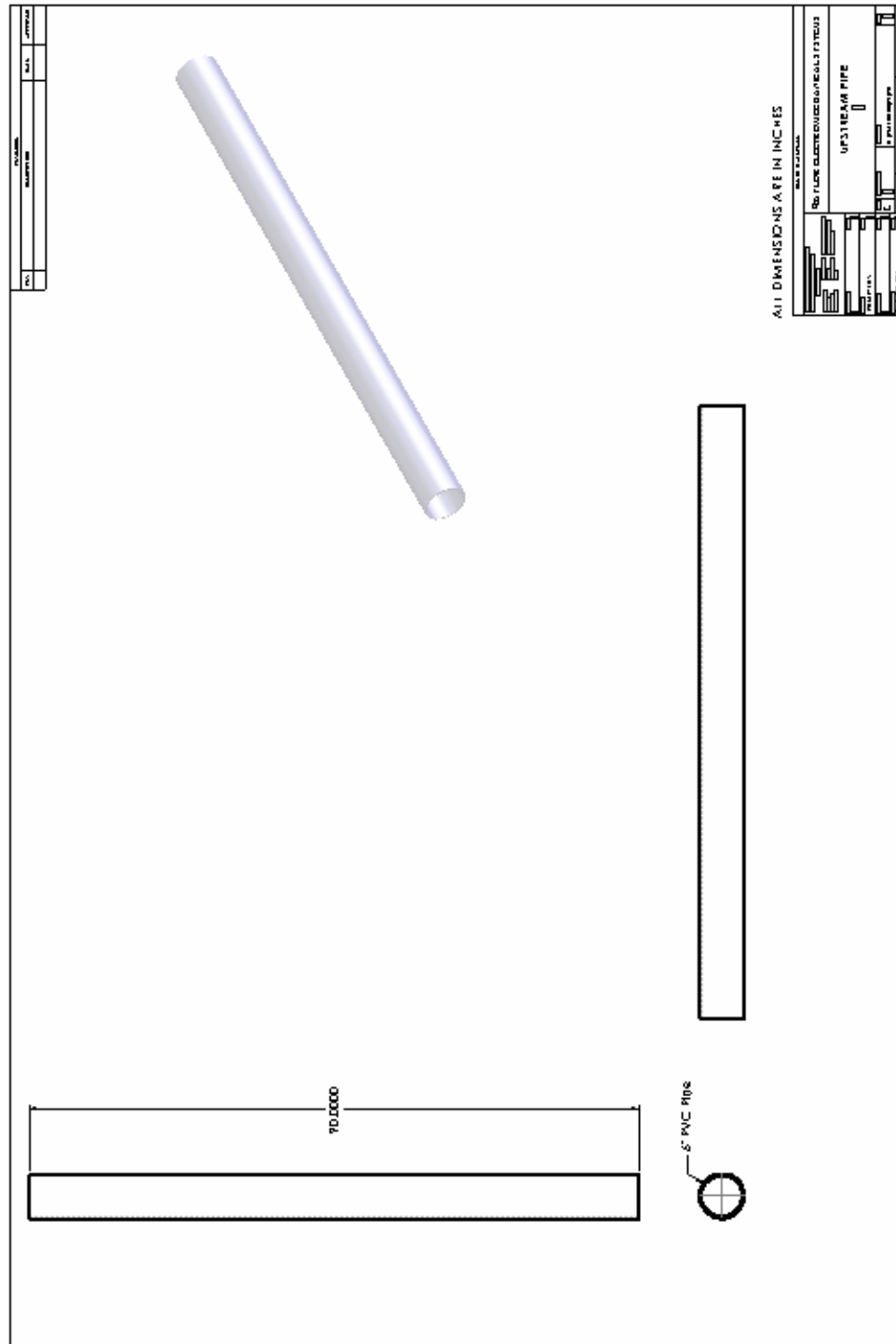
Predicted

Rejet 31249 from Florschuetz (1982) - C3630F.exe  
Nu 112.3167 from Van Treuren (1994) correlation

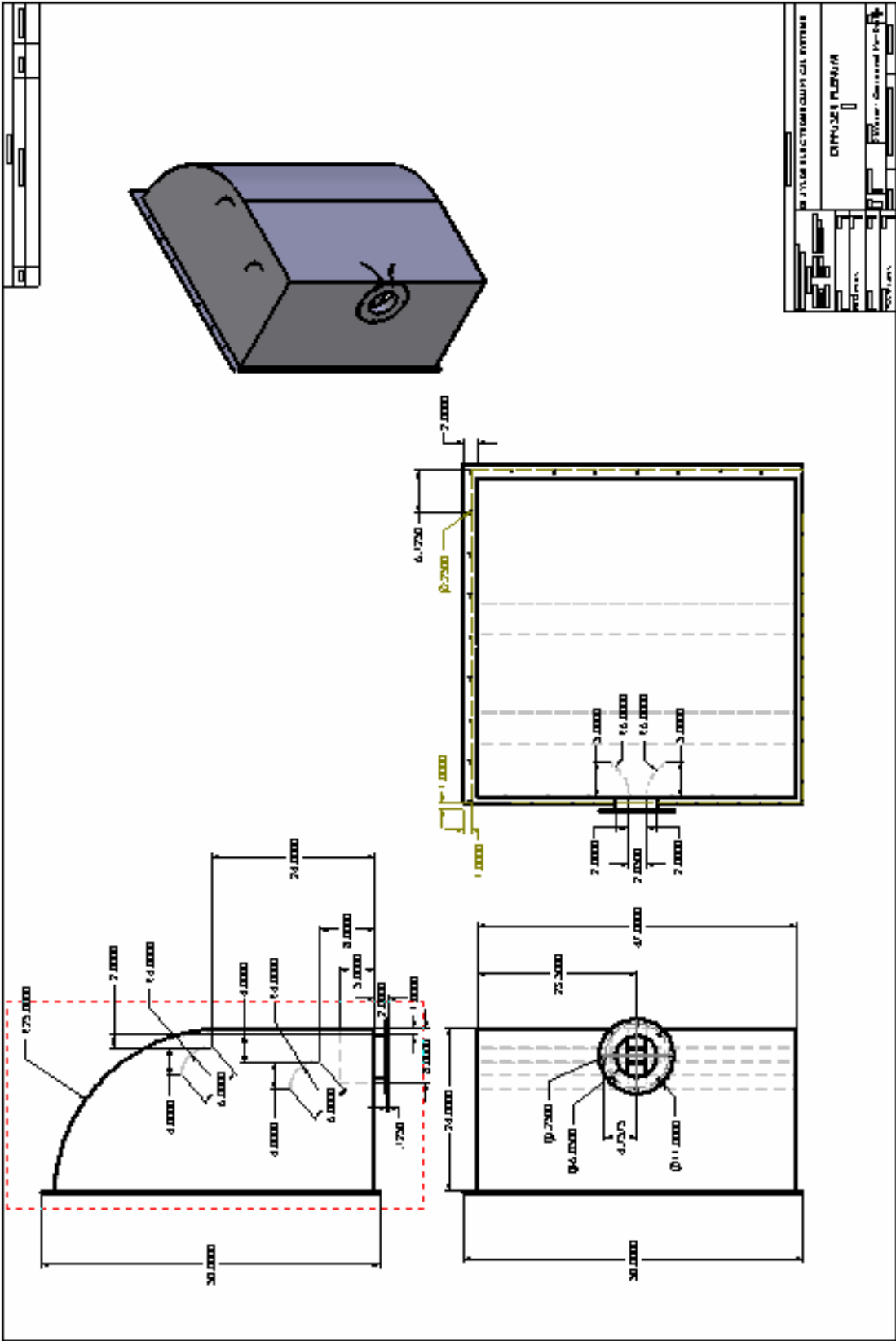
1.9382614 % difference

## APPENDIX J

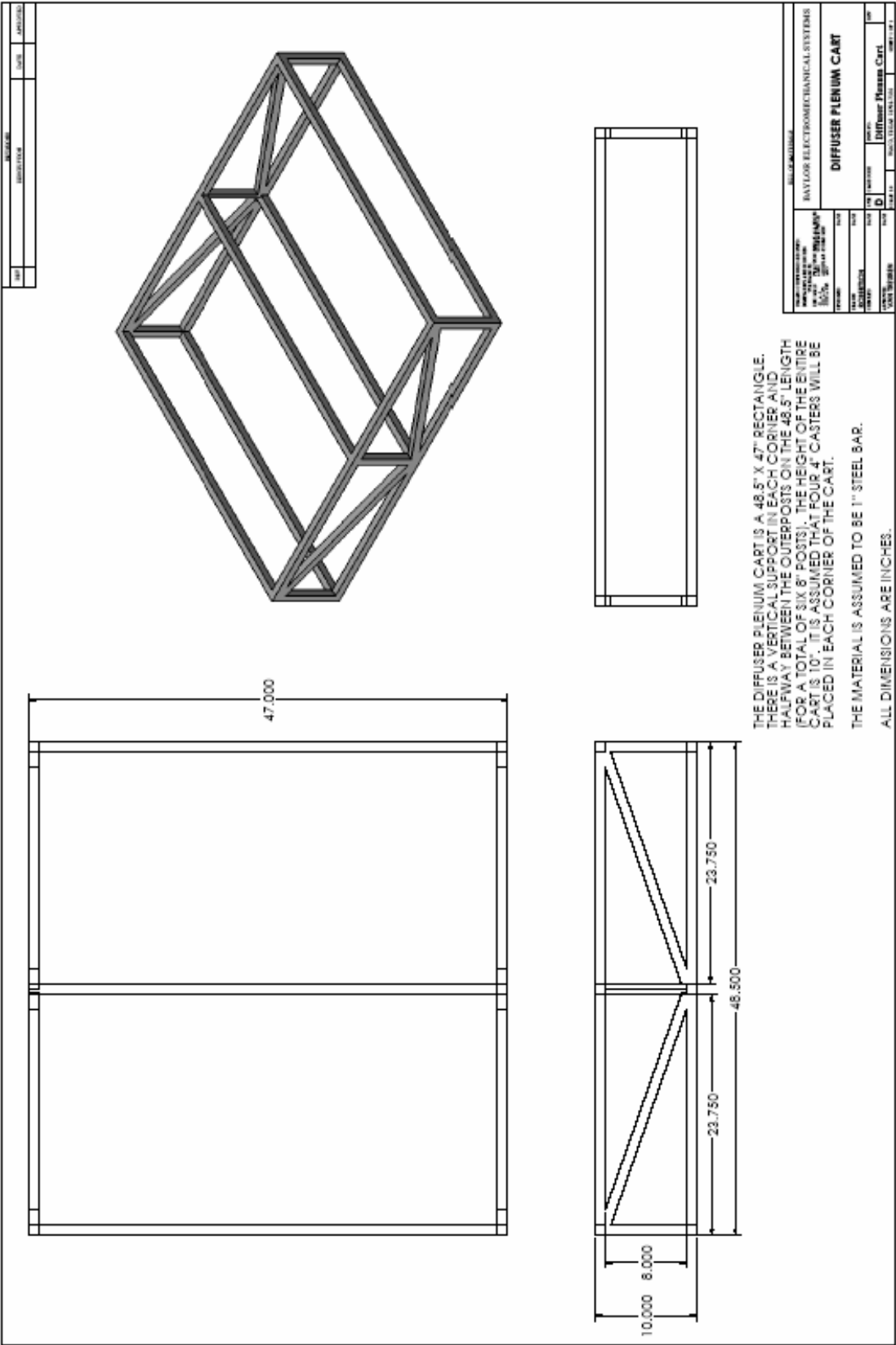
### Construction Drawings

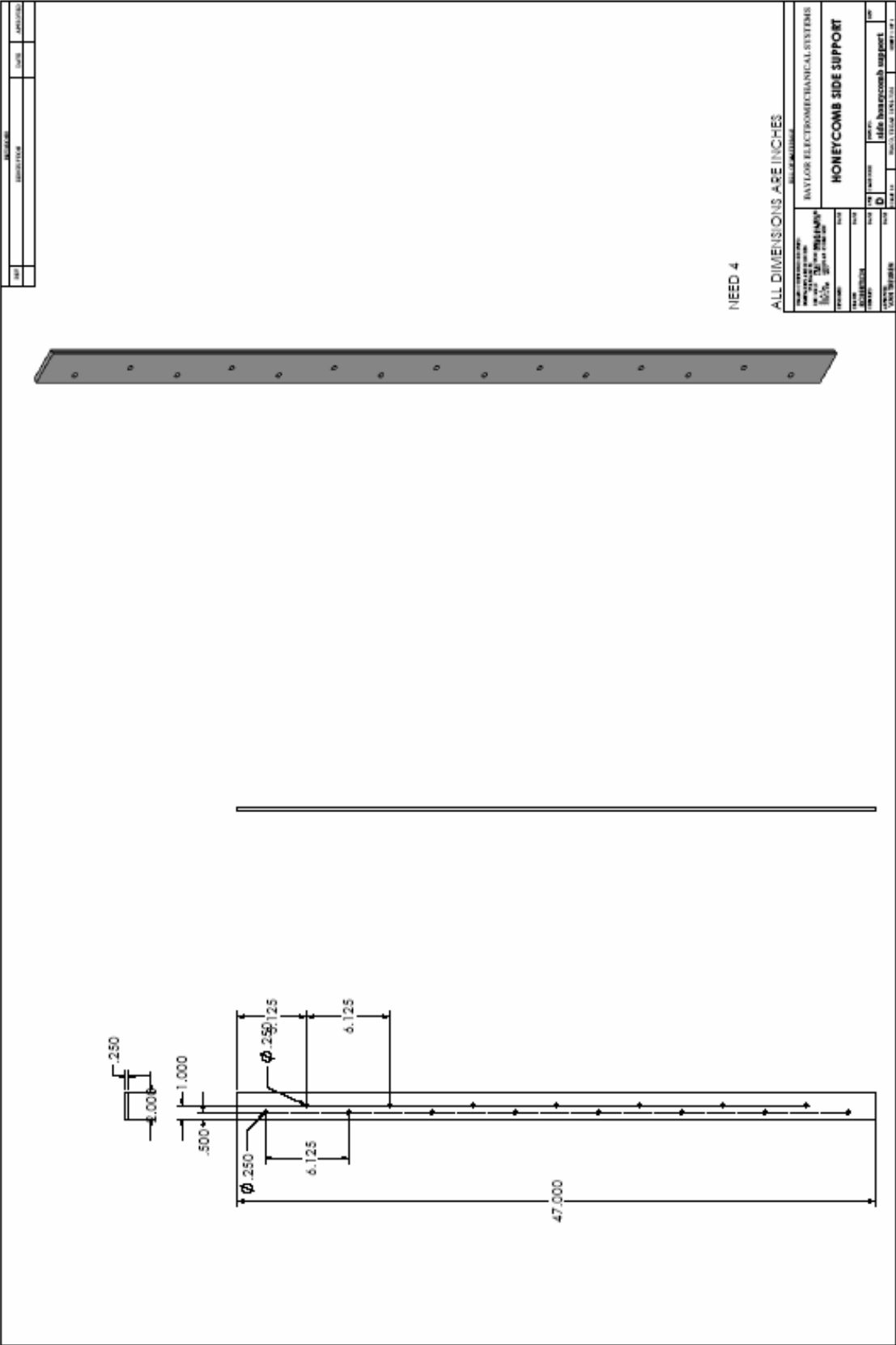


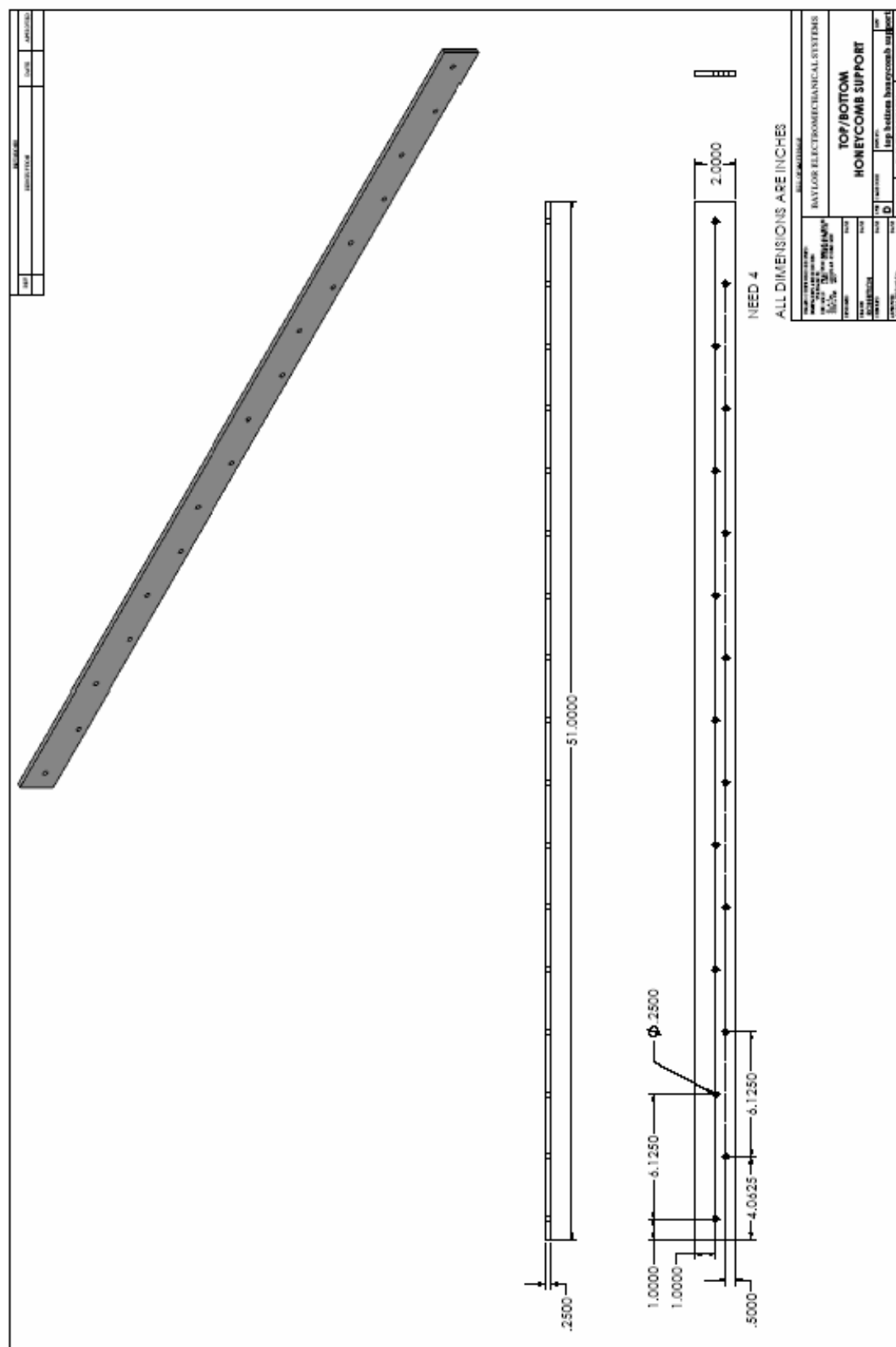












ITEM NO.	QTY	DESCRIPTION	UNIT
1	1	Rectangular Honeycomb Support	EA

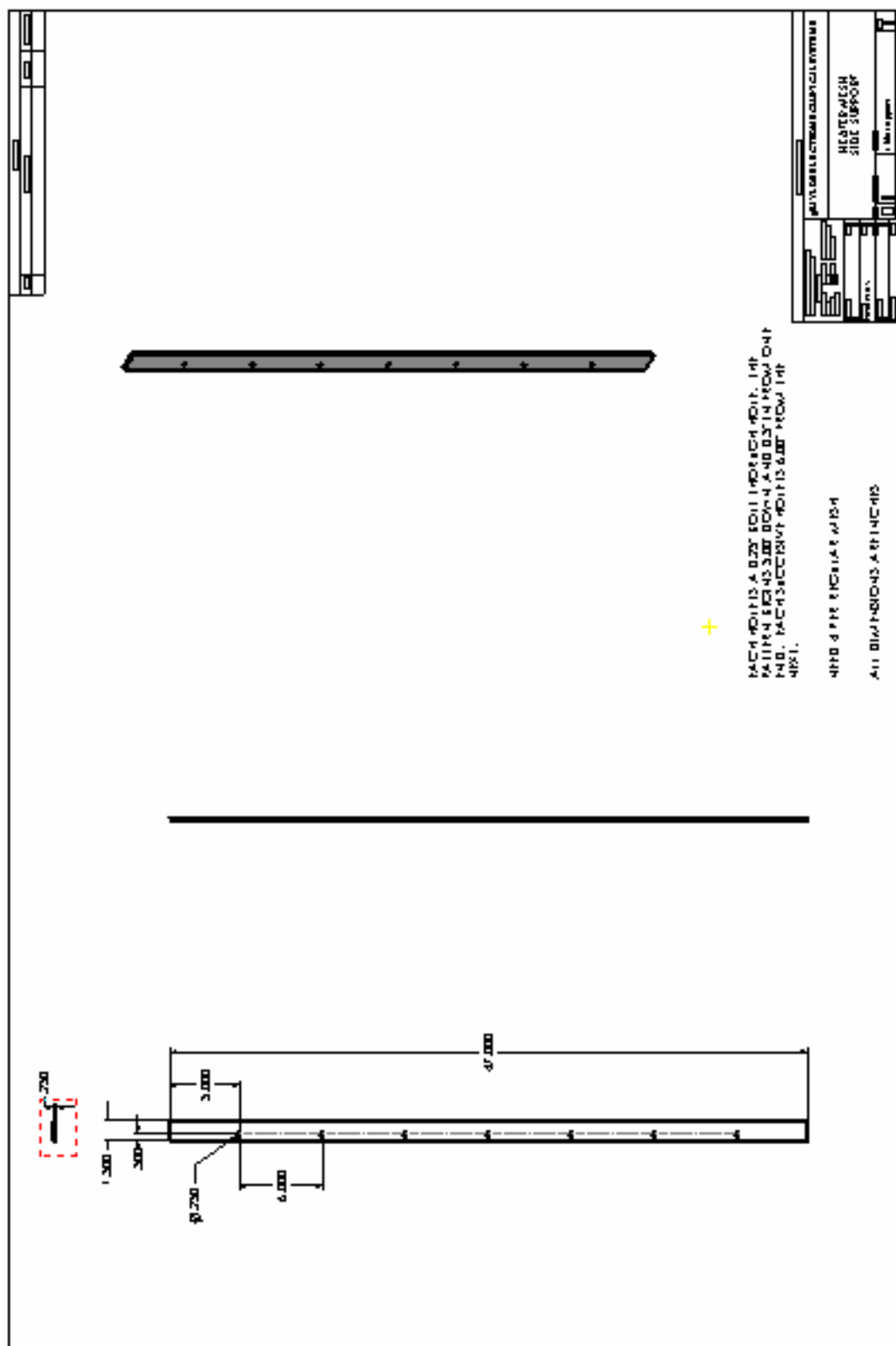
  

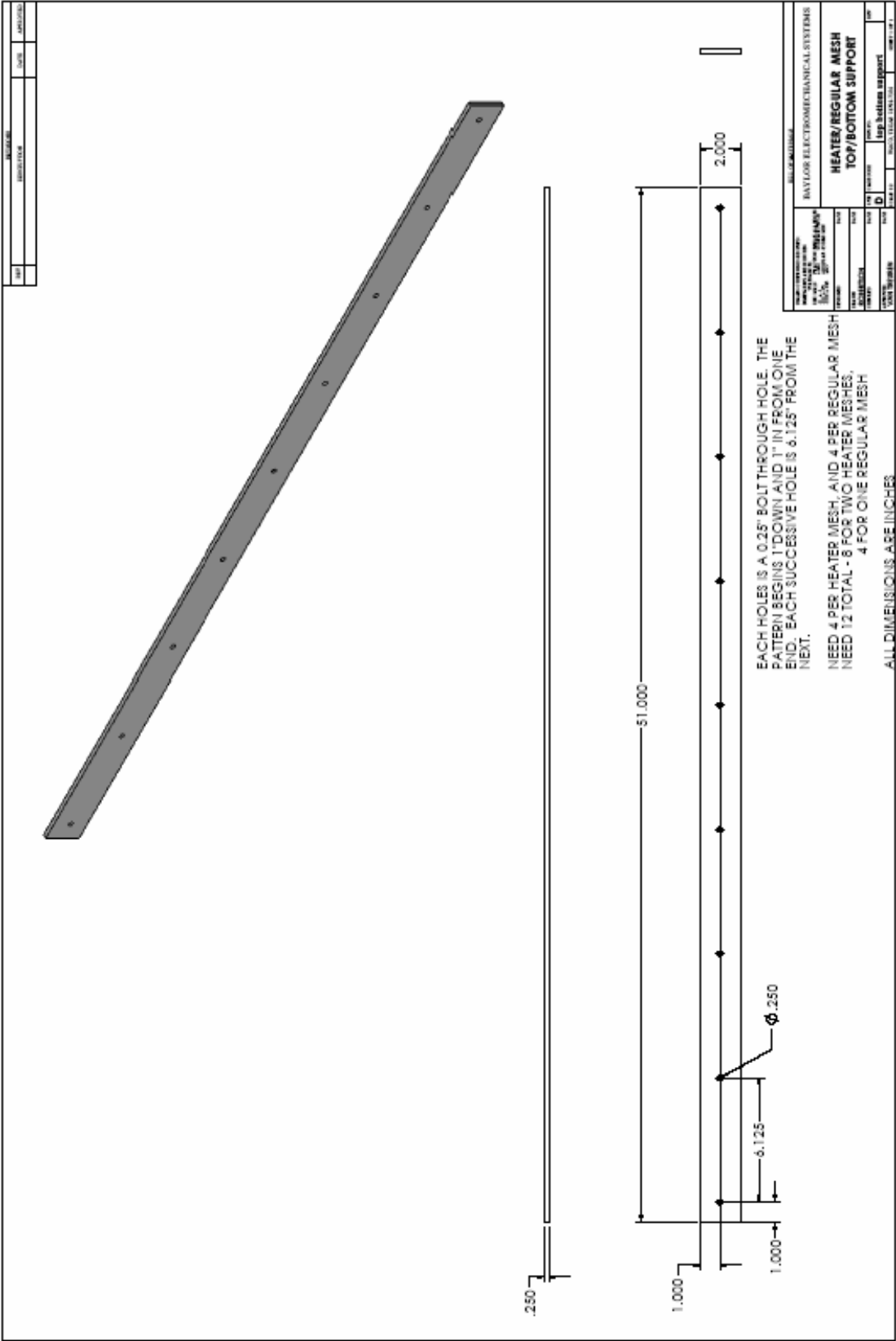
<b>REVISIONS</b> 1. REVISED TO ADD HONEYCOMB SUPPORT		<b>DATE</b> 10/10/2010
<b>REVISED BY</b> J. Smith	<b>APPROVED BY</b> M. Jones	<b>DATE</b> 10/10/2010

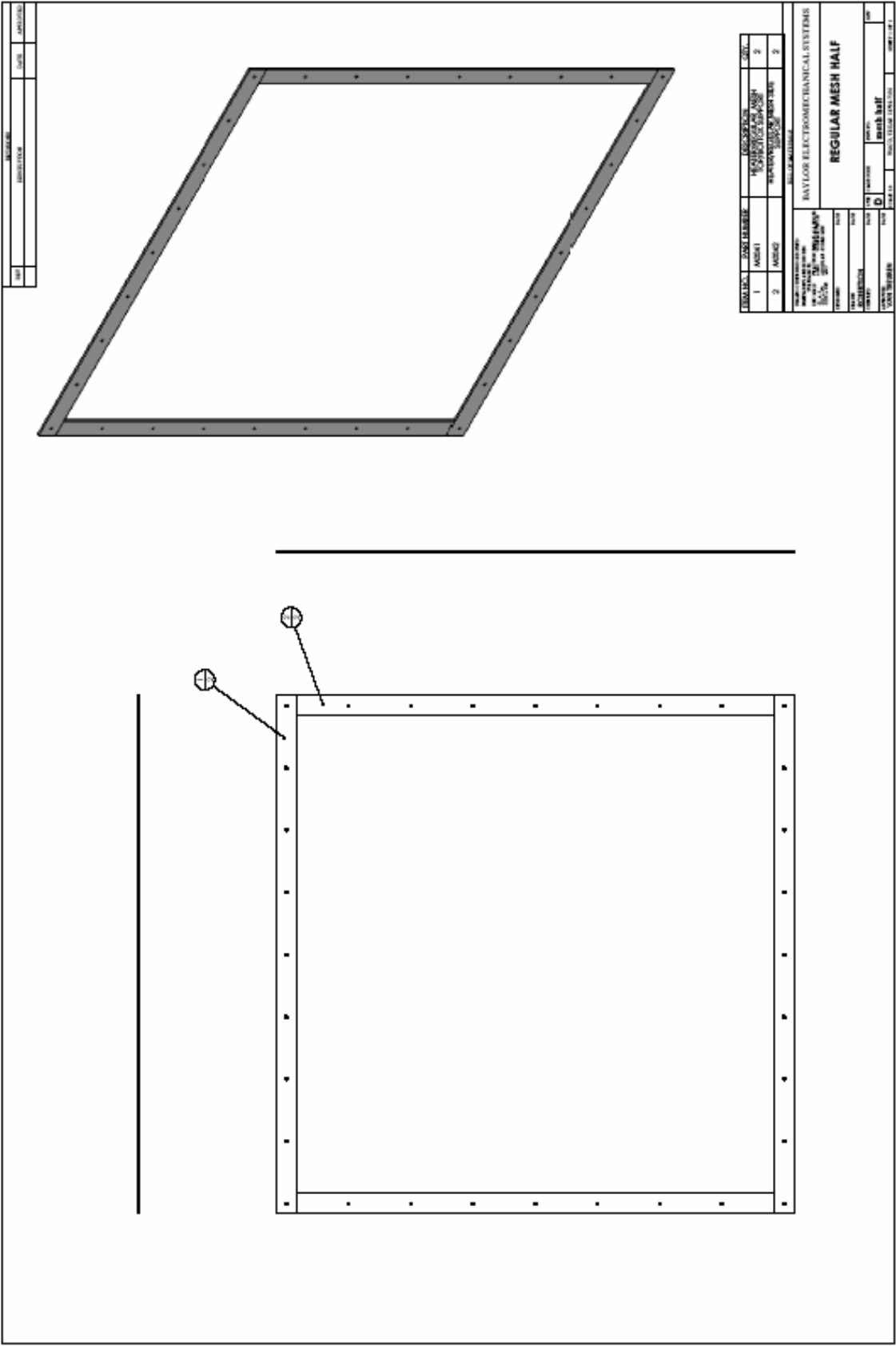
  

<b>PROJECT</b> BAYLOR ELECTROMECHANICAL SYSTEMS	
<b>DESCRIPTION</b> HONEYCOMB SUPPORT	
<b>DATE</b> 10/10/2010	<b>BY</b> J. Smith
<b>CHKD BY</b> M. Jones	<b>APP'D BY</b> M. Jones



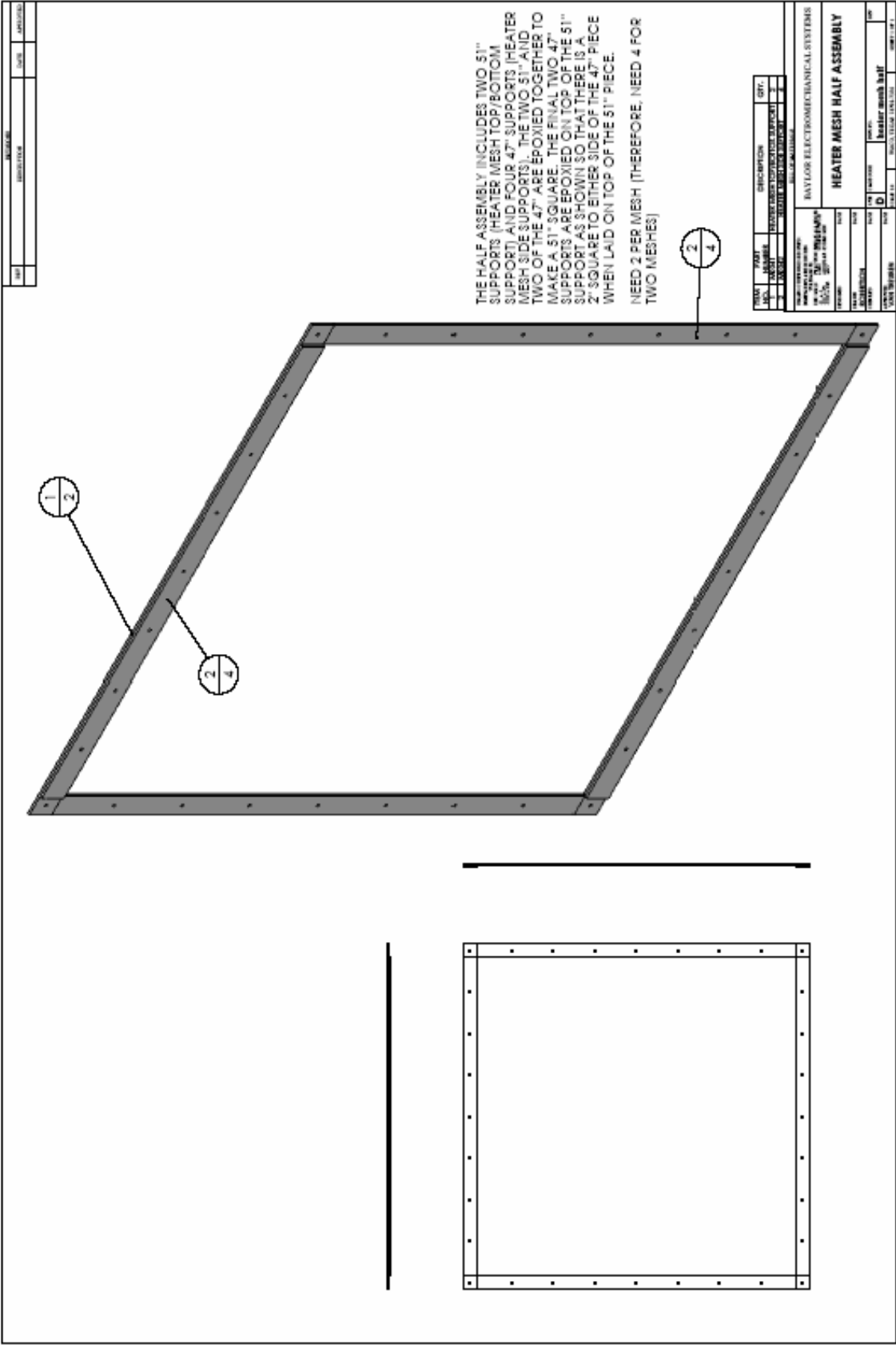


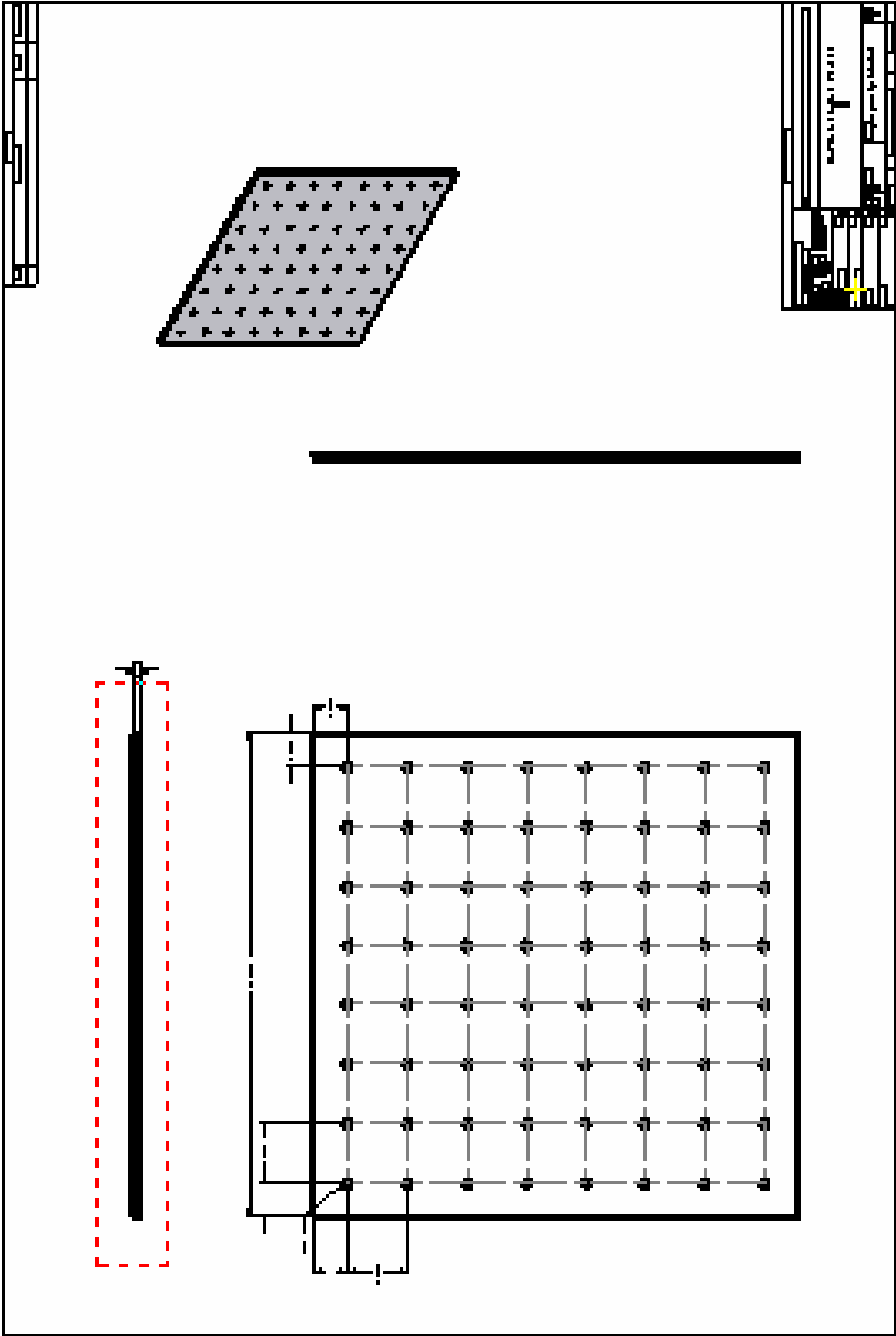












## REFERENCES

- Acalar, M.S., and Smith, C.R., 1987. A Study of Hairpin Vortices in a Laminar Boundary Layer. Part 2. Hairpin Vortices Generated by Fluid Injection. *Journal of Fluid Mechanics*, Vol. 87, pp. 43-83.
- Adavi, K. and Van Treuren, K.W., 2003. MATLAB Code for Analyzing Heat Transfer Images.
- Anderson, M.R., and Baughn, J.W., 2004. Hysteresis in Liquid Crystal Thermography. *Journal of Heat Transfer*, Vol. 126, No. 3, pp. 339-346.
- Bailey, J.C. and Bunker, R.S., 2002. Local Heat Transfer and Flow Distributions for Impinging Jet Arrays of Dense and Sparse Extent. ASME paper GT-2002-30473.
- Baughn, J.W., and Shimizu, S., 1989. Heat Transfer Measurements From a Surface with Uniform Heat Flux and an Impinging Jet. *ASME Journal of Heat Transfer*, Vol. 111, pp. 1096-1098.
- Bonnet, P., 1989. Applications of Liquid Crystals in Aerodynamic Testing. *D. Phil Thesis*, Department of Engineering Science, University of Oxford, England.
- Borns, F.G., 1989. Gas Turbine Engine Mechanical Design Considerations for Turbine Rotors. *Allied-Signal Aerospace Company Garret Engine Presentation at the United States Air Force Academy*.
- British Standards, BS1042, 1989. Measurement of Fluid Flow in Closed Conduits. British Standards Institution, London.
- Byerley, A.R., Ireland, P.T., Jones, T.V., and Ashton, S.A., 1988. Detailed Heat Transfer Measurements Near and Within the Entrance of a Film-Cooling Hole. ASME paper 88-GT-155.
- Cheong, B.C.Y., 2002. Flow and Heat Transfer Characteristics of an Impinging Jet with Crossflow. *D. Phil Thesis*, Department of Engineering Science, University of Oxford, England.
- Cincinnati Fan, 2000. Fan Selection and Performance. Manufacturer's Data.
- den Ouden, C. and Hoogendoorn, C.J. 1974. Local Convective Heat Transfer Coefficients for Jets Impinging on a Plate: Experiments Using Liquid Crystal. *5<sup>th</sup> International Heat Transfer Conference*.

- Florschuetz, L.W., Metzger, D.E., and Truman, C.R., 1981. Jet Array Impingement with Crossflow – Correlation of Streamwise Resolved Flow and Heat Transfer Distributions. *NASA Contractor Report 3373*.
- Florschuetz, L.W., Metzger, D.E., Su, D.E., and Isoda, Y., 1982. Jet Array Impingement Flow Distributions and Heat Transfer Characteristics. *NASA Contractor Report 3630*.
- Gao, L., Ekkad, S.V., and Bunker, R.R., 2003. Impingement Heat Transfer Under Linearly Stretched Arrays of Holes. ASME Paper GT2003-38178.
- Gao, X. and Sunden, B. 2002. Experimental Investigation of the Heat Transfer Characteristics of Confined Impinging Slot Jets. *Experimental Heat Transfer*, Vol. 16, pp. 1-18.
- Gardon, R. and Akfirat, J.C., 1965. The Role of Turbulence in Determining the Heat-Transfer Characteristics of Impinging Jets. *Int. J. Heat and Mass Transfer*, Vol. 8, pp. 1261-1272.
- Gillespie, D.R.H., 1993. First Year Report.
- Goldstein, R.J., Behbahani, A.I., and Heppelmann, K.K., 1986. Streamwise Distribution of the Recovery Factor and the Local Heat Transfer Coefficient to an Impinging Circular Air Jet. *Int. J. Heat and Mass Transfer*, Vol. 29, No. 8, pp. 1227-1235.
- Groth, J., 1991. On the Modeling of Homogeneous Turbulence. *Tech Rep.*, Dep. Of Mechanics, KTH, SE-100 E Stockholm.
- Han, J.C., Dutta, S., and Ekkad, S., 2000, Gas Turbine Heat Transfer and Cooling Technology. Taylor & Francis Group, New York.
- Hay, N., Khaldi, A., and Lampard, D., 1987. Effects of Crossflows on the Discharge Coefficients of Film Cooling Holes with Rounded Entries or Exits. *Proc. 2<sup>nd</sup> ASME-JSME Thermal Engineering Joint Conference*, Honolulu, HI, Vol. 3, pp. 369-374.
- Hebert, R., Ekkad, S.V., Khanna, V., Abreu, M., and Moon, H.K., 2004. Heat Transfer Study of a Novel Low-Crossflow Design for Jet Impingement. *Proceedings of ASME International Mechanical Engineering Congress & Exposition*. IMECE paper IMECE2004-60468.
- Hippensteele, S.A., Russell, L.M. and Stepka, F.S., 1983. Evaluation of a Method for Heat Transfer Measurements and Thermal Visualization Using a Composite of a Heater Element and Liquid Crystals. *ASME Journal of Heat Transfer*, Vol. 105, No. 1, pp. 184-189.
- Hirschberg, Mike. On the Vertical Horizon: IHPTET – Power for the Future. 7 December 2004. <<http://www.vtol.org/IHPTET.HTM>>.

- Hollworth, B.R. and Bowley, W.W., 1975. Heat Transfer Characteristics of an Impinging Jet in Crossflow. ASME Paper 75-WA/HT-100.
- Holman, J.P., 2001. Experimental Methods for Engineers, 7<sup>th</sup> Ed. McGraw Hill Co., New York.
- Hong, S.K., Rhee, D.H., and Cho, H.H., 2005. Effects of Fin Shapes and Arrangements on Heat transfer for Impingement/Effusion Cooling with Crossflow. ASME GT2005-68684.
- Ireland, P.T., and Jones, T.V., 1987. The Response Time of a Surface Thermometer Employing Encapsulated Thermochromatic Liquid Crystals. *J. Phys. E: Sci. Instrum.*, Vol. 20, pp. 1195-1199.
- Ireland, P.T., Wang, Z., and Jones, T.V., 1993. Liquid Crystal Heat Transfer Measurements. Lectures for the series on Measurement Techniques, von Karman Institute for Fluid Dynamics, 1992-1993 Lecture Series.
- Ireland, P.T., Personal communication, August 31, 2005.
- Jambunathan, K., Lai, E., Moss, M.A., and Button, B.L., 1992. A Review of Heat Transfer Data for Single Circular Jet Impingement. *Int. J. Heat and Fluid Flow*, Vol. 13, No. 2, pp. 106-115.
- James, A.J., 1961. Flow through a Long Orifice. *B.Sc. Thesis*, Nottingham University.
- Jeong, J., Hussain, F., Schoppa, W., and Kim, J., 1997. Coherent Structures Near the Wall in a Turbulent Channel Flow. *Journal of Fluid Mechanics*, Vol. 332, pp. 185-214.
- Jones, T.V., 1992. The Use of Liquid Crystals in Aerodynamic and Heat Transfer Testing. *Proc. 4<sup>th</sup> Int. Symp. on Transport Phenomena in Heat and Mass Transfer*, Vol. 2, pp. 1242-1273.
- Kanokjaruvijit, K., and Martinez-Botas, R.F., 2003. Parametric Effects of Heat Transfer of Impingement on Dimpled Surface. ASME paper GT2003-53142.
- Kercher, D.M., and Tabakoff, W., 1970. Heat Transfer by a Square Array of Round Air Jets Impinging Perpendicular to a Flat Surface Including the Effect of Air Spent. *ASME Journal of Engineering for Power*, Vol. 92, pp. 73-82.
- Lee, D.H., Chung, Y.S., and Kim, D.S., 1997. Turbulent Flow and Heat Transfer Measurements on a Curved Surface with a Fully Developed Round Impinging Jet. *Int. J. of Heat and Fluid Flow*, 18, pp. 160-169.
- Li, L.G., Zhang, D.L., and Lin, J.L., 1988. The Applications of the Liquid Crystal Technique to the Experimental Modeling of Impingement Cooling. 2<sup>nd</sup> International Symposium on Heat Transfer, Beijing.

- Lindgren, B., and Johansson, A.V., 2002. Design and Evaluation of a Low-Speed Wind Tunnel with Expanding Corners. TRITA-MEK 2002:14. Department of Mechanics, KTH.
- Mattingly, J.D., 1996. Elements of Gas Turbine Propulsion. McGraw-Hill, Inc., New York.
- McGrehan, W.F., and Schotsch, M.J., 1988. Flow Characteristics of Orifices with Rotation and Corner Radiusing. *ASME Journal of Turbomachinery*, Vol. 110, pp. 231-237.
- Mehta, R.D., and Bradshaw, P. 1979. Design Rules for Small Low Speed Wind tunnels. *The Aeronautical Journal of the Royal Aeronautical Society.*, pp. 443-449.
- Metzger, D.E., Bunker, R.S., and Bosch, G., 1989. Transient Liquid Crystal Measurement During Local Heat Transfer on a Rotating Disk with Jet Impingement. ASME paper 89-GT-287.
- Moffat, R.J., 1988. Describing the Uncertainties in Experimental Results. *Experimental Thermal and Fluid Science*, Vol. 1, pp. 3-17.
- Moss, R.W. and Oldfield, M.L.G., 1991. Measurements of Hot Combustor Turbulence Spectra. ASME paper 91-GT-351.
- Munson, B.R., Young, D.F., and Okiishi, T.H., 2002. Fundamentals of Fluid Mechanic, 4<sup>th</sup> Ed. John Wiley and Sons, Inc., New York.
- Nomoto, H., Okamura, T., and Ito, S., 1996. Turbine Cooling Blade Having Inner Hollow Structure with Improved Cooling. *United States Patent 5533864*.
- Obot, N.T., Majumdar, A.S., Douglas, W.J.M., 1979. The Effect of Nozzle Geometry on Impingement Heat Transfer Under a Round Turbulent Jet. ASME paper 79-WA/HT-53.
- Patel, P. and Roy, S., 2003. Heat Transfer for a pair of Rectangular jets Impinging upon an Inclined Surface. *International Journal of Heat and Mass Transfer*, Vol. 46, No. 3, pp. 411-425.
- Perry, K.P., 1954. Heat Transfer by Convection from a Hot Gas Jet to a Plane Surface. *Proceedings of the Institute of Mechanical Engineers (London)*, Vol. 168, pp. 775-784.
- Prandtl, L., 1932. Herstellung Einwandfrier Luftstrome (Windkanäle). *Handbuch der Experimentalphysik*, Leipzig, Germany, Vol. 4, Part 2, p. 73
- Rhee, D.H., Yoon, P.H., Cho, H.H., 2002. Local Heat/Mass Transfer and Flow Characteristics of Array Impinging Jets with Effusion Holes Ejecting Spent Air. *Int. J. of Heat and Mass Transfer*, Vol. 46, pp. 1049-1061.

- Robertson, P., and Van Treuren, K.W., 2005. "Design of an Impinging Jet Testing Facility." *Proceedings of the Great International Southwest Region X Graduate Student Technical Conference*, Lubbock, TX.
- San, J.Y., and Lai, M.D., 2001. Optimum Jet-to-Jet Spacing of Heat Transfer for Staggered Arrays of Impinging Air Jets. *Int. J. Heat and Mass Transfer*, 44, pp. 3997-4007.
- Saxena, V. Nassir, H. and Ekkad, S.V. 2003. Effect of Blade Tip Geometry on Tip Flow and Heat Transfer for a Blade in a Low Speed Cascade. ASME paper GT2003-38176.
- Schultz, D.L. and Jones, T.V., 1973. Heat Transfer Measurements in Short-Duration Hypersonic Facilities. AGARD AG-165.
- Son, C., Dailey, G., Ireland, P., and Gillespie, D., 2005. An Investigation of the Application of Roughness Elements to Enhance Heat Transfer in an Impingement Cooling System. ASME paper GT2005-68504.
- Stasiek, J. A., and Kowalewski, T.A., (2002). Thermochromatic Liquid Crystals Applied for Heat Transfer Research. *Opto-Electronics Review*, Vol. 10, No. 1, pp. 1-10.
- Van Treuren, K.W., 1994. Impingement Flow Heat Transfer Measurements of Turbine Blades Using a Jet Array. *D. Phil Thesis*, Department of Engineering Science, University of Oxford, England.
- Van Treuren, K.W., Wang, Z., Ireland, P., Jones, T.V., and Kohler, S.T., 1996. The Role of the Impingement Plate in Array Heat Transfer. ASME Paper 96-GT-162.
- Van Treuren, K.W., Wang, Z., Ireland, P.T., and Jones, T.V., 1994. Detailed Measurements of Local Heat Transfer Coefficient and Adiabatic Wall Temperature Beneath an Array of Impinging Jets. *Journal of Turbomachinery*, Vol. 116, pp. 369-374.
- Wang, Z., Gillespie, D.R.H., and Ireland, P.T., 1996. Advances in Heat Transfer Measurements Using Liquid Crystals. *Proc Engineering Foundation Turbulent Heat Transfer Conference*, San Diego CA.
- Wieghardt, K.E.G., 1953. On the Resistance of Screens. *Aero Quarterly*, Vol. 4, p. 186.